AD________________

GRANT NUMBER DAMD17-96-1-6023

TITLE: Fluorescence Lifetime Imaging for Breast Cancer Detection and Diagnosis

PRINCIPAL INVESTIGATOR: Eva M. Sevick Muraca, Ph.D.

CONTRACTING ORGANIZATION: Purdue Research Foundation
West Lafayette, Indiana 47907

REPORT DATE: July 1998

TYPE OF REPORT: Annual

PREPARED FOR: Commander
U.S. Army Medical Research and Materiel Command
Fort Detrick, Maryland 21702-5012

DISTRIBUTION STATEMENT: Approved for Public Release;
Distribution Unlimited

The views, opinions and/or findings contained in this report are those of the author(s) and should not be construed as an official Department of the Army position, policy or decision unless so designated by other documentation.

DTIC QUALITY INSPECTED 4

REPORT DOCUMENTATION PAGE

Form Approved
OMB No. 0704-0188

Public reporting burden for this collection of information is estimated to average 1 hour per response, including the time for reviewing instructions, searching existing data sources, gathering and maintaining the data needed, and completing and reviewing the collection of information. Send comments regarding this burden estimate or any other aspect of this collection of information, including suggestions for reducing this burden, to Washington Headquarters Services, Directorate for Information Operations and Reports, 1215 Jefferson Davis Highway, Suite 1204, Arlington, VA 22202-4302, and to the Office of Management and Budget, Paperwork Reduction Project (0704-0188), Washington, DC 20503.

1. AGENCY USE ONLY *(Leave blank)*

2. REPORT DATE
July 1998

3. REPORT TYPE AND DATES COVERED
Annual (1 Jul 97 - 30 Jun 98)

4. TITLE AND SUBTITLE
Fluorescence-Lifetime Imaging for Breast Cancer Detection and Diagnosis

5. FUNDING NUMBERS
DAMD17-96-1-6023

6. AUTHOR(S)
Eva M. Sevick Muraca, Ph.D.

7. PERFORMING ORGANIZATION NAME(S) AND ADDRESS(ES)
Purdue Research Foundation
West Lafayette, Indiana 47907

8. PERFORMING ORGANIZATION REPORT NUMBER

9. SPONSORING / MONITORING AGENCY NAME(S) AND ADDRESS(ES)
U.S. Army Medical Research and Materiel Command
Fort Detrick, Maryland 21702-5012

10. SPONSORING / MONITORING AGENCY REPORT NUMBER

19981210 092

11. SUPPLEMENTARY NOTES

12a. DISTRIBUTION / AVAILABILITY STATEMENT
Approved for Public Release; Distribution Unlimited

12b. DISTRIBUTION CODE

13. ABSTRACT *(Maximum 200 words)*

In this exploratory research program, the use of fluorescent contrast agents for detection and diagnosis of sub-surface diseased tissues is demonstrated. Using Newton-Raphson inversion techniques, we demonstrated the ability to map fluorescence lifetime and quantum efficiency from frequency-domain measurements of photon migration using synthetic data sets. Multi-pixel instrumentation for generation of actual data sets was constructed and is planned to validate the approach of fluorescence lifetime imaging of breast disease using optical contrast agents.

14. SUBJECT TERMS
Breast Cancer
Flouorescent contrast agents,
Optical Imaging

15. NUMBER OF PAGES
103

16. PRICE CODE

17. SECURITY CLASSIFICATION OF REPORT
Unclassified

18. SECURITY CLASSIFICATION OF THIS PAGE
Unclassified

19. SECURITY CLASSIFICATION OF ABSTRACT
Unclassified

20. LIMITATION OF ABSTRACT
Unlimited

FOREWORD

Opinions, interpretations, conclusions and recommendations are those of the author and are not necessarily endorsed by the U.S. Army.

____ Where copyrighted material is quoted, permission has been obtained to use such material.

____ Where material from documents designated for limited distribution is quoted, permission has been obtained to use the material.

____ Citations of commercial organizations and trade names in this report do not constitute an official Department of Army endorsement or approval of the products or services of these organizations.

____ In conducting research using animals, the investigator(s) adhered to the "Guide for the Care and Use of Laboratory Animals," prepared by the Committee on Care and use of Laboratory Animals of the Institute of Laboratory Resources, national Research Council (NIH Publication No. 86-23, Revised 1985).

____ For the protection of human subjects, the investigator(s) adhered to policies of applicable Federal Law 45 CFR 46.

____ In conducting research utilizing recombinant DNA technology, the investigator(s) adhered to current guidelines promulgated by the National Institutes of Health.

____ In the conduct of research utilizing recombinant DNA, the investigator(s) adhered to the NIH Guidelines for Research Involving Recombinant DNA Molecules.

____ In the conduct of research involving hazardous organisms, the investigator(s) adhered to the CDC-NIH Guide for Biosafety in Microbiological and Biomedical Laboratories.

Eva M Szent- 9/23/98
PI - Signature Date

Fluorescence Lifetime Imaging for Breast Cancer Detection and Diagnostics

TABLE OF CONTENTS:

Report Documentation Page ....(i)

Foreword....(ii)

Table of Contents....1

I. INTRODUCTION....2

II. COMPUTATIONAL METHODS....4

III. EXPERIMENTAL METHODS AND APPROACHES....5

IV. SUMMARY....7

V. REFERENCES....9

VI. BIBLIOGRAPHY....10

VII. APPENDIX

I. Introduction

The development of biomedical optical imaging for the detection of breast cancer has been the subject of an increasing number of research programs in science, engineering, and medicine. The ability to optically detect breast cancer in a group of women who are not good candidates for conventional mammography depends upon the optical contrast available between normal and diseased tissues. In a study published in 1996, we measured the optical properties of 115 human breast tissue specimens in order to ascertain the level of contrast which may be available for the proposed general screening tool of "optical mammography." Our results, although they underpredict the contrast owing to absorption, suggest that there is insufficient contrast for the detection of disease. In addition, that study suggests the need for an optical contrast agent.

The detection of superficially located diseased tissues via the use of fluorescent dyes and photodynamic drugs as contrast agents has been proposed by several investigators over the past several years. In our program, we have investigated the development of imaging technologies which employ fluorescent drugs or agents for detection of small lesions beneath the skin, or tissue volumes that are located several centimeters deep, However, to accomplish such a technology, a long-standing problem must be overcome. Specifically, the low uptake or "leakage" into diseased tissues, providing insufficient contrast for detection of disease, While targeted delivery may improve uptake ratios and contrast imparted by these agents, drug and contrast agent targeting approaches have been rather elusive even in conventional imaging modalities such as magnetic resonance imaging and x-ray computer tomography. Investigators have sought to improve optical contrast independent of uptake ratio by employing dyes which fluoresce differently in diseased and normal tissues. The use of agents whose emission characteristics vary with tissue pH and O2 may not only enhance detection of diseased tissues by the nature of differing fluorescent properties, but may also contain diagnostic information regarding the disease.

The difficulty, however, lies in using the multiply scattered light detected at the tissue-air interface to reconstruct and image which differentiates internal tissues on the basis of uptake and the fluorescent properties of quantum yield and lifetime. In ongoing work in this and other laboratories, investigators have demonstrated the capacity for fluorescent lifetime and quantum yield imaging form frequency-domain measurements of modulation phase-shift and amplitude demodulation conducted at the surface of simulated tissue phantoms. Under this support, the aims of the exploratory project were:

(1) To develop inverse imaging algorithms providing lifetime and yield mapping of tissues as thick as five centimeters;

(2) To measure the temporal, re-emitted excitation and fluorescence from tissue phantoms using frequency-domain techniques; and

(3) To use these measurements as input into the inverse imaging algorithm for reconstruction of lifetime and yield maps.

Specifically, we seek to develop fluorescence lifetime imaging techniques for screening in a population of women who are at high risk for the disease, and for those women who require prognostic information of lymphatic involvement in order to aid in the management of the disease. This DOD support focuses upon the development of inverse solution procedures and coupling of measurements to image algorithms for the detection of disease. These specific aims are the foundations of the technology.

II. Computational Methods

As described in the publications in the Appendix, our work has been towards the development of forward simulators of the propagation of excitation and emission light in tissues. Under this support, we have generated two forward solvers:

(1) a finite difference, MUDPACK routine operating in two and three dimensions, and
(2) a finite element approach which enables arbitrary tissue geometry.

We have also developed Newton-Raphson based inversion strategies which enable the reconstruction of fluorescent lifetime and the product of quantum efficiency and absorption cross section (Paithankar, et al., 1997) as well as the reconstruction of fluorescent lifetime, quantum efficiency, and absorption cross section (Troy and Sevick, 1998). The publications are included in the Appendix for further information.

More recently, in the latter two months of the DOD project, we have coupled with University of Vermont's Computer Science Department in order to develop Bayesian optical tomography techniques. The approach provides a zonation structure to the inverse optical imaging problem, enabling rapid convergence and stability for reconstruction of absorption and fluorescent properties.

III. Experimental Methods

In our inversion strategies, we have employed synthetic data to demonstrate the feasibility of optical imaging of absorption and fluorescence following the administration of a contrast agent. In order to demonstrate the feasibility of the technology, we need to develop fast methods for data acquisition of frequency-domain photon migration measurements, demonstrate the ability to match experimental measurements with those predicted by our forward solvers, and create real, experimental data sets for incorporation into our solutions to the inverse optical imaging problem. In part under this support, we have developed a multi-pixel imaging device which consists of a gain modulated image intensified camera to capture measurements of phase and amplitude modulation of re-emitted light from the surface of tissues without the need to optically couple or contact the tissue.

The details of the apparatus are found in a publication included in the appendix. Briefly, the technique depends upon illuminating the tissue volume of interest with a modulated light source, i.e., either a point source of light delivered by a fiber optic, or a plane wave created by the expansion of a diode beam. The light which propagates from the source within the tissue and to the various positions on the surface of the tissue is collected by the ICCD system which is focused upon the surface of interest. Incidentally, the ICCD system enables in principle 512 x 512 pixel measurements on the surface of a tissue whose dimensional are set by a focusing lens. Measurements can be made of excitation light, as well as from the fluorescence generated by a contrast agent. We report that the measurements are hundreds of times faster than single-pixel scanning demonstrated by other groups and imaging companies and point out that our measurements contain less noise than that reported for single-pixel systems. Since the propagation of measurement noise into an inverse solution severely deteriorates the solution or the determined optical image, we expect that our measurement approach provides the best means for coupling real experimental data to the solution for the inverse imaging problem.

While we were unable to couple the measurements with the inversion algorithms owing to the short duration and small funding level of this exploratory research proposal, we have nonetheless demonstrated the ability to quantify fluorescence lifetime in a highly scattering, uniform medium. While the manuscript are currently under preparation and will be made available to the funding agency upon their completion, the following briefly summarizes our approach and findings. These experimental measurements confirm the ability to quantify fluorescence lifetime in scattering media.

The goals of the non-imaging experiments were to determine the fluorescent optical properties of a dye in a highly scattering media. Specifically, we sought to determine the lifetime of Indocyanine Green (currently used a s a contrast agent in our animal studies supported under separate funding) and IR-140, a common laser dye, Indocyanine Green has a measured lifetime of 0.58 ns as measured in our laboratory while IR-140 has a lifetime of 1.19 ns. Using frequency-domain measurements of photon migration, we sought to determine the lifetime of these two dyes when contained in micromolar concentrations within a tissue-like scattering solution of 0.5% Intralipid. This gives us confidence that the inverse optical imaging of fluorescence lifetime can be achieved, We found that in order to effectively perform lifetime spectroscopy in scattering media, we required three FDPM measurements: One measurement was required at the excitation wavelength in which a neutral density filter was simply placed at the detector in order to determine the propagation characteristics of the excitation light. Another measurement involved measuring the propagation of an incident wave that was at the same wavelength as the generated fluorescence. We term this measurement the emission FDPM measurement. Finally, the final measurement consisted of exciting the sample with the excitation light and using interference filters to collect the generated fluorescence which propagated to the surface. From these measurements, we were able to determine the lifetime of the dye without using any a priori information regarding the optical properties of the medium. Our results, again which will be made available to the DOD in the coming weeks, verify the feasibility of fluorescence lifetime imaging in tissues.

IV. CONCLUSIONS

The exploratory research supported by the DOD provided the following results:

(i) The inverse imaging problem for fluorescence lifetime has a solution as demonstrated using synthetic data sets.

(ii) Multi-pixel imaging devices were developed in part under this support to provide experimental data sets for demonstration of fluorescence lifetime imaging.

(iii) Using single-pixel measurements, we demonstrated the ability to perform lifetime spectroscopy in homogeneous scattering media.

In the future, we require the coupling of the multi-pixel measurements with the solutions to the optical imaging modality to provide a new imaging modality to provide detection and perhaps diagnostics based upon spectroscopic parameters of fluorescent photophysical properties.

V. REFERENCES

Troy, T.L., Page, D.L., and E.M. Sevick-Muraca, Öptical properties of normal and diseased breast tissues: prognosis for optical mammography," J. Biomedical Optics, 1: 342-355, 1996.

Paithankar, D.Y., Chen, A.U., Pogue, B.W., Patterson, M.S., and E.M. Sevick-Muraca, ïmaging of fluorescent yield and lifetime from multiply scattered light re-emitted from tissues and other random media," Appl. Optics, 36: 2260-2272, 1997.

Reynolds, J.S., Troy, T.L., and E.M. Sevick-Muraca, "Multi-pixel techniques for frequency-domain photon migration imaging," Biotech. Prog., 13: 669-680, 1997.

Troy, T.L. amd E.M. Sevick-Muraca, "Fluorescence lifetime imaging and spectroscopy in random media,"in Applied Fluorescence in Chemistry, Biology, and Medicine, Rettig, Ed., Springer Verlag, 1998.

Biobliography

Paithankar, D.Y. Chen, A.U., Pogue, B.W., Patterson, M.S., and E.M. Sevick-Muraca, "Imaging of fluorescent yield and lifetime from multiply scattered light re-emitted from tissues and other random media," Appl. Optics, 36: 2260-2272, 1997. *(8)*

Sevick-Muraca, E.M., Lopez, G., Troy, T.L., Reynolds, J.S., and C.L. Hutchinson, "Fluorescence and absorption contrast mechanisms for biomedical optical imaging using frequency-domain techniques," Photochemistry and Photobiology, 66: 55-64, 1997. *(3)*

Reynolds, J.S., Troy, T.L., and E.M. Sevick-Muraca, "Multi-pixel techniques for frequency-domain photon migration imaging," Biotech. Prog. (invited) 13: 669-680, 1997.

Sevick-Muraca, E.M., Heintzelman, D.L., Lee, J., Troy, T.L., and D.Y. Paithankar, "The role of higher order scattering in solutions to the forward and inverse optical imaging problems in random media," Appl. Optics, 36: 9058-9067, 1997.

Troy, T.L., and E.M. Sevick-Muraca, "Fluorescence lifetime imaging and spectroscopy in random media," in Applied Fluorescence in Chemistry, Biology, and Medicine, Rettig, ed., Springer Verlag, 1998.

Sevick-Muraca, E.M. and D.Y. Paithankar, "Imaging of fluorescent yield and lifetime from multiply scattered light re-emitted from random media," In Advances in Fluorescence Sensing Technology in Chemical Diagnostics III, eds. J.R. Lakowicz and R.B. Thompson, Proc. Soc. Photo-Opt. Instrum. Eng., 2980: 303-318, 1997.

Reynolds, J.S., Troy, T.L., and E.M. Sevick-Muraca, "Multi-pixel imaging of interfering photon density waves," in Optical Tomography and Spectroscopy of Tissue: Theory, Instrumentation, Model, and Human Studies II, B. Chance and R.R. Alfano (eds), Proc. Soc. Photo-Opt. Instrum. Eng., 2979: 122-128, 1997.

Lopez, G., Troy, T.L., Reynolds, J.S., Hutchinson, C.L., and E.M. Sevick-Muraca, "Detection of fluorescent and light absorbing optical hetereogeneities in tissue-mimicking phantoms using frequency-domain techniques," In Advances in Fluorescence Sensing Technology in Chemical Diagnostics III, eds. J.R. Lakowicz and R.B. Thompson (eds), Proc. Soc. Photo-Opt. Instrum. Eng., 2980: 519-529, 1997.

Chen, A. and E.M. Sevick-Muraca, "On the use of phosphorescent and fluorescent dyes for lifetime-based imaging within tissues," Proc. Soc. Photo-Opt. Instrum. Eng., in Optical Tomography and Spectroscopy of Tissue: Theory, Instrumentation, Model, and Human Studies II, B. Chance and R.R. Alfano (eds), 2979: 129-138, 1997.

Troy, T.L., Reynolds, J.S., and E.M. Sevick-Muraca, "Photon migration imaging using multi-pixel measurements," in Optical Tomography and Spectroscopy of Tissue: Theory, Instrumentation, Model, and Human Studies II, B. Chance and R. R. Alfano (eds), Proc. Soc. Photo-Opt. Instrum. Eng., 2979: 111-121, 1997.

Troy, T.L., Reynolds, J.S., and E.M. Sevick-Muraca, "Reconstruction of fluorescence lifetime and quantum efficiency using frequency-domain photon migration measurements," Optical Society of America Proceedings in Biological Optical Spectroscopy and Diagnostics, 1998.

Reynolds. J.S., Troy, T.L., Waters, D.J., Cornell, K.K., and E.M. Sevick-Muraca, "Multi-pixel freqeuncy-domain photon migration imaging of a fluorescent contrast agent," Optical Society of America Proceedings in Biological Optical Spectroscopy and Diagnostics, 1998.

Lopez, G., Troy, T.L., Hutchinson, C.L., D.Y. Paithankar, and E.M. Sevick-Muraca, "Fluorescent contrast agents for biomedical optical imaging using frequency-domain techniqqes," Proc. Soc. Photo-Opt. Instrum. Eng., San Jose, CA, February 1997.

Chen, A.U., Paithankar. D.Y., and E.M. Sevick-Muraca,"The affects of chromophore lifetime on the propagation of light through scattering media," Proc. Soc. Photo-Opt. Instrum. Eng., San Jose, CA, February 1997.

Troy, T.L., Reynolds, J.S., and E.M. Sevick-Muraca,"Photon migration imaging using multi-pixel measurements," Proc. Soc. Photo-Opt. Instrum. Eng., San Jose, CA, February 1997.

Reynolds, J.S., and E.M .Sevick-Muraca,"Multipixel imaging with interfering photon density waves," Proc. Soc. Photo-Opt. Instrum. Eng., San Jose, CA, February 1997.

Sevick-Muraca, E.M., Reynolds, J.S.*, Troy, T.L., Paithankar, D.Y., Lopez, G. and J. Lee, "Fluorescence lifetime imaging with measurements of photon migration: theory, simulation, and experiment," IEEE Annual Meeting, Chiacgo, November 1997 *(invited).*

Troy, T.L., Reynolds, J.S., and E.M. Sevick-Muraca, "Photon migration imaging using multi-pixel measurements," Annual Meeting of the American Institute of Chemical Engineers, Los Angeles, CA, November 1997.

Reynolds, J.S.*, Troy, T.L., and E.M. Sevick-Muraca, "Fluorescence lifetime imaging," Eastern Analytical Symposium, New Brunswick, NJ, November 1997 *(invited).*

Mayer, R.H., Reynolds, J.S., and E.M. Sevick-Muraca, "Measurement of fluorescent dye optical properties in scattering media," Annual Meeting of the Biomedical Engineering Society, Case-Western University, Cleveland OH, October 11, 1998.

Troy, T.L., Reynolds, J.S., Thompson, A.B., Mayer, R.H., and E.M. Sevick-Muraca, "Photon migration imaging of fluorescent contrast agents," Annual Meeting of the Biomedical Engineering Society, Case-Western University, Cleveland OH, October 11, 1998.

Multipixel Techniques for Frequency-Domain Photon Migration Imaging

Jeffery S. Reynolds, Tamara L. Troy, and Eva M. Sevick-Muraca*

Photon Migration Laboratory, School of Chemical Engineering, Purdue University,
West Lafayette, Indiana 47907-1283

The ability to map interior optical properties of a highly scattering medium from exterior measurements of light propagation is afforded by optical tomography. In this communication, we describe the problem of optical tomography, the techniques of photon migration measurements necessary to accomplish it, and the development of multipixel measurements for rapid collection of optical signals. These multipixel measurements are shown to provide detection of contrast owing to the optical properties of absorption and fluorescence associated with dye-laden heterogeneities embedded in a tissue-like scattering medium. From these rapid measurements, successful reconstruction of an interior optical property map may now be possible with clinically realistic data acquisition times. Applications for the technology arise for biomedical optical imaging for the *in vivo* detection of disease and the diagnosis of tissue (bio-) chemistry.

Introduction

Electrical impedance, ultrasound, microwave, and optical tomographies involve launching one or more excitation signals at the periphery of a body whose interior contents are under investigation and measuring the emitted signals at a number of detectors or receivers also located on the periphery. Owing to the presence of interior heterogeneities, the spatial propagation of current, sound, microwave, or light between a transmitter and receiver is altered, depending upon the differences in the respective transport properties between interior heterogeneities and their surroundings. Consequently, information regarding interior heterogeneities is contained in the signals detected at the periphery. Tomographic reconstruction usually consists of linearizing the relationship between received signals and the spatial distribution of transport properties to mathematically recover the spatial distribution of properties which yields the best modeled match to the receiver measurements. The result is a tomographic image of the interior distribution of transport properties detailing the presence of heterogeneities.

The feasibility of optical tomography has been best demonstrated using single-pixel measurements of frequency-domain photon migration (O'Leary *et al.*, 1995; Pogue *et al.*, 1995). These point measurements consist of launching sinusoidally modulated light into a highly scattering medium, such as tissue or a particulate suspension, and measuring the modulation phase delay, θ, and amplitude, M, of the emitted light relative to the incident source (Figure 1). Solution of the inverse-imaging algorithm involves iteratively updating a map of optical properties until these "single-pixel" measurements of phase shift, θ, and amplitude demodulation, M, match model predictions. The propagation of intensity modulated light can be predicted from the diffusion equation (Patterson *et al.*, 1989):

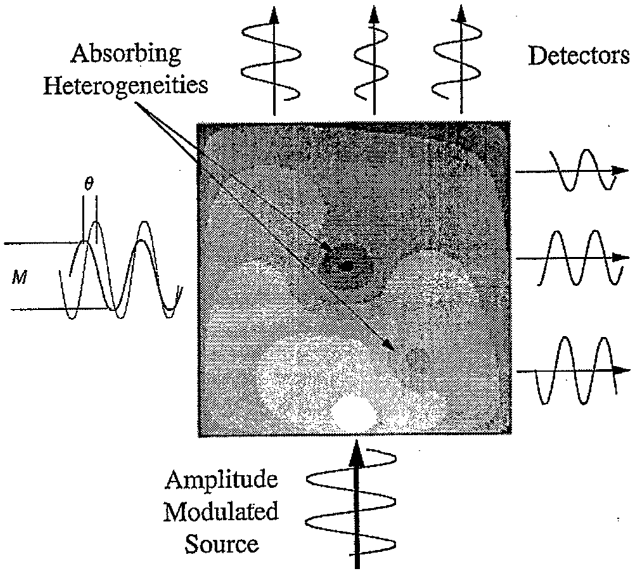

Figure 1. Technique for making frequency-domain measurements is depicted schematically, overlaid on a logarithmic plot of photon fluence or density produced by numerical simulation. White represents high photon density. The medium is assumed to have the typical scatter parameters of breast adipose tissue with two heterogeneities that have a 10× increase in absorption.

$$-\nabla\cdot D(\vec{r})\,\nabla\Phi(\vec{r},\omega) + \frac{i\omega}{c}\Phi(\vec{r},\omega) + \mu_a(\vec{r})\,\Phi(\vec{r},\omega) = S(\vec{r},\omega) \quad (1)$$

where $\Phi(\vec{r}\omega)$ is the ac fluence rate of light at position $\vec{r}$ and modulated at frequency, ω; μ_a is the absorption coefficient responsible for elimination of propagating light by the process of absorption; c is the speed of light in the medium; and D is the optical diffusion coefficient, given by

$$D(\vec{r}) = \frac{1}{3[\mu_a(\vec{r}) + \mu_s'(\vec{r})]} \quad (2)$$

---

* Corresponding author. Phone: (765) 496-2377. FAX: (765) 494-0805. E-mail: sevick@ecn.purdue.edu.

The coefficient, μ_s', is the isotropic scattering coefficient. By employing the proper boundary conditions (Haskell *et al.*, 1994; Patterson *et al.*, 1989), values of the complex ac fluence, $\Phi(\vec{r},\omega)$, can be calculated numerically for arbitrary spatial distributions of the absorption, μ_a, and isotropic scattering, μ_s', coefficients. The modulation phase shift and amplitude at any position can be obtained directly from the complex ac fluence, $\Phi(\vec{r},\omega) = Me^{i\theta}$.

The diffusion approximation describing the propagation of light is valid when photons are predominantly scattered rather than absorbed (i.e., $\mu_a \ll \mu_s'$). This is indeed the case in most tissues, and the diffusion equation has been successfully applied to many problems involving light propagation in biological media. However, in some cases, the more general theory of radiative transfer must be applied (Ishamaru, 1978). In addition, because the absorption coefficient is related to the product of extinction coefficients and the concentration of light absorbing compounds (i.e., $\mu_a = \epsilon[C]$), optical tomography also gives added local information on (bio-) chemical composition. In the case of tissues, the dominant light absorbing species are melanin, water, and deoxy- and oxyhemoglobin.

Typically, optical tomography using frequency-domain photon migration measurements has been used to reconstruct tomographic images in models or phantoms which mimic the scattering properties of tissues. O'Leary and co-workers (1995) have successfully employed the first-order Born scattering approximation to linearize the relationship between detected fluence and spatial distributions of absorption, μ_a, and isotropic scattering, μ_s', coefficients to reconstruct images from experimental, near-infrared measurements. The linearization is valid for small changes in optical properties at vanishingly small point volumes. Pogue and co-workers (1995) have relaxed these restrictions and have also successfully reconstructed images from experimental, frequency-domain photon migration measurements. Their approach uses an iterative approach based upon Newton's method to converge upon maps of absorption and scattering by minimizing the differences between model predictions and measured fluences. These studies provide promising results for the development of optical tomography for biomedical imaging (Jiang *et al.*, 1996; Paulsen and Jiang, 1996). Although future improvements to the inverse imaging solution are certain, two stumbling blocks remain: (i) instrumentation for rapid registration of ac fluence signals and (ii) the availability of endogenous contrast for biomedical optical tomography.

Measurements of ac Fluence for Tomographic Reconstructions. Frequency-domain measurements of photon migration have been demonstrated to frequencies as high as the gigahertz range (Madsen *et al.*, 1994; Fishkin *et al.*, 1996, 1997). However, the attenuation of the modulation envelope increases rapidly at these higher frequencies due to the order of nanosecond photon "time-of-flight" in tissues (Chance *et al.*, 1988). This increased attenuation coupled with decreased detector performance at higher frequencies limits the range of useful modulation frequencies for most biomedical optical imaging applications to between 30 and 200 MHz (Sevick *et al.*, 1992). Typically, transmitters consist of laser diodes biased above the lasing threshold and modulated at frequency, f, by the addition of an rf signal (Chance *et al.*, 1990; Thompson *et al.*, 1992). Alternatively, constant intensity sources can be used when coupled with an acousto-optic modulator or Pockels cell assembly (Gratton and Limkeman, 1983; Piston *et al.*, 1989). Detection of the modulation amplitude and phase at these high modulation frequencies can be challenging. Typically, photomultiplier tube detectors with high gain are employed in heterodyne mode, whereby the voltage across the electron multiplier chain is gain modulated at the modulation frequency, f, of the incident light source plus an offset frequency, Δf, of 100 Hz or more. This mixing results in a current at the anode that is modulated at the frequency, Δf, but contains the information of modulation amplitude and phase shift of the optical signal modulated at frequency f (Spencer and Weber, 1969; Graton and Limkeman, 1983). Other possibilities in which the mixing of the electronic signal occurs after the photomultiplier tube, rather than in its electron multiplier chain, are also possible. The advantage of this heterodyned detection is that simple data acquisition can be used to acquire and evaluate the modulation amplitude and phase shift of the ac fluence detected at a single location. Typically, measurement error in modulation phase and amplitude are 0.1° and 1%, respectively (Barbieri *et al.*, 1989, 1990). The disadvantage for these single-pixel detection systems is that, for a tomographic imaging system, multiple detectors need to be replicated or multiplexed to provide the number of inputs required to solve the inverse imaging problem. Boas and co-workers (1997) report that often the limiting error in inverse solutions for optical tomography arises from uncertainty in detector position typically determined from the positioning of the fiber optic coupling leading from the detector to the air–phantom interface. In this paper we demonstrate multipixel measurements of ac fluence directed for the development of biomedical optical tomography that do not require the positioning of multiple detectors or single detector scanning.

Available Contrast for Tomographic Reconstructions in Tissues. Biomedical optical tomography is successful only if the contrast in the optical properties between heterogeneities and their surroundings are significant enough to cause alteration in measured signals. However, in the work by Troy *et al.* (1996), the endogenous contrast available by tissue scattering was *not* found to be consistently large enough to alter the propagation of light. While their *in vitro* measurements were unable to assess the contrast owing to absorption due to the increased hemoglobin associated with angiogenesis, single-pixel ac measurements suggest that the degree of contrast offered by the presence of a perfect absorber ($\mu_a \rightarrow \infty$) in an unrealistically absorption-free surroundings ($\mu_a = 0$) may still be too small (Sevick-Muraca *et al.*, 1997). Measured phase shifts are altered by less than 6° at 200 MHz and amplitude demodulated by a few percent due to the presence of a perfect light absorbing heterogeneity located in a lossless, highly scattering medium. This is the maximum possible contrast owing to absorption and is physiologically unrealistic. Consequently, another mechanism of contrast imposed by artificial or exogenous methods may be necessary (Sevick-Muraca *et al.*, 1997).

Recently, we have demonstrated that the ac contrast offered by fluorescence exceeds that offered by absorption (Sevick-Muraca *et al.*, 1997). The additional mechanism for contrast arises from the kinetics of the fluorescence decay process. Once a fluorophore absorbs excitation light and undergoes an electronic transition, it remains in an activated state for a mean period of time, known as the lifetime, before relaxation to the ground state and

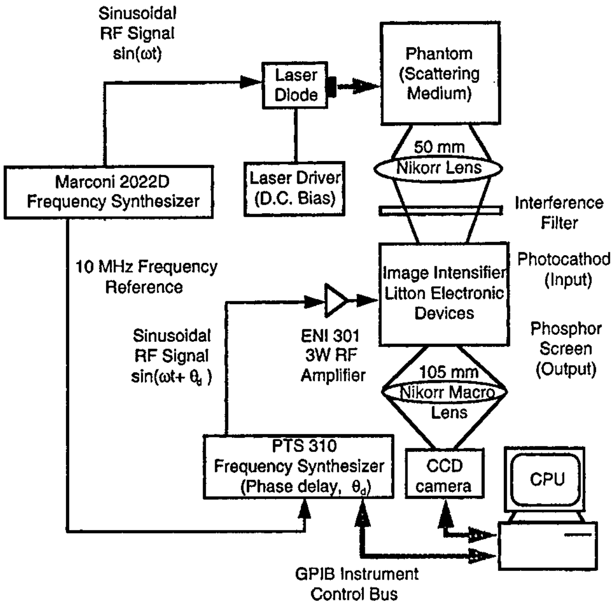

Sinusoidal
RF Signal
sin(ωt)
Laser
Diode
Phantom
(Scattering
Medium)
50 mm
Nikorr Lens
Marconi 2022D
Frequency Synthesizer
Laser Driver
(D.C. Bias)
Interference
Filter
10 MHz Frequency
Reference
Image Intensifier
Litton Electronic
Devices
Photocathode
(Input)
Sinusoidal
RF Signal
sin(ωt+ θd)
ENI 301
3W RF
Amplifier
Phosphor
Screen
(Output)
105 mm
Nikorr Macro
Lens
PTS 310
Frequency Synthesizer
(Phase delay, θd)
CCD
camera
CPU
GPIB Instrument
Control Bus

Figure 2. Apparatus for multipixel frequency-domain photon migration imaging.

re-emission of a fluorescent photon occurs. Typically lifetimes, τ, are on the order of nanoseconds, inducing decades of fluorescent phase shift change and tens of percent of fluorescent amplitude demodulation relative to the incident light. The phase shift and amplitude modulation of the propagated fluorescent light relative to the incident excitation source can be predicted from the coupled diffusion equations for both excitation and emission (fluorescent) light propagation (Patterson *et al.*, 1994; Sevick-Muraca and Burch, 1994; Hutchinson *et al.*, 1996; Reynolds *et al.*, 1997):

$$-\nabla\cdot D_x(\vec{r})\,\nabla\Phi_x(\vec{r},\omega) + \frac{i\omega}{c_x}\Phi(\vec{r},\omega) + \mu_{ax}(\vec{r})\,\Phi_x(\vec{r},\omega) = S_x(\vec{r},\omega) \quad (3)$$

$$-\nabla\cdot D_m(\vec{r})\,\nabla\Phi_m(r,\omega) + \frac{i\omega}{c_m}\Phi_m(\vec{r},\omega) + \mu_{am}(\vec{r})\,\Phi_m(\vec{r},\omega) = \phi\mu_{ax_f}\frac{1-i\omega\tau}{1+(\omega\tau)^2}\,\Phi_x(\vec{r},\omega) \quad (4)$$

where the subscript x denotes the properties and fluence for excitation light and subscript m denotes that for emission light. The absorption coefficient for excitation light, μ_{ax}, is comprised of absorption due to the fluorophore, μ_{ax_f}, as well as that owing to chromophores which do not result in emission of light. The quantum efficiency of the fluorophore is denoted by ϕ. The term on the right-hand side of eq 4 constitutes the source term of emission light and assumes first-order fluorescent decay kinetics.

Tomographic inversion of fluorescent ac measurements using eqs 3 and 4 constitutes a more complicated problem than the nonfluorescent measurements in eq 1. However, the disadvantage of added complexity may be offset by the increased contrast available if enough ac signal can be detected for phase shift and amplitude demodulation measurements. In addition, since the electronic relaxation from activated to ground state can be governed by the local biochemical environment, the local value of lifetime can provide spectroscopic information. Despite the added complexity of fluorescence photon migration, two groups have demonstrated the feasibility of reconstructing lifetime, τ, and the product of quantum yield and fluorophore absorption coefficient, $\phi\mu_{ax_f}$, from simulated measurements (O'Leary *et al.*, 1996; Sevick-Muraca *et al.*, 1996; Paithankar *et al.*, 1997). Experimental measurements remain yet to be performed to confirm the

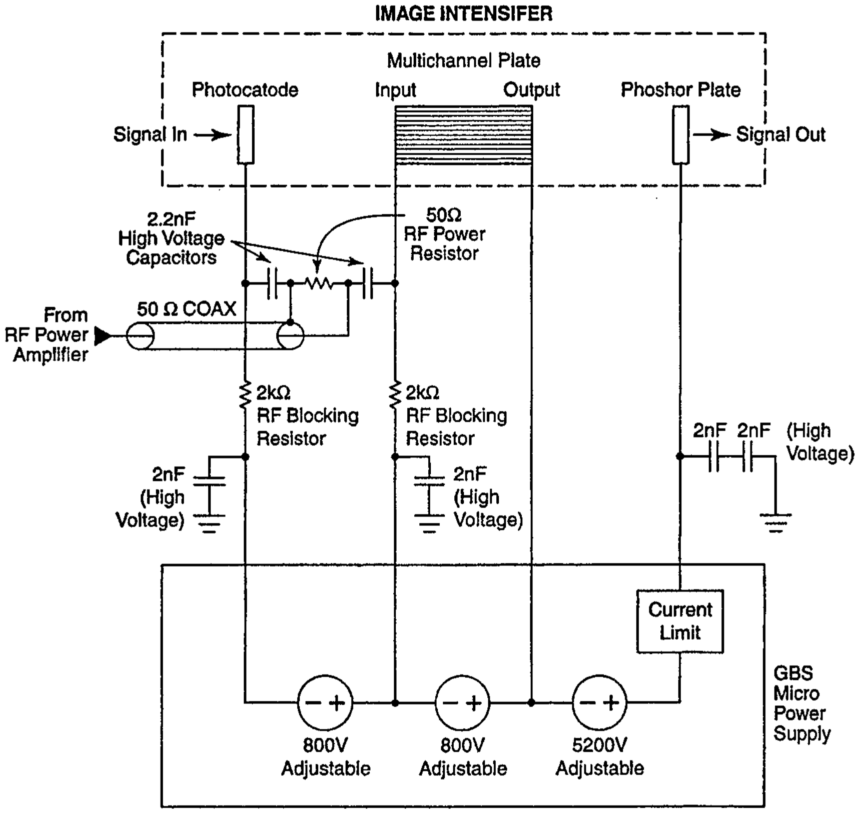

IMAGE INTENSIFER
Multichannel Plate
Photocatode
Input
Output
Phoshor Plate
Signal In
Signal Out
2.2nF
High Voltage
Capacitors
50Ω
RF Power
Resistor
From
RF Power
Amplifier
50 Ω COAX
2kΩ
RF Blocking
Resistor
2kΩ
RF Blocking
Resistor
2nF 2nF (High
Voltage)
2nF
(High
Voltage)
2nF
(High
Voltage)
Current
Limit
GBS
Micro
Power
Supply
800V
Adjustable
800V
Adjustable
5200V
Adjustable

Figure 3. Detailed circuit schematic for the gain-modulated image intensifier.

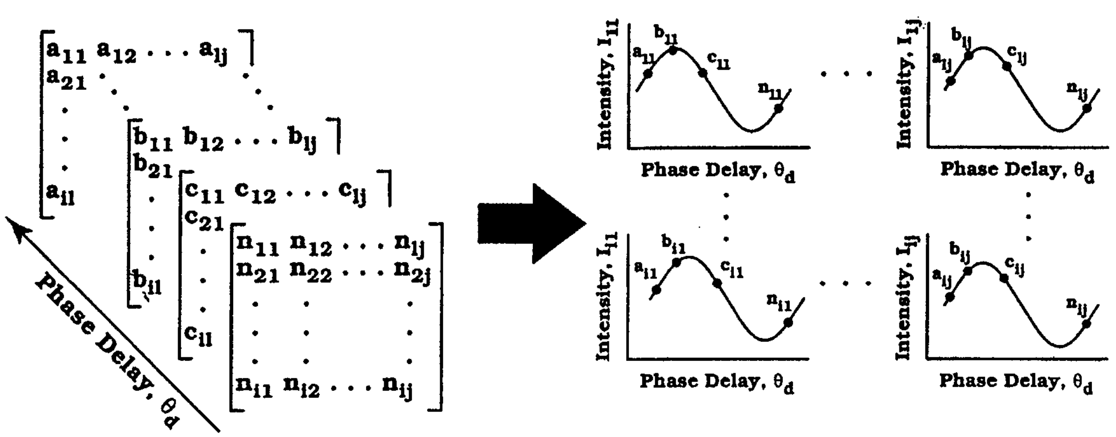

Figure 4. Graphical depiction of homodyne multipixel data acquisition.

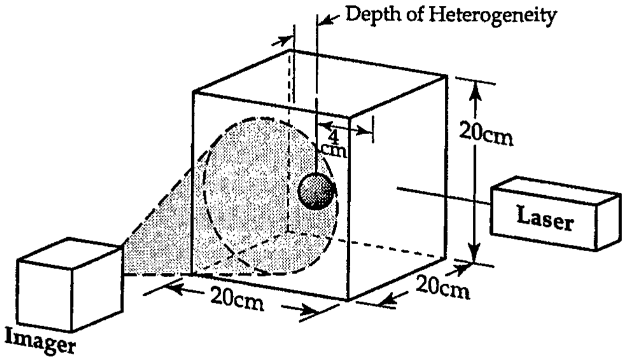

Figure 5. Schematic illustrating the 20 cm cubic tank used for a tissue phantom and the side illumination geometry used for the presented measurements.

feasibility of fluorescence lifetime imaging for biomedical optical imaging with fluorescent contrast agents. Agents such as indocyanine green (ICG) are already approved by the FDA for systemic introduction into the human body and have been shown to provide measurable signals in tissue phantom studies in our laboratory (Sevick *et al.*, 1997). In this work, we extend multipixel measurements to fluorescence measurements with the addition of an interference filter to select the ac component of the fluorescent light. The goal of our multipixel fluorescence measurements is to demonstrate enhanced contrast owing to fluorescence over absorption, even with the reduced fluorescence signal level.

In the following sections, we describe the instrumentation associated with multipixel ac fluence measurements and present ac measurements of diffusing photon density waves propagating in tissue-like scattering media with absorbing and fluorescing heterogeneities. By comparing measurements in the presence and absence of these heterogeneities, we demonstrate the contrast provided by each mechanism as detected with multipixel measurements.

Experimental Technique

Apparatus. The experimental apparatus for multipixel frequency-domain photon migration measurements is shown schematically in Figure 2 (Troy *et al.*, 1997). A collimated and circularized laser diode (Melles Griot model 06DLS403, 789 nm, 30 mW; model 06DLS503, 836 nm, 40 mW) illuminates the scattering phantom with a sinusoidally amplitude modulated signal. The diode is maintained at a constant dc bias midpoint above threshold by a Melles Griot model 06DLD203 laser diode driver which also maintains the diode at a constant temperature. A 13 dBm (20 mW) sinusoidal rf signal (Marconi 2022D frequency synthesizer) is superimposed on the constant dc current through a bias network internal to the laser diode (Thompson, 1992). The scattered signal from the phantom is focused onto the photocathode of the image intensifier by a 50 mm Nikorr camera lens. This lens is positioned so that the 18 mm diameter of the intensifier photocathode has a field of view of approximately 80 mm. An optical interference filter can be inserted at the input of the image intensifier to separate fluorescent and excitation light. The weak near-infrared signal at the photocathode is converted to an electronic image which is amplified by the image intensifier's microchannel plate and converted to a visible optical image when the amplified electrons strike the phosphor output plate. The 18 mm diameter optical output of the intensifier is then coupled to a $1/2$ in. CCD array with a 105 mm Nikorr microlens. Coupling with a tapered fiber optic face plate would be more efficient and compact, but lens coupling allows for both the use of a mechanical shutter in front of the CCD array and direct viewing of the intensifier output with the naked eye during alignment and testing. The CCD camera (Photometrics AT200) has a resolution of 512 × 512 pixels with a 16 bit dynamic range.

The heart of this instrument is a gain-modulated image intensifier. The intensifier and a detailed schematic of its bias network are shown in Figure 3. The image intensifier is an 18 mm diameter Generation III device (Litton Electronic Devices model 510-5916-310) and is similar to those found in common military and commercial night vision systems. Generation III image intensifiers are characterized by their extended near-infrared response, high gain, and high resolution. This particular image intensifier has a photocathode sensitivity of 209 mA/W at 830 nm and 103 mA/W at 880 nm, a current gain of 27 500, and a resolution of 45 lp/mm. An adjustable high-voltage power supply (GBS Micro Power Supply model PS20060500) provides all the dc high voltages to the image intensifier as well as a phosphor screen current limiting protection circuit which shuts down the intensifier when the incident light level reaches a potentially damaging level. A sinusoidal rf modulation voltage is superimposed on the normal dc high-voltage bias on the image intensifier's photocathode through high-voltage isolation capacitors. The rf modulation is typically a 50 V peak-to-peak sinusoid which is provided by an ENI model 604L 4 W linear rf power amplifier. Because the ENI amplifier will drive an open circuit, the 50 Ω power resistor can be removed from the circuit to increase the maximum rf voltage which can be supplied to the intensifier. Since the gain of the image intensifier is essentially proportional to applied voltage, the resulting gain of the image intensifier is also modulated at the

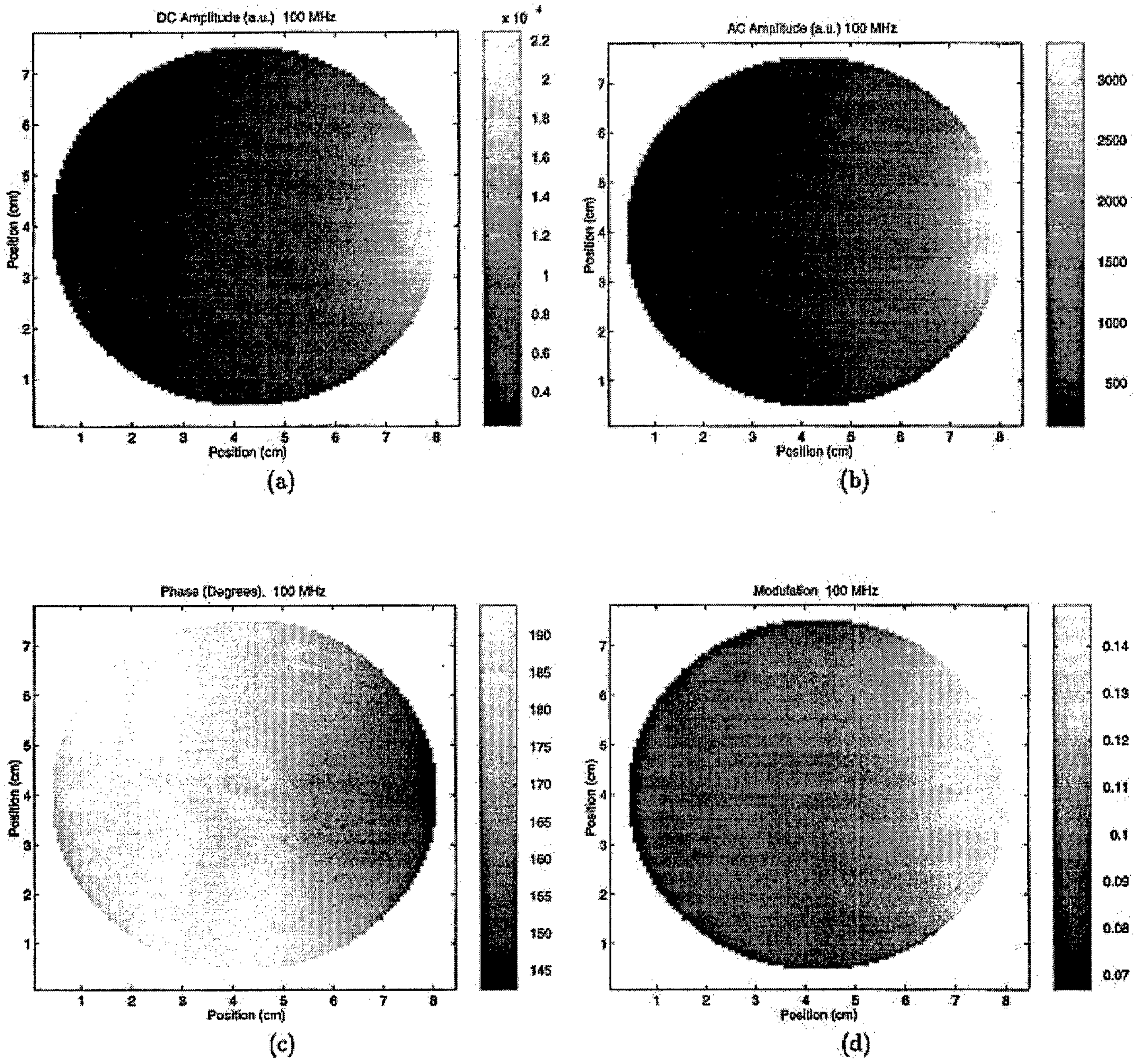

Figure 6. Multi-pixel image of a homogeneous phantom with 836 nm side illumination (as in Figure 5) and a 100 MHz modulation frequency. Image a is the average or dc pixel intensities; image b is the ac pixel intensities; image c is the modulation phase at each pixel; and image d is the modulation ratio.

applied rf. Given a modulated optical signal at its input, the image intensifier will act as a multichannel rf mixer across its field of view. Similar instrumentation has been developed for fluorescence lifetime imaging in nonscattering media by Lakowicz and Berndt (1991).

Data Acquisition and Signal Processing. In the application of frequency-domain imaging, the gain-modulated intensifier can be used in one of two modes. In the heterodyne mode, the image intensifier is modulated at a frequency $f + \Delta f$, offset from the laser source by Δf. The difference frequency must be within the frequency response of the phosphor output of the intensifier (~30 Hz) and the readout rate of the CCD array. The rf amplitude and phase at a given pixel is then regressed from the magnitude and phase of the variation of the pixel intensity at the frequency Δf. In the homodyne mode, the intensifier is driven at the same frequency as the optical source. Here the image produced is a steady-state image with no time variation. Rf amplitude and phase are determined by varying the phase of the intensifier relative to the phase of the excitation light and then fitting a sinusoid to the measured data. Homodyning has the advantage that the image at the output of the intensifier is steady-state so that the read out rate of the CCD array can be arbitrarily slow. For this reason we use the homodyne method when taking data. However, since we can see the output of the intensifier directly, we use the heterodyne method with $\Delta f \sim 3$ Hz to optimize the ac and dc drive voltages to the intensifier by maximizing the Δf flicker at the output of the intensifier.

In our homodyne technique, the phase delay, θ_d, is introduced by a frequency synthesizer (Programmed Test Sources model PTS 310) which is phase locked to second synthesizer (Marconi model 2022A) via a 10 MHz phase reference signal, ensuring that the two synthesizers will operate at exactly the same frequency with a constant phase difference. The phase of the PTS 310 synthesizer relative to the Marconi can then be controlled digitally from 0 to 360° via an IEEE-488 GPIB instrument control bus. A homodyned rf amplitude and phase picture is then obtained by stepping the phase delay at a regular interval from 0 to 360° and acquiring a CCD image of the intensifier phosphor screen at each phase delay, as

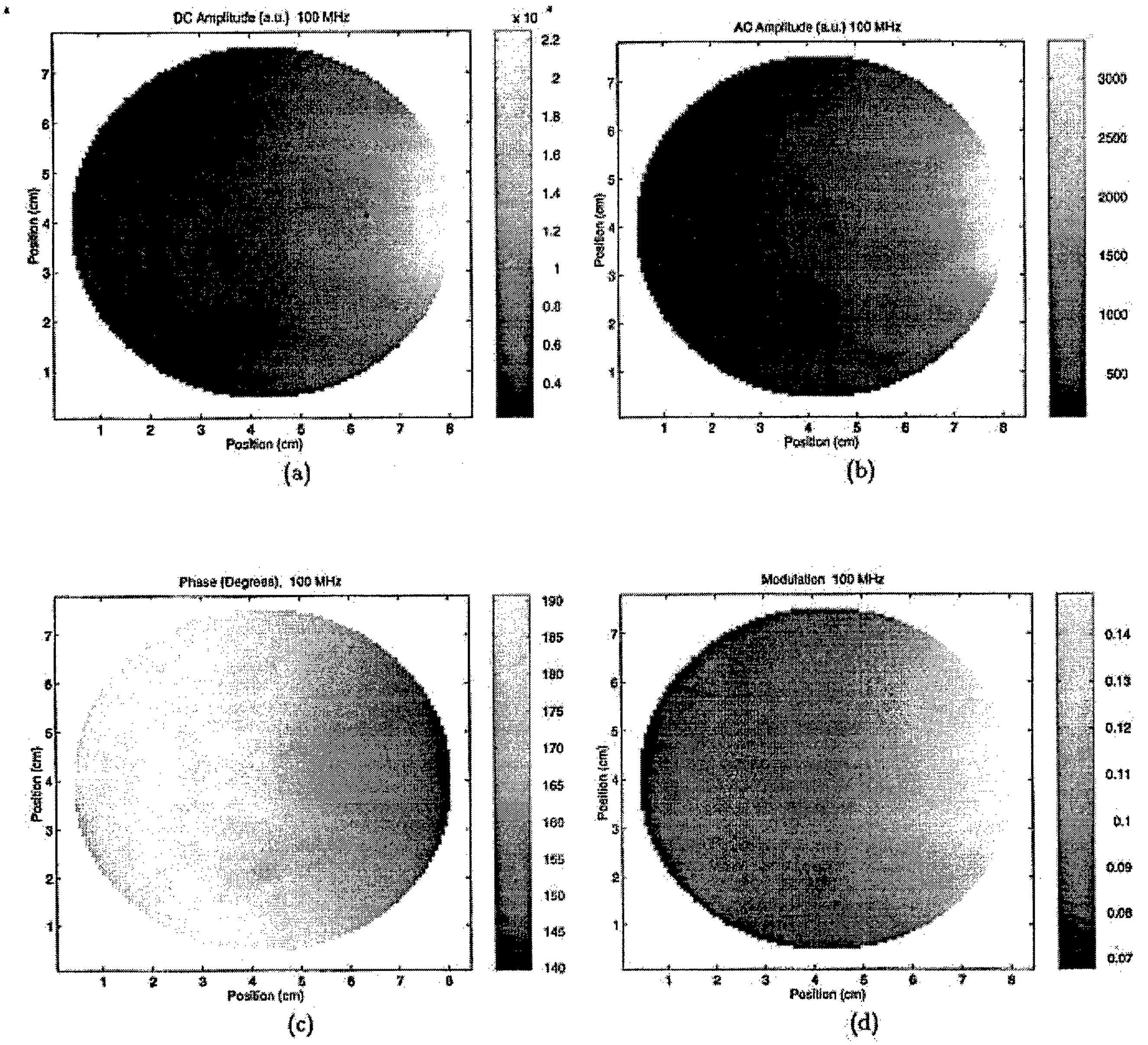

(a) (b)

(c) (d)

Figure 7. Multi-pixel image of a phantom with three absorbing beads of diameters 4, 6, and 8 mm with 836 nm side illumination (as in Figure 5) and 100 MHz modulation frequency. Image a is the average or dc pixel intensities; image b is the ac pixel intensities; image c is the modulation phase at each pixel; and image d is the modulation ratio.

illustrated in Figure 4. A single CCD image for a given relative phase shift is represented by a matrix with each *ij*th element representing a single pixel. The intensity at a given pixel will vary over a single sinusoid cycle as the phase delay is varied over 360° as can be seen in Figure 4. Once this series of images is recorded, the measurement is complete. A simple and fast data analysis algorithm is then applied to extract the pixel by pixel intensity and phase data. The dc value is computed by taking the average pixel intensity for all phase delays. The ac component of the pixel intensity is then isolated by subtracting this dc value from the total pixel intensity at each phase delay. This pixel ac intensity as a function of phase delay is Fourier transformed using a Fast Fourier Transform (FFT). Since each pixel intensity varies over exactly one period, the maximum of the digital frequency spectrum calculated by the FFT will be found at the first element of the digital frequency spectrum and will correspond to the frequency component of the optical signal at the modulation frequency for a given pixel. This complex number is then used to calculate the pixel phase (θ) and rf amplitude (A) by the simple relationships:

$$\theta = \arctan\left(\frac{Im\{I(f_{\max})\}}{Re\{I(f_{\max})\}}\right) \tag{5}$$

and

$$A = \frac{[(Im\{I(f_{\max})\})^2 + Re\{I(f_{\max})\})^2]^{1/2}}{(N/2)} \tag{6}$$

where $I(f)$ is the Fourier transform of the measured intensity versus phase delay, $I(\theta_d)$, and N is the number of phase delays. Modulation ratio is simply the ratio of the ac pixel intensity to the dc pixel intensity, $M =$ ac/dc. The FFT algorithm is an efficient way to find the ac component of the pixel intensity. Ac magnitude and phase values can be calculated approximately 100 times faster than by using a nonlinear least-squares fit of the data to a sinusoid. The FFT algorithm is most efficient when dealing with $N = 2^n$ data points, where n is an

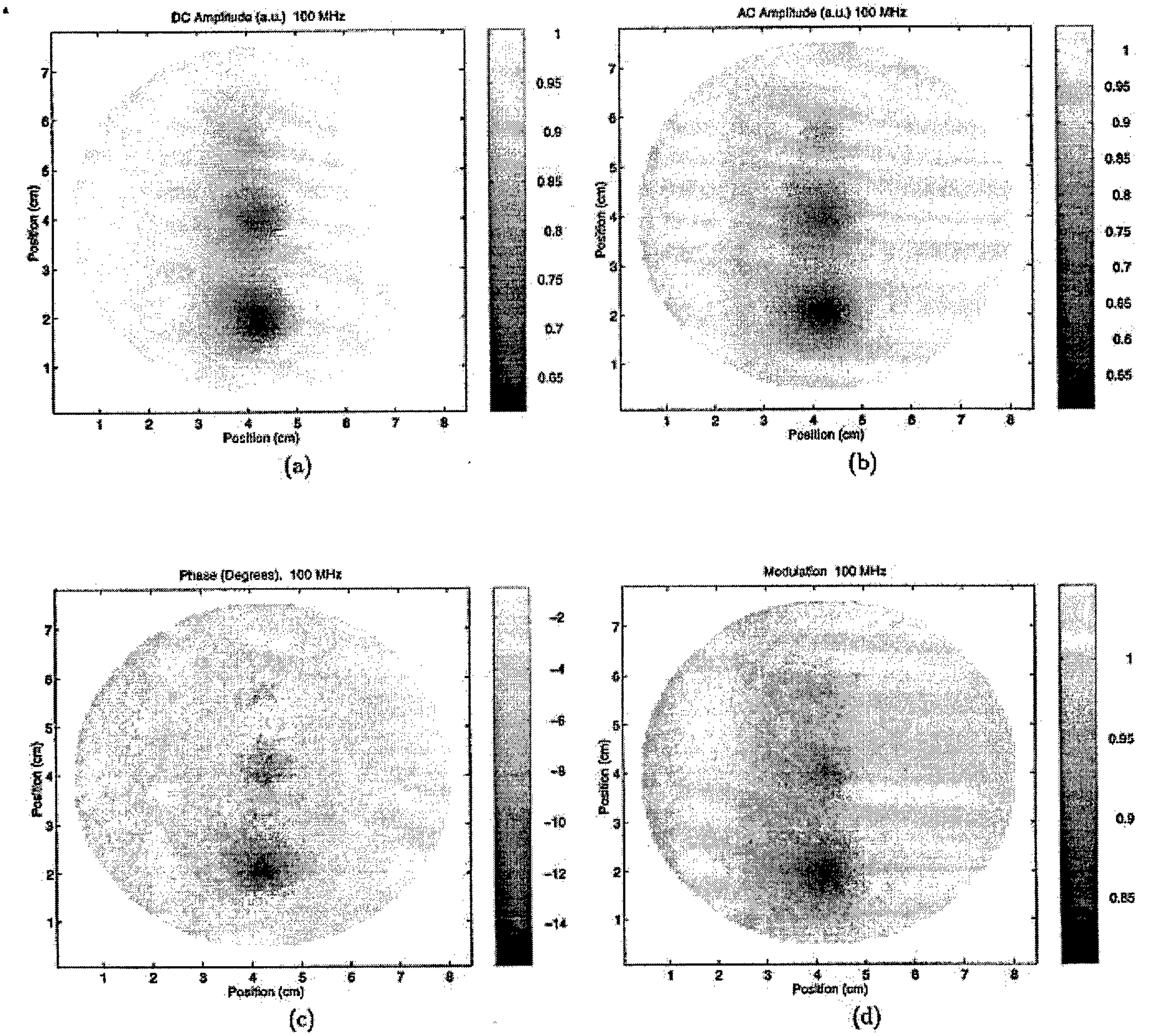

Figure 8. Multi-pixel ratio images (presence/absence) for three absorbing beads of diameters 4, 6, and 8 mm with 836 nm side illumination (as in Figure 5) and a 100 MHz modulation frequency. Image a is the average or dc pixel ratios ($dc_{\mathrm{presence}}/dc_{\mathrm{absence}}$); image b is the ac pixel ratios ($ac_{\mathrm{presence}}/ac_{\mathrm{absence}}$); image c is the modulation phase difference ($\theta_{\mathrm{presence}} - \theta_{\mathrm{absence}}$) pixel; and image d is the modulation ratio ($M_{\mathrm{presence}}/M_{\mathrm{absence}}$).

integer. For that reason we use either 32 or 64 phase steps when taking our data.

The entire measurement procedure is automated. A personal computer steps the phase of the PTS 310 via IEEE-488 bus and acquires a CCD image at each phase delay, θ_d. Typically, three images are taken at each phase delay and averaged. The data are then stored to disk before stepping the phase delay and repeating. For the measurements recorded here, the CCD array is binned by a factor of 8 for a pixel resolution of 128 × 128. Typical exposures for our measurements range from 10 to 1000 ms, but measurement times are limited by the array readout time. Newer CCD arrays are capable of readout times on the order of 0.1 s with comparable resolution and pixel dynamic range. The data acquisition time for a series of 100 ms exposures would be approximately equal to the (exposure time + frame transfer time) × (number of phase delays) × (number of pictures per phase delay) = $(0.1 + 0.1) \times 64 \times 3 = 384$ s. This corresponds to an equivalent acquisition time for data acquired using "single-pixel" techniques of the order $T \times 128 \times 128$, where T is the aquisition time required to achieve a similar signal to noise ratio with the single-channel detector. Our laboratory experience indicates that at these signal levels, single-channel aquisition times would be on the order of 10 s/pixel, excluding mechanical scan time. Thus, the total single-pixel aquisition time would be on the order of 160 000 s—over 400 times slower than this multipixel acquisition system.

Multipixel Images and Discussion

To test the effectiveness of the multipixel technique for frequency-domain photon migration imaging, we imaged a number of tissue mimicking scattering phantoms with both absorbing and fluorescing heterogeneities. All multipixel images presented in this paper are made directly from 128 × 128 pixel experimental images with no smoothing, interpolating, or any other image processing. The tissue phantom and side illumination geometry that we used in our experiments is shown in Figure 5. The phantom is a $20 \times 20 \times 20$ cm^3 acrylic tank which was filled with a 0.5% by volume Intralipid (Kabi Pharmacia, Inc.) scattering solution which has an isotropic scattering coefficient of approximately 5.7 cm^{-1} at

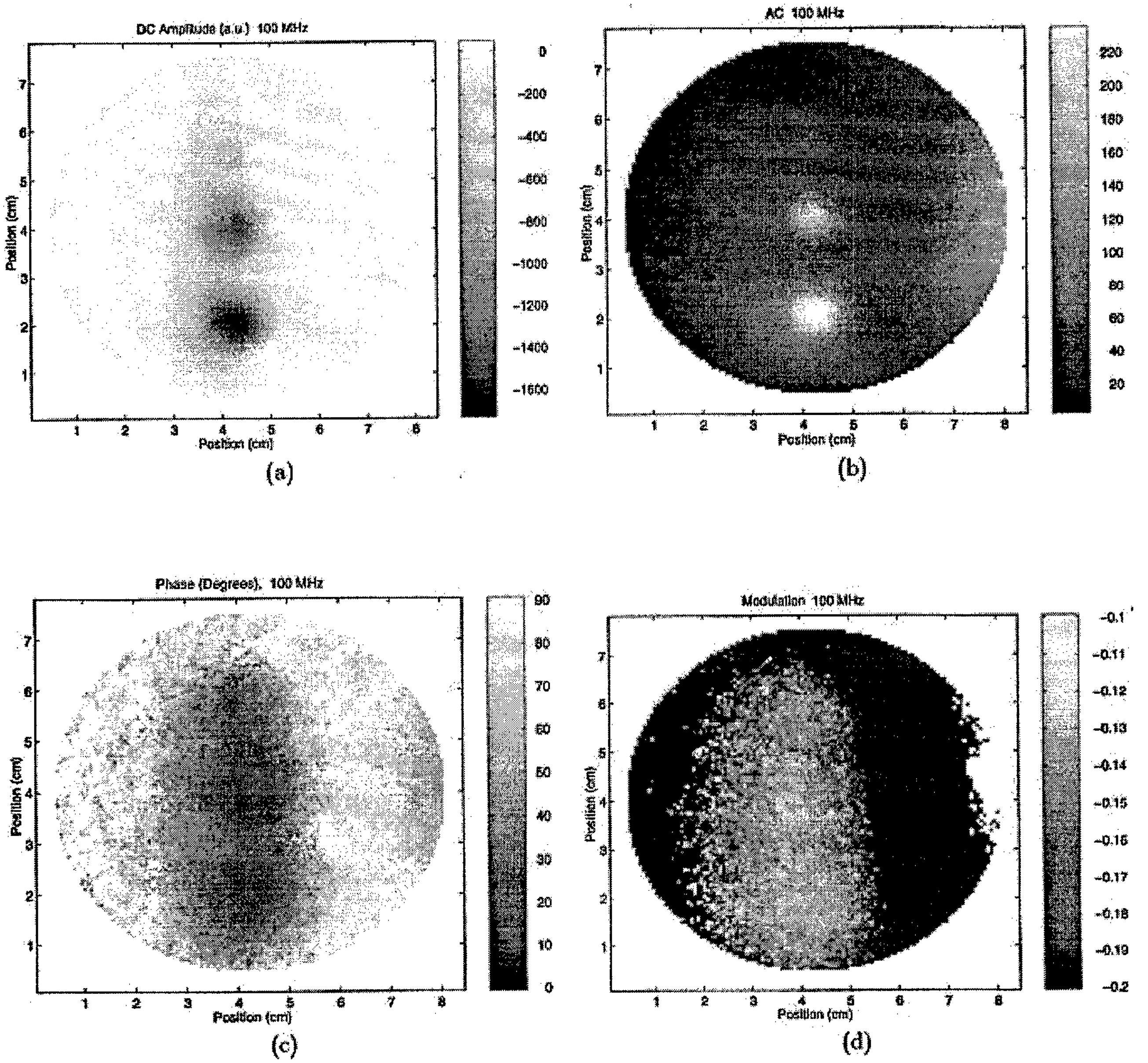

Figure 9. Multi-pixel difference images (presence − absence) for three absorbing beads of diameters 4, 6, and 8 mm with 836 nm side illumination (as in Figure 5) and a 100 MHz modulation frequency. Image a is the average or dc pixel ratios ($dc_{\text{presence}} - dc_{\text{absence}}$); image b is the ac amplitude of the complex difference for presence − absence; image c is the modulation phase of the complex difference for presence − absence; and image d is the modulation of the complex difference for presence − absence.

a wavelength of 789 nm (van Staveren *et al.*, 1991). Used clinically as an intravenous nutrient, Intralipid is a milky looking fat emulsion that mimics the scattering properties of tissue (Driver *et al.*, 1989; van Staveren *et al.*, 1991; Flock *et al.*, 1992). Calibration of the spatial axes for all of the images is achieved by imaging a ruler on the face of the phantom before making measurements.

Absorption Imaging. Figure 6 illustrates the photon migration images for a homogeneous tissue phantom (no heterogeneity) with 836 nm, 40 mW excitation and 100 MHz modulation. Figure 6a shows the dc or average pixel intensities; part b is the ac amplitude or modulation envelope for each pixel; part c is the pixel modulation phases; part d is the modulation ratio for each pixel (ac/dc) or part b/part a. Moving from right to left across the images, the dc and ac intensities as well as modulation ratio all gradually decrease as the distance from the source on the right side (at $x = 8$ cm and $y = 4$ cm) of the phantom increases. Conversely, the phase delay of the optical signal increases with increasing distance from the source. These images are consistent with a diffusing photon density wave emanating from a point source. Also note that the data plots are circular because the field stop for the multipixel imager is set by the image intensifier which has a circular cross section.

To quantify the noise level at each pixel, a slice was taken horizontally across the data for each plot in Figure 6. Since this is a homogeneous scatterer, all ac and dc fluence profiles should have smoothly varying spatial profiles which are predicted by the diffusion equation. By subtracting this fitted smooth profile from the experimental data, one obtains a measure of the noise at each pixel. This noise can be quantified as the standard error by computing the root mean square of the difference signal and dividing by the square root of the number of pixels sampled. Using this aproach on the 100 MHz data for the homogeneous phantom, the standard errors are ±1.5% for the dc, ±1.8% for the modulation amplitude, ±0.2° for the modulation phase, and ±0.6% for the modulation ratio.

The data illustrated in Figure 7 are for a similar experiment, but with three black beads 4, 6, and 8 mm in diameter suspended 1 cm from the front (inside) surface of the phantom and 4 cm from the source. The

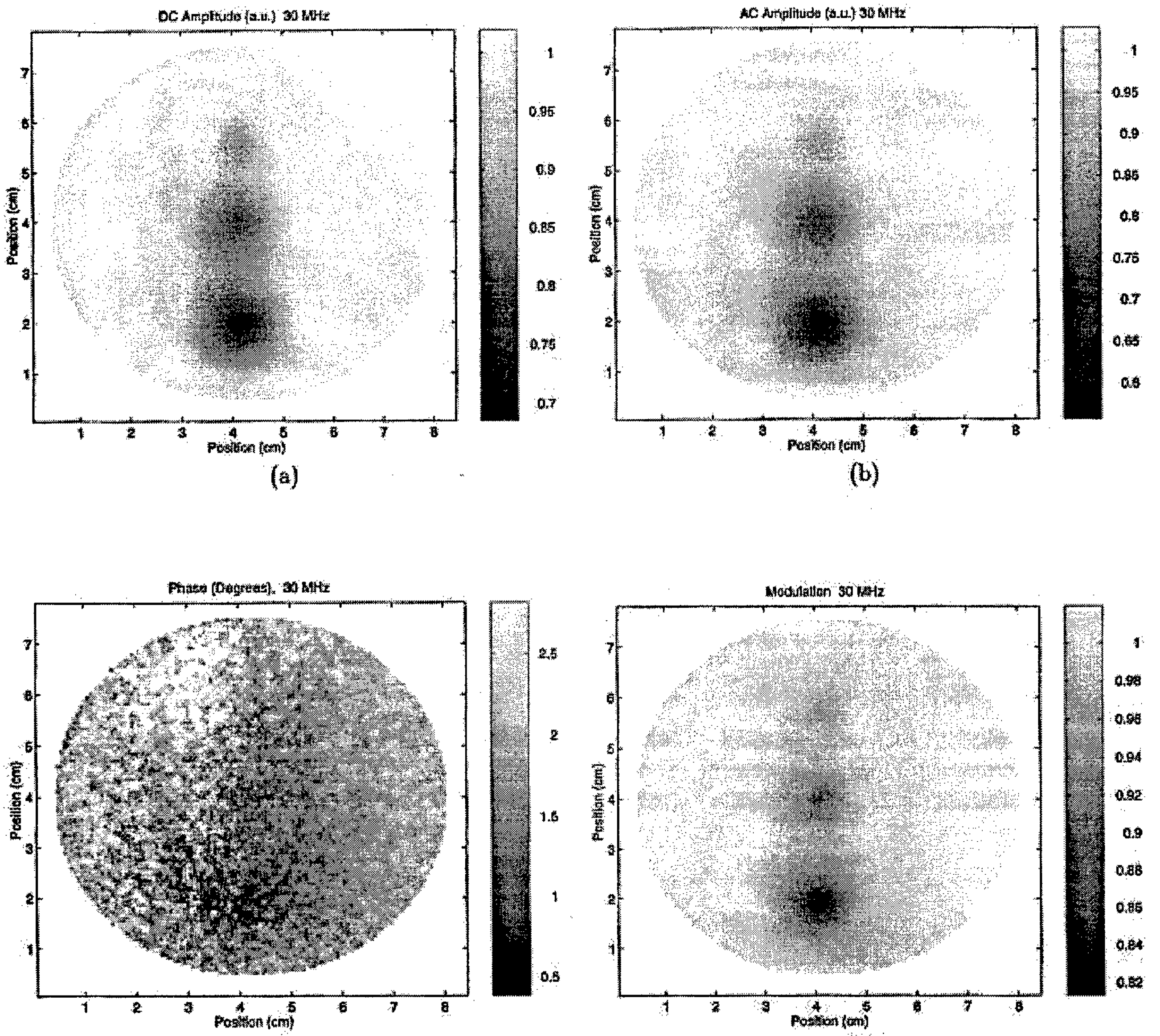

(a) (b) (c) (d)

Figure 10. Multi-pixel ratio images (presence/absence) for three absorbing beads of diameters 4, 6, and 8 mm with 836 nm side illumination (as in Figure 5) and a 30 MHz modulation frequency. Image a is the average or dc pixel ratios ($dc_{\text{presence}}/dc_{\text{absence}}$); image b is the ac pixel ratios ($ac_{\text{presence}}/ac_{\text{absence}}$); image c is the modulation phase difference ($\theta_{\text{presence}} - \theta_{\text{absence}}$) pixel; and image d is the modulation ratio ($M_{\text{presence}}/M_{\text{absence}}$).

shadow from the beads is faintly visible in all four images. To further illustrate the contrast resulting from the heterogeneities, the bead images are ratioed to the "absence" case illustrated in Figure 6 and presented in Figure 8. Here the modulation ratio ($M_{\text{presence}}/M_{\text{absence}}$) and phase difference ($\theta_{\text{presence}} - \theta_{\text{absence}}$) are plotted. Although a "presence" and "absence" case of a disease are not clinically feasible, we use this to illustrate the contrast that would be available for tomographic reconstruction algorithms which would use only the presence data. The degree of contrast can also be assessed by taking the complex difference between the "presence" and "absence" data. The difference signal can then be thought of as the "scattered" signal from the heterogeneity. This calculation is shown in Figure 9. Again, the contrast can be clearly seen in the signal scattered from the heterogeneity.

To show the effect of changing modulation frequency, a presence/absence image for the same phantom is depicted in Figure 10 with a modulation frequency of 30 MHz. The effect of reduced modulation frequency can be clearly seen. As expected, the dc image looks similar but the ac-dependent images are different. However, the longer wavelength of the "photon density wave" associated with the lower modulation frequency results in a much lower phase shift induced by the absorbers. The phase noise of the detection process then becomes comparable to the phase shift caused by the heterogeneities, and the contrast may be insufficient for image reconstruction using the presence data alone.

Fluorescence Imaging. Heterogeneities consisting of fluorescent dyes were imaged in the phantom to demonstrate the performance of the imager and investigate the contrast offered by fluorescence. The excitation source for these experiments is the 789 nm laser diode modulated at 60 MHz. The emission light is separated from the excitation light using an interference filter with a 10 nm bandpass centered at 830 nm (CVI Laser Corp. model F10-830-4-100). The heterogeneities consist of micromolar concentrations of the fluorescent dye ICG contained in a 10 mm tall, 4 mm diameter glass cylinder filled with 0.5% Intralipid scattering solution. The heterogeneity is located 1 cm from the front surface of the phantom and 4 cm from the source. ICG has a

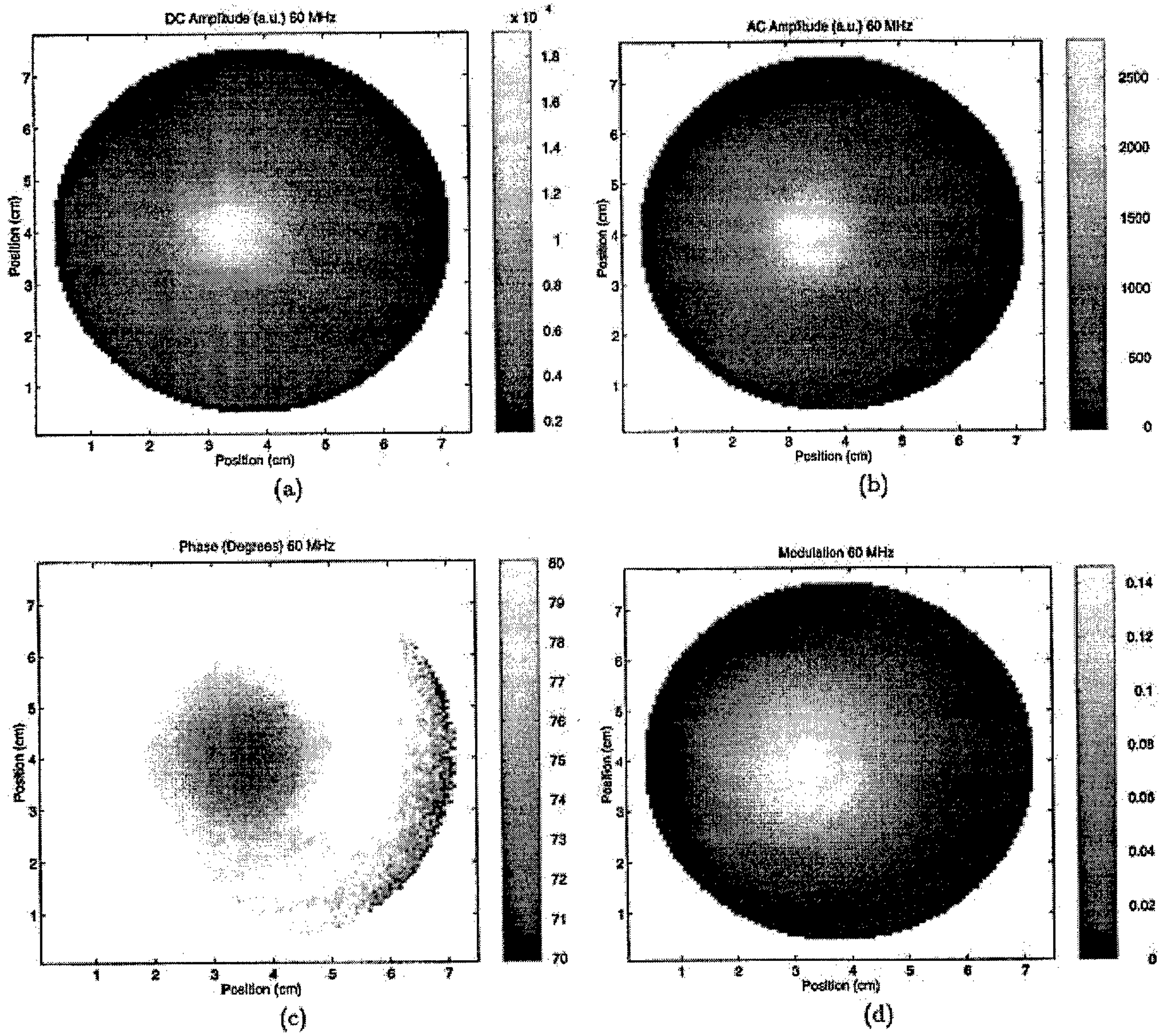

(a) (b)

(c) (d)

Figure 11. Multi-pixel image of a tissue phantom with a 10 mm tall × 4 mm diameter glass cylinder filled with a 2 μM concentration of ICG in 0.5% Intralipid. The emission image is at 830 nm with 789 nm side illumination (as in Figure 5) and a 60 MHz modulation frequency. Image a is the average or dc pixel intensities; image b is the ac pixel intensities; image c is the modulation phase at each pixel; and image d is the modulation ratio.

reported absorption cross section at 780 nm of ϵ = 130 000 (M cm)$^{-1}$, a quantum efficiency for 780−830 nm conversion of $\phi = 0.016$, and fluorescent time decay of τ = 0.56 ns (Sevick *et al.*, 1997). Because of the reduced signal level associated with fluorescence, we used 1000 ms exposure times. Figure 11 shows the images resulting from a 2 μM concentration of ICG. A 2 μM concentration of ICG is approximately 50−75 times below its lethal level and is on the order of that used clinically for photodynamic agents. Because of the inherent contrast offered by fluorescence, the object is clearly visible without referencing to the absence case.

Conclusion

We have demonstrated an efficient method for making high resolution multipixel measurements of frequency-domain diffusing photon density waves using a gain-modulated image intensifier. This high resolution is critical in making measurements for tomographic reproductions because frequency-domain measurements are essentially the near field diffraction pattern resulting from the propagation of diffusing photon density waves, and just as in near-field optical microscopy, imaging resolution is directly related to the measurement resolution. We obtain two-dimensional maps of modulation magnitude and phase as well as dc intensity with 128 × 128 pixel resolution in under 7 min. The equivalent single-pixel data acquisition time would be on the order of 40 h, not counting mechanical scan time. In addition, because there is no mechanical scanning, the multipixel measurement system has much lower positioning errors which have been identified as the limiting noise factor in scanning single-pixel measurements (Boas *et al.*, 1997).

The increased gain, resolution, and near-infrared response of Generation III image intensifiers allow detection and localization of smaller heterogeneities at greater depths in tissue mimicking phantoms. In addition, the extended infrared response also allows measurements to be made over a wider range of the near-infrared biological window. This provides more spectroscopic data and also allows for low loss propagation at both the excitation and emission wavelength when imaging fluorescence. In addition, any exogenous fluorescent contrast agent operating in this near-infrared window will not be competing with endogenous fluorescence which is generally excited by ultraviolet and blue light.

Currently, we are working on adapting our excitation and fluorescent tomographic inversion algorithms to accept the wealth of data that we obtain from our multipixel measurements. This rapid data acquisition coupled with improved inversion algorithms, ever increasing computational speeds, and exogenous contrast agents will hopefully produce a new and extremely powerful biomedical imaging modality.

Acknowledgment

This work was supported in part by the National Institute of Health Grants R01CA67176, R01CA61413, and K04CA68374.

Notation

$\vec{r}$	position (cm)
t	time (s)
f	modulation frequency (1/s or Hz)
Δf	offset in modulation frequency (1/s or Hz)
ω	modulation angular frequency = $2\pi f$ (rad/s)
c	speed of light (cm/s)
i	imaginary number, $(-1)^{1/2}$
$\mu_{\mathrm{a}}(\vec{r})$	absorption coefficient or inverse mean free path (1/cm)
$\mu_{\mathrm{ax}}(\vec{r})$	absorption coefficient at excitation wavelength (1/cm)
$\mu_{\mathrm{ax_f}}(\vec{r})$	fluorophore absorption coefficient at excitation wavelength (1/cm)
$\mu_{\mathrm{am}}(\vec{r})$	absorption coefficient at emission wavelength (1/cm)
$\mu_{\mathrm{s}}'(\vec{r})$	isotropic scattering coefficient or inverse mean free path (1/cm)
$\mu_{\mathrm{sx}}'(\vec{r})$	isotropic scattering coefficient at excitation wavelength (1/cm)
$\mu_{\mathrm{sm}}'(\vec{r})$	isotropic scattering coefficient at emission wavelength (1/cm)
$\Phi(\vec{r}, t)$	fluence or angle integrated photon flux (W/cm^2)
$D(\vec{r})$	optical diffusion constant (cm)
$S_{\mathrm{x}}(\vec{r}, t)$	power density source at excitation wavelength (W/cm^3)
ϕ	quantum efficiency for excitation to emission conversion
τ	exponential time constant for fluorescence (s)
θ	modulation phase (deg or rad)
θ_{d}	phase delay between intensifier and laser diode modulation (deg or rad)
M	modulation amplitude (W/cm^2)
$[C]$	molar concentration (M)
ϵ	extinction coefficient $[(\mathrm{M\ cm})^{-1}]$

Literature Cited

Barbieri, B.; DePiccoli, F.; Gratton, E. Synthesizers' phase noise in frequency domain fluorometry. *Rev. Sci. Instrum.* **1989**, *60*, 3201–3206.

Barbieri, B.; DePiccoli, F.; vandeVen, M.; Gratton, E. What determines the uncertainty of phase and modulation measurements in frequency domain fluorometry. *Proc. SPIE* **1990**, *1204*, 158–170.

Boas, D. A.; O'Leary, M. A.; Chance, B.; Yodh, A. G. Detection and characterization of optical inhomogeneities with diffuse photon density waves: a signal-to-noise analysis. *Appl. Opt.* **1997**, *36*, 75–92.

Chance, B.; Leigh, J.; Miyake, H.; Smith, D.; Nioka, S; Greenfeld, R.; Finander, M.; Kaufman, K.; Levy, W.; Young, M.; Cohen, P.; Yoshioka, H.; Boretsky, R. Comparison of time-resolved and -unresolved measurements of deoxyhemoglobin in brain. *Proc. Natl. Acad. Sci. U.S.A.* **1988**, *85*, 4971–4975.

Chance, B.; Maris, M.; Sorge, J.; Zhang, M. A phase modulation system for dual wavelength difference spectroscopy of hemoglobin deoxygenation in tissues. *Proc. SPIE* **1990**, *1204*, 481–491.

Driver, I.; Feather, J. W.; King, P. R.; Dawson, J. B. The optical properties of aqueous suspensions of Intralipid, a fat emulsion. *Phys. Med. Biol.* **1989**, *34*, 1927–1930.

Fishkin, J. B.; Fantini, S.; Vandeven, M. J.; Gratton, E. Gigahertz photon density waves in turbid media: Theory and Experiments. *Phys. Rev. E.* **1996**, *53*, 2307–2319.

Fishkin, J. B.; Coquoz, O.; Anderson, E. R.; Brenner, M.; Tromberg, B. J. Frequency domain photon migration measurements of normal and malignant tissue optical properties in a human subject. *Appl. Opt.* **1997**, *36*, 10–20.

Flock, S. T.; Jacques, S. L.; Wilson, B. C.; Star, W. M.; Marijnissen, J. P. A.; Prahl, S. A. Optical properties of Intralipid: A phantom medium for light propogation studies. *Lasers Surg. Med.* **1992**, *12*, 510–519.

Gratton, E. and Limkeman, M. A continuously variable frequency cross-correlation phase fluorometer with picosecond resolution *Biophys. J.* **1983**, *12*, 315–324.

Haskell, R. C.; Svaasand, L. O.; Tsay, T.-T.; Feng, T.; McAdams, M. S.; Tromberg, B. J. Boundary conditions for the diffusion equation in radiative transfer. *J. Opt. Soc. Am. A* **1994**, *11*, 2727–2741.

Hutchinson, C.; Troy, T.; Sevick-Muraca, E. Fluorescence-lifetime determination in tissues or other scattering media from measurements of excitation and emission kinetics. *App. Opt.* **1996**, *35*, 2325–2332.

Ishimaru, A. *Wave Propagation and Scattering in Random Media*; Academic Press: New York, 1978.

Jiang, H.; Paulsen, K. D.; Osterberg, U. L.; Pogue, B. W.; Patterson, M. S. Optical image reconstruction using frequency domain data: simulations and experiments. *J. Opt. Soc. Am. A* **1996**, *13*, 253–266.

Lakowicz, J.; Berndt, K. Lifetime-selective fluorescence imaging using an rf phase-sensitive camera. *Rev. Sci. Instrum.* **1991**, *62*, 1727–1734.

Madsen, S.; Anderson, E.; Haskell, R.; Tromberg, B. Portable, high-bandwidth frequency domain photon migration instrument for tissue spectroscopy. *Opt. Lett.* **1994**, *19*, 1934–1936.

O'Leary, M.; Boas, D.; Chance, B.; Yodh, A. Experimental images of heterogeneous turbid media by frequency-domain diffusion-photon tomography. *Opt. Lett.* **1995**, *20*, 426–428.

O'Leary, M.; Boas, D.; Chance, B.; Yodh, A. Fluorescence lifetime imaging in turbid media. *Opt. Lett.* **1996**, *21*, 158–160.

Patterson, M. S.; Pogue, B. W. Mathematical model for time-resolved and frequency-domain fluorescence spectroscopy in biological tissues. *Appl. Opt.* **1994**, *33*, 1963–1974.

Patterson, M. S.; Chance, B.; Wilson, B. Time resolved reflectance and transmittance for the noninvasive measurement of tissue optical properties. *Appl. Opt.* **1989**, *28*, 2331–2336.

Paithankar, D. Y.; Chen, A. U.; Pogue, B. W.; Patterson, M. S.; Sevick-Muraca, E. M. Imaging of fluorescent yield and lifetime from multiply scattered light reemitted from random media. *Appl. Opt.* **1997**, *36*, 2260–2272.

Paulsen, K. D.; Jiang, H. Enhanced frequency-domain optical image reconstruction in tissue through total variation minimization. *Appl. Opt.* **1996**, *35*, 3447–3458.

Piston, D. W.; Marriott, G.; Gratton, E. Wide-band acousto-optic light modulator for frequency domain fluorometry and phosphorimetry. *Rev. Sci. Instrum.* **1989**, *62*, 1727–1734.

Pogue, B. W.; Patterson, M. S.; Jiang, H.; Paulsen, K. D. Initial assesment of a simple system for frequency domain diffuse otpical tomography. *Phys. Med. Biol.* **1995**, *40*, 1709–1729.

Reynolds, J. S.; Thompson, C. A.; Webb, K. J.; LaPlant, F. A.; Ben-Amotz, D. Frequency domain modeling of reradiation in highly scattering media. *Appl. Opt.* **1997**, *36*, 2252–2259.

Sevick, E.; Lakowicz, J.; Szmacinski, H.; Nowaczyk, K.; Johnson, M. Frequency domain imaging of absorbers obscured by scattering. *J. Photochem. Photobiol. B: Biol.* **1992**, *16*, 169–185.

Sevick-Muraca E. M.; Burch, C. L. Origin of phosphorescence signals reemitted from tissues. *Opt. Lett.* **1994**, *19*, 1928–1930.

Sevick-Muraca, E. M.; Hutchinson, C. L.; Paithankar, D. Y. Optical tissue biodiagnostics using fluorescence lifetime. *Opt. Photon News* **1996**, *5*, 25–28.

Sevick-Muraca, E.; Lopez, G.; Reynolds, J.; Troy, T.; Hutchinson, C. Fluorescence and absorption contrast mechanisms for biomedical optical imaging using frequency-domain techniques. *J. Photochem. Photobiol. B: Biol.* **1997**, *66*, 55–64.

Spencer, R. D. and Weber, G. Measurement of subnanosecond fluorescence lifetimes with a cross-correlation phase fluorometer. *Ann. N. Y. Acad. Sci.* **1969**, *158*, 361–376.

van Staveren, H. J.; Moes, C. J. M.; van Marie, J.; Prahl, S. A.; van Gement, M. J. C. Light scattering in Intralipid-10% in the wavelength range of 400–1100 nm. *Appl. Opt.* **1991**, *30*, 4507–4514.

Thompson, R. B.; Frisoli, J. K.; Lakowicz, J. R. Phase fluorometry using a continuously modulated laser didoe. *Anal. Chem.* **1992**, *64*, 2075–2078.

Troy, T. L.; Page, D.; Sevick-Muraca, Optical properties of normal and diseased breast tissues: prognosis for optical mammography. *J. Biomed. Opt.* **1996**, *1*, 342–355.

Troy, T. L.; Reynolds, J. S.; Sevick-Muraca, E. M. Photon migration imaging using multipixel measurements. *Proc. SPIE* **1997**, *2979*, 111–121.

Accepted August 5, 1997.⊗

BP970085G

⊗ Abstract published in *Advance ACS Abstracts,* September 15, 1997.

Multi-Pixel Frequency Domain Photon Migration Imaging of a Fluorescent Contrast Agent

J.S. Reynolds, T.L. Troy, D.J. Waters[†], K.K. Cornell[†] and E.M. Sevick-Muraca
School of Chemical Engineering and [†]School of Veterinary Medicine
Purdue University, West Lafayette, IN 47907 USA
http://photon.ecn.purdue.edu/~chepmi/ppml.html
Phone: (765) 496-2377, Fax: (765) 494-0805, email: sevick@ecn.purdue.edu

Abstract

An RF phase sensitive camera is used to acquire frequency domain photon migration images of the fluorescent contrast agent indocyanine green (ICG) in diseased canine mammary tissue both *in vivo* and *ex vivo*. Using this system, images of 100 MHz modulation amplitude and phase are obtained for 128 x 128 pixels.

I. INTRODUCTION

The success of frequency domain biomedical optical imaging depends upon the ability to measure changes in photon migration due to differences in the optical properties of normal and diseased tissues. In fact several investigators have successfully demonstrated reconstructed images based upon differences in absorption and scattering for idealized tissue phantoms [1,2]. However, the differences between normal and diseased tissue may not be consistently large enough for sufficient detection [3]. Consequently, we have embarked on studies to investigate exogenous contrast agents using multi-pixel frequency domain measurements. In this study we examine the fluorescence from ICG in diseased canine mammary tissue.

II. EXPERIMENTAL PROCEDURE

Experimental measurements are performed using the apparatus shown in Figure 1 [4]. The light source is a 30 mW, 789 nm laser diode (circular and collimated), driven above its lasing threshold by a constant current source and amplitude modulated by a 13 dBm RF signal supplied by a Marconi frequency synthesizer. For the images presented here, we use a 100 MHz modulation frequency. The RF modulated light is delivered to the tissue using a 1 mm optical fiber. The light is allowed to spread in its natural cone from the fiber to a diameter of 2.5 cm to provide more uniform illumination. The light propagates through the tissue in a transillumination geometry and is collected by the RF phase sensitive camera. The image intensifier of the phase sensitive camera is gain modulated at the same phase locked frequency as the laser diode. This produces a homodyne image of the phantom where the intensity is related to both the average intensity as well as the modulation amplitude and phase of the light emitted by the tissue. By taking a series of images with different intensifier phases relative to the diode modulation phase, the individual pixel average intensity, modulation amplitude, and modulation phase can be determined efficiently with a Fast Fourier Transform algorithm. This technique is described in more detail in Reference [4]. Images of emission light can be obtained by inserting an appropriate bandpass filter in front of the input to the image intensifier.

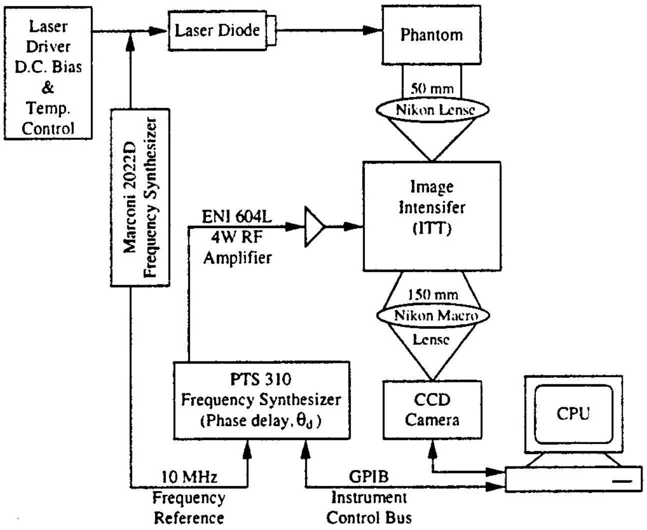
Laser Driver D.C. Bias & Temp. Control
Laser Diode
Phantom
50 mm Nikon Lense
Marconi 2022D Frequency Synthesizer
ENI 604L 4W RF Amplifier
Image Intensifer (ITT)
150 mm Nikon Macro Lense
PTS 310 Frequency Synthesizer (Phase delay, θ_d)
CCD Camera
CPU
10 MHz Frequency Reference
GPIB Instrument Control Bus

FIG. 1. Schematic of the multi-pixel frequency domain apparatus.

The canine subjects in this study are all adult, female pets that are about to undergo surgery to remove parts of their mammary chain because of palpable breast nodules. Many of these lumps are suspected to be naturally occurring breast cancer. Thus, this model affords an excellent opportunity to study the pharmacokinetics and *in vivo* optical properties of a fluorescent contrast agent in naturally occurring diseased mammary tissue.

The clinical procedure is as follows. The subject is prepared for surgery, which includes shaving the area around the mammary glands. The dog is anesthetized and moved into the surgical suite. While the surgical team monitors the dog's health, the RF phase sensitive camera is clamped to the area with suspect breast lumps. The imager is shown clamped to a canine breast in Figure 2. Measurements of excitation and emission fluence are made before and after injection of a clinical dose of

ICG. After acquiring the *in vivo* data, the imager is removed from the operating room and a mastectomy is performed. Further *ex vivo* images are then acquired on the freshly excised diseased tissue. The tissue is then frozen and sectioned for histology.

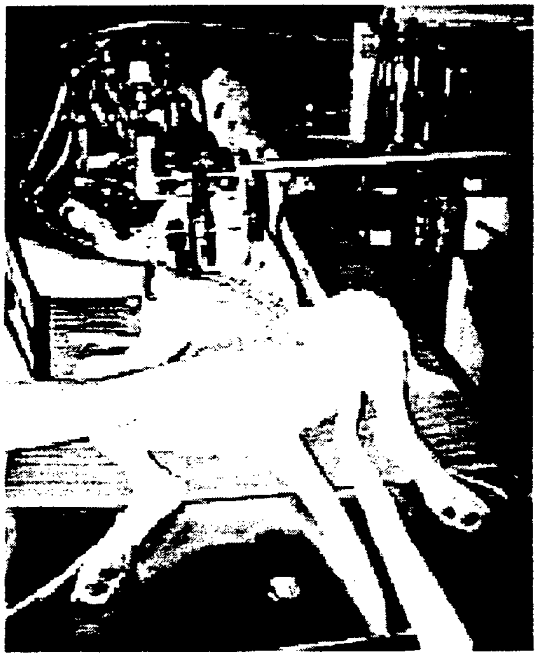

FIG. 2. Photograph of the apparatus used to clamp canine mammary tissue for transillumination measurements.

III. EXPERIMENTAL RESULTS

A representative set of fluorescent emission images of the right fifth (most posterior) mammary gland is shown in Figure 3. This subject is a 11 year old miniature poodle weighing 7.5 kg. The total exposure time for this 128 x 128 pixel modulation image is approximately 1 minute. This data was acquired approximately 25 minutes after systemic injection of a 1.6 cc 0.5% solution of pharmaceutical grade ICG in sterile saline solution. The source is centered at the lower edge of the frame on the opposite side of the tissue (transillumination geometry, thickness 1.9 cm). The upper edge of the clamped breast tissue is marked by the smooth transition from grey to black near 1.5 cm on the vertical axis. The raised tissue at 3 cm on the horizontal axis is caused by the suture which is used to support the tissue during clamping. The area of low phase around the suture in Figure 3c. is believed to result from the fluorescence of a small area of bleeding around the suture. The differences between the *in vivo* average (DC) intensity images, modulation amplitude images, and modulation phase images demonstrate that more information can be obtained with frequency domain measurements than with a simple measurement of average fluorescent intensity.

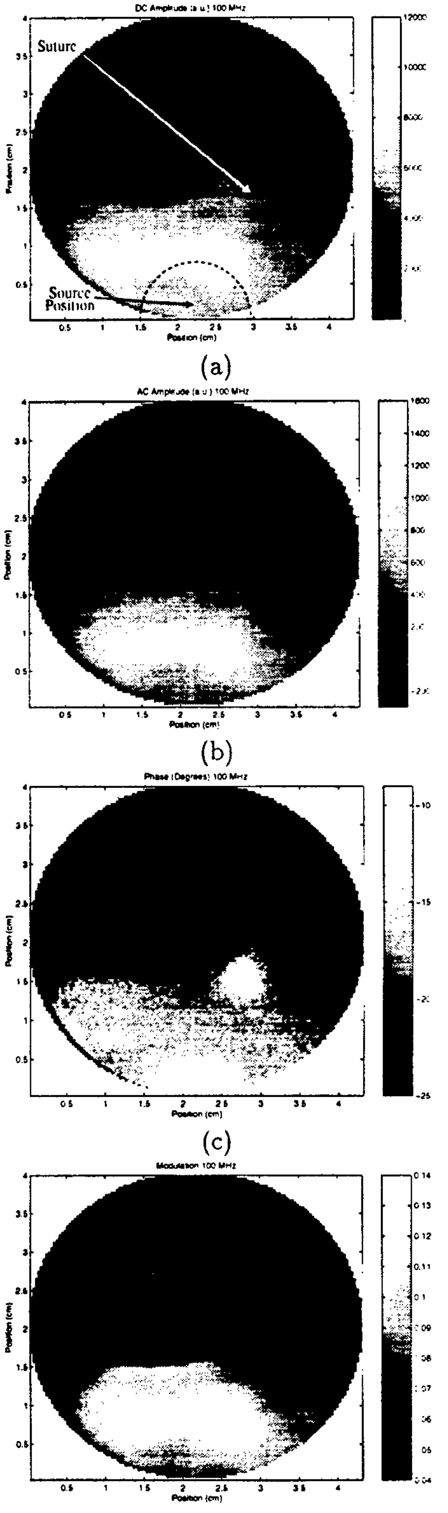
DC Amplitude (a.u.) 100 MHz
Suture
Source Position
Position (cm)
Position (cm)
12000
10000
8000
6000
4000
2000
(a)
AC Amplitude (a.u.) 100 MHz
1600
1400
1200
1000
800
600
400
200
(b)
Phase (Degrees) 100 MHz
-10
-15
-20
-25
(c)
Modulation 100 MHz
0.14
0.13
0.12
0.11
0.1
0.09
0.08
0.07
0.06
0.05
0.04
(d)
0.5
1
1.5
2
2.5
3
3.5
4

FIG. 3. *In vivo* image of the emission light from ICG at 830 nm from the right fifth mammary gland of a miniature poodle. The excitation light is 789 nm with 100 MHz modulation. a) is the average (DC) intensity, b) is the AC or modulation amplitude, c) is the modulation phase, and d) is the modulation ratio (AC/DC).

In order to quantify the spatial uptake of the dye in the breast tissue a series of average intensity images were taken at periodic intervals for several minutes after injection of the dye. The geometry and subject are identical to Figure 3. In Figure 4 we present a time histogram created by taking a horizontal slice through each of the time images at around 1 cm (through the area of high intensity). The data starts 3 minutes after injection and runs for 23 minutes. The fluorescent intensity can be clearly seen rising quickly to a peak at 5 minutes after injection and then dropping slowly thereafter as the dye washes out.

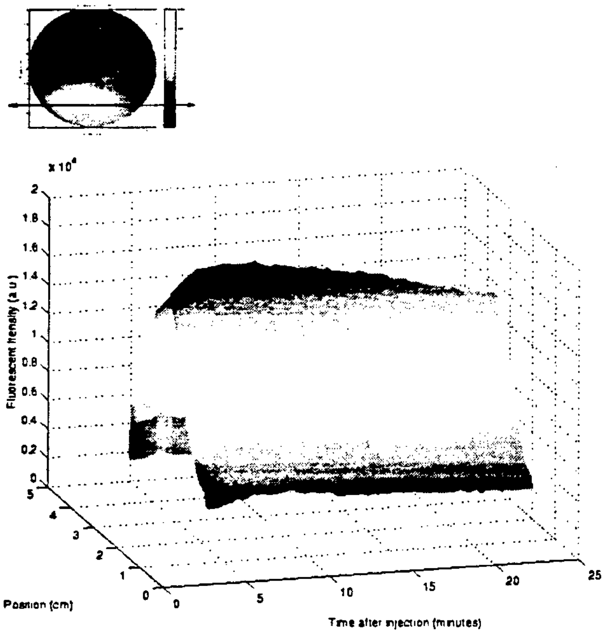

FIG. 4. Histogram showing uptake and wash out of ICG in a mammary gland *in vivo*. The sub figure in the upper left corner shows the physical location of the displayed slice.

A representative *ex vivo* frequency domain photon migration image is shown in Figure 5. The excised tissue is from the right fifth mammary gland of a 9 year old, female golden retriever weighing 38 kg. This image is taken from the skin side through 2 cm of tissue in a transillumination geometry with the source centered in the frame. A palpable lump is present in the center of this image. The shadow of the lump (approximately 1 cm in diameter) can be seen in the phase and modulation ratio images although it is not visible in the image of DC intensity. Once again this demonstrates the added information obtained using frequency domain photon migration imaging.

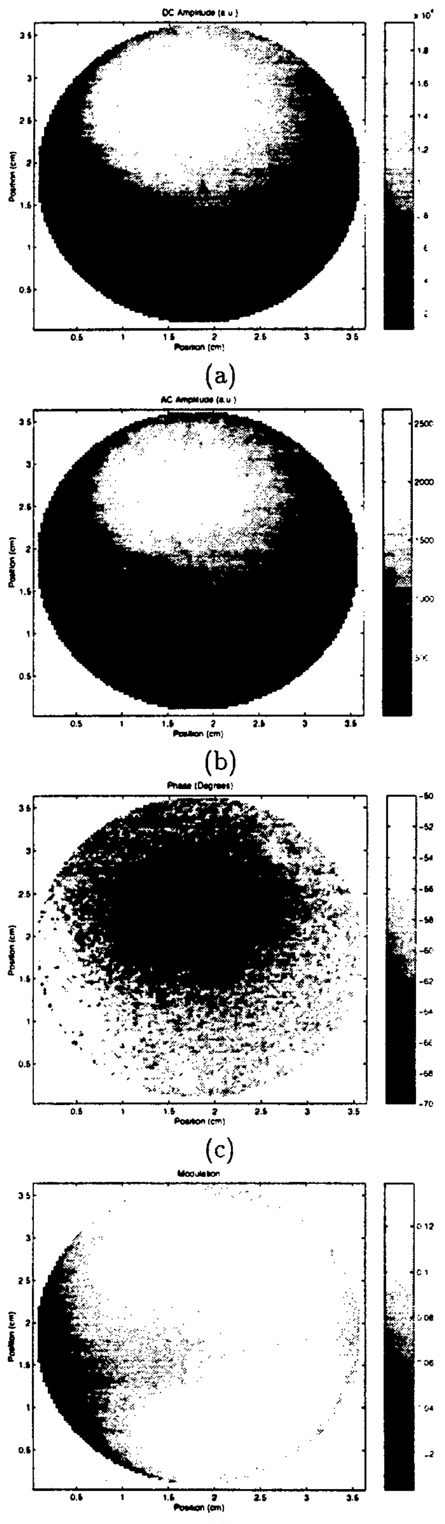
DC Amplitude (a.u.)
x 10⁴
Position (cm)
Position (cm)
(a)
AC Amplitude (a.u.)
2500
2000
1500
Position (cm)
Position (cm)
(b)
Phase (Degrees)
-50
-52
-54
-56
-58
-60
-62
-64
-66
-68
-70
Position (cm)
Position (cm)
(c)
Modulation
0.12
0.1
0.08
0.06
0.04
Position (cm)
Position (cm)
(d)

FIG. 5. *Ex vivo* image of the 789 nm excitation light from the right fifth mammary gland of a golden retriever with 100 MHz modulation. a) is the average (DC) intensity, b) is the AC or modulation amplitude, c) is the modulation phase, and d) is the modulation ratio (AC/DC).

Figure 6 shows a time histogram of vertical slices through the center of the data shown in Figure 5. The shadow from the tumor can be seen in the middle of the spatial axis. However, a definite shift in brightness from bottom to top can be seen as time progresses. We speculate that this shift in average intensity is due to blood drainage in the tissue which is clamped vertically for this measurement.

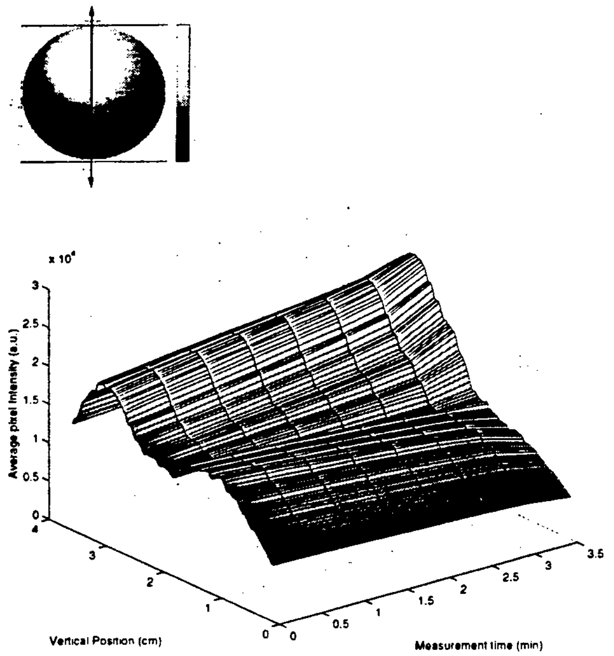

FIG. 6. Time histogram showing change in average intensity of an *ex vivo* tissue sample. The sub figure in the upper left corner shows the physical location of the displayed slice.

IV. CONCLUSION

Because of its ability to make rapid and highly sensitive measurements of frequency domain diffusing photon density waves, an RF phase sensitive camera is proving to be a useful tool for clinical measurements. In addition, both the *in vivo* and *ex vivo* frequency domain images demonstrate that there is important information present in the RF modulation envelope that is not present in the average intensity images. Continuous improvements are being made to the apparatus to increase sensitivity and image quality. Clinical images allow for the study of important contrast agent parameters such as pharmacokinetics, lifetime, and specificity. Also, improved clinical images can be used as inputs into reconstruction algorithms.

V. ACKNOWLEDGMENTS

The authors would like to acknowledge Amy Honkomp and the other members of the Purdue University Comparative Oncology Program. We would also like to thank Ralf Meyer, Jennifer Elmore, Alan Thompson and Brian Towne of the Purdue University Photon Migration Laboratory. This work was supported in part by the National Institutes of Health under grants R01CA61413, R0167176-01, and K04CA687374-01.

---

[1] M. O'Leary, D. Boas, B. Chance, and A. Yodh, "Experimental images of heterogeneous turbid media by frequency-domain diffusion-photon tomography," Optics Letters **20**, 426–428 (1995).

[2] B. W. Pogue, M. S. Patterson, H. Jiang, and K. D. Paulsen, "Initial assessment of a simple system for frequency domain diffuse optical tomography," Phys. Med. Biol. **40**, 1709–1729 (1995).

[3] T. L. Troy, D. Page, and E. M. Sevick-Muraca, "Optical properties of normal and diseased breast tissues: prognosis for optical mammography," J. Biomed. Opt. **1**, 342–355 (1996).

[4] J. S. Reynolds, T. Troy, and E. M. Sevick-Muraca, "Multipixel techniques for frequency-domain photon migration imaging," Biotechnology Progress **13**, 669–680 (1997).

Reconstruction of Fluorescent Lifetime and Quantum Efficiency Using Frequency Domain Photon Migration Measurements

T.L. Troy, J.S. Reynolds and E.M. Sevick-Muraca
The Photon Migration Laboratory
School of Chemical Engineering
Purdue University
West Lafayette, IN 47907-1283 USA
http://photon.ecn.purdue.edu/~chepmi/ppml.html
Phone: (765) 496-2377, Fax: (765) 494-0805, email: sevick@ecn.purdue.edu

Abstract

Using a finite difference approach to solve the coupled diffusion equations for the excitation and emission light, tomographic maps of absorption, fluorescence quantum efficiency, and lifetime were reconstructed from simulated detector measurements of diffuse photon density waves made at the periphery of a tissue phantom.

I. INTRODUCTION

With the development of near-infrared (NIR) laser diodes, the synthesis of fluorescent dyes with excitation and emission spectra in the NIR wavelength regime has accelerated in the past decade for microscopy applications. Owing to the window of low absorbance in tissues in this wavelength regime, an opportunity also exists for the deployment of fluorescent dyes as *in vivo* diagnostic agents.

The detection of disease via the use of fluorescent dyes and photodynamic drugs as contrast agents has been proposed by several investigators. However, a long-standing problem has been the low uptake into diseased tissues providing insufficient contrast for detection of disease. While targeted delivery may improve uptake ratios and contrast imparted by these agents, contrast agent targeting approaches have been rather elusive even in conventional imaging modalities such as magnetic resonance imaging and x-ray computed tomography. Investigators have sought to improve optical contrast independent of uptake ratio by employing dyes which fluoresce differently in diseased and normal tissues.

One difficulty, however, lies in using multiply scattered light detected at the air-tissue interface to reconstruct an image which differentiates internal tissues on the basis of uptake and fluorescent properties of quantum efficiency and lifetime. Frequency domain measurements of modulation phase and amplitude were conducted at the surface of simulated tissue phantoms in order to demonstrate the capacity for fluorescent quantum efficiency and lifetime imaging. The modulation phase and amplitude of the detected fluorescent wave relative to the incident excitation source provides information about fluorescent quantum efficiency and lifetime. However, due to the intense multiple scattering properties of tissues, contributions of excitation and fluorescent light propagation characteristics are also incorporated into the measurements.

Using a mathematical model of diffuse light propagation and fluorescence generation within random media, the presence and location of simulated diseased tissue heterogeneities within a tissue volume was detected. These computations suggest that multiple source and detection schemes need to be utilized for biomedical diagnostic imaging and spectroscopy of fluorescence quantum efficiency and lifetime. The method is similar to that used by Yorkey *et al.* [1] for electrical impedance tomography, Pogue *et al.* [2] for absorption and scattering reconstructions, and Paithankar *et al.* [3] who performed reconstructions on both fluorescent lifetime, τ, and fluorescent yield (the product of the absorption coefficient due to fluorophores and quantum efficiency, $\phi\mu_{a_{xf}}$). In addition to these types of reconstructions, fluorescent lifetime imaging has been performed using alternative approaches [4,5].

II. FORWARD PROBLEM

The forward problem generates simulated exterior detector data. This data is then used by the inversion algorithm to reconstruct optical property maps of the interior. The approach consists of a two dimensional, simulated tissue phantom with a 4 × 4 cm^2 surface (Figure 1). The phantom is discretized into either a 17 × 17 or a 33 × 33 grid. An optical heterogeneity is placed in the phantom and is either one pixel (for the 17 × 17 grid) or nine pixels (for the 33 × 33 grid) in size.

The source and the detector locations were placed one pixel in from the edge of the phantom to overcome the effects of the zero fluence boundary condition. A source is centered on each side of the phantom for a total of 4 sources. Our approach to the forward problem consists of solving the coupled diffusion equations using finite differences in order to obtain detector data at either 56 (17 × 17 grid) or 120 (33 × 33 grid) locations around the periphery of the phantom for each of the 4 sources.

To solve the forward problem, the optical properties of the background and the object are input as parameters into the program and then the fluence at each grid point is calculated using MUDPACK, a finite difference, multigrid software package [6]. The fluence values at the detector positions are then used to calculate the modulation phase, $\theta^{x,m}$, and the log of the modulation amplitude, $I_{AC}^{x,m}$ (superscripts x and m represents the excitation and emission light, respectively),

$$\theta^{x,m} = \tan^{-1}\left[\frac{Im\Phi^{x,m}}{Re\Phi^{x,m}}\right] \tag{2.1}$$

$$I_{AC}^{x,m} = \log_{10}\sqrt{[Im\Phi^{x,m}]^2 + [Re\Phi^{x,m}]^2}. \tag{2.2}$$

During the simulation, only one source is active at a time. A total of four simulated experiments constitute the data to be acquired experimentally. In all the simulated experiments, the sources are modulated at a frequency of 100 MHz. Typical forward calculations on a Ultra 2 Sun workstation take approximately 1.3 s.

After detector data is evaluated for $\theta^{x,m}$ and $I_{AC}^{x,m}$, simulated Gaussian noise with a standard deviation of 0.1° for phase and 1% for modulation amplitude is added using a MATLAB routine. The Gaussian noise is added to account for the noise which would be encountered in a real experiment. The simulated forward results with added noise are then input to the inversion algorithm.

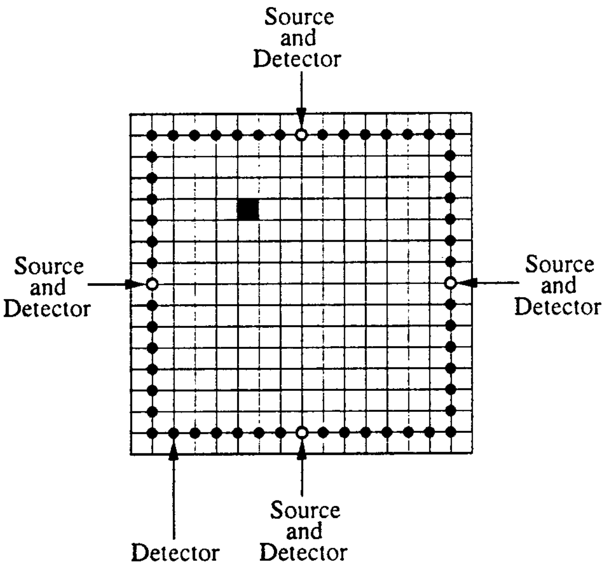
Source
and
Detector
Source
and
Detector
Source
and
Detector
Detector
Source
and
Detector

FIG. 1. Schematic of the two–dimensional simulated tissue phantom showing the location of the 4 sources and 56 detectors around the perimeter for a 17 × 17 grid of 16 cm^2 area. The small square object (one pixel in size) inside the phantom represents a simulated diseased tissue volume.

III. INVERSE PROBLEM

The solution to the inverse problem requires reconstructing images of the interior volume from exterior measurements of $\theta^{x,m}$ and $I_{AC}^{x,m}$. The inversion algorithm is conducted in two parts on the basis of (i) absorption at the excitation wavelength due to fluorophores, $\mu_{a_{xf}}$, and (ii) quantum efficiency, ϕ, or lifetime, τ, at the emission wavelength. The two parts are similar except the reconstruction based on $\mu_{a_{xf}}$ uses detector data at the excitation wavelength while the other part uses data at the emission wavelength.

Figure 2 shows the flow diagram for $\mu_{a_{xf}}$ inversions. First, a uniform guess for the optical property map is given. Typical values are those found in normal tissue. The forward solution is then calculated to obtain θ^x and I_{AC}^x detector data for the excitation light. Next, two Jacobian matrices, $\mathbf{J}(\theta^x, \mu_{a_{xf}})$ and $\mathbf{J}(I_{AC}^x, \mu_{a_{xf}})$, are constructed where each entry of the matrix is defined as $j_{ij} = \partial\theta_i^x / \partial\mu_{a_{xf},j}$ and $j_{ij} = \partial I_{AC_i}^x / \partial\mu_{a_{xf},j}$, respectively. Each element of the matrix describes the response of the source-detector pair at position i to changes in $\mu_{a_{xf}}$ at each pixel j. The partial derivatives are numerically approximated by calling the forward solution a second time

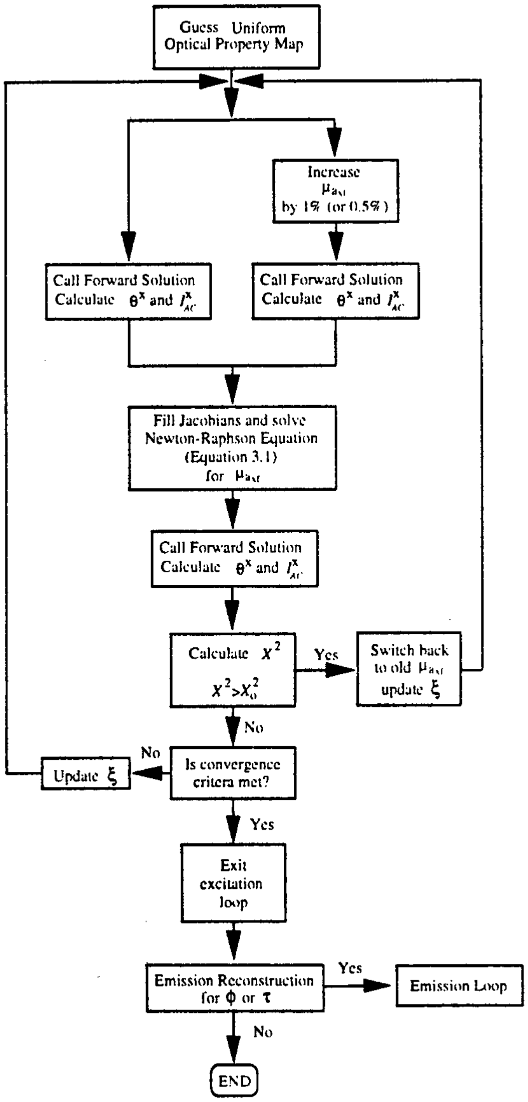
Guess Uniform
Optical Property Map
Increase
μaxf
by 1% (or 0.5%)
Call Forward Solution
Calculate θx and IxAC
Call Forward Solution
Calculate θx and IxAC
Fill Jacobians and solve
Newton-Raphson Equation
(Equation 3.1)
for μaxf
Call Forward Solution
Calculate θx and IxAC
Calculate χ2
χ2>χ2o
Yes
Switch back
to old μaxf
update ξ
No
No
Update ξ
Is convergence
critera met?
Yes
Exit
excitation
loop
Emission Reconstruction
for φ or τ
Yes
Emission Loop
No
END

FIG. 2. Flow diagram for $\mu_{a_{xf}}$ inversions based on photon migration measurements at the excitation wavelength.

for a 1% (17 × 17 grid) or a 0.5% (33 × 33 grid) increase in the original pixel value of $\mu_{a_{xf}}$ and subtracting the difference (i.e. $\partial\theta^x/\partial\mu_{a_{xf}} \approx \Delta\theta^x/\Delta\mu_{a_{xf}}$ and $\partial I^x_{AC}/\partial\mu_{a_{xf}} \approx \Delta I^x_{AC}/\Delta\mu_{a_{xf}}$).

The values of $\mu_{a_{xf}}$ are updated using an iterative Newton-Raphson technique,

$$\left[\frac{\mathbf{J}^T(\theta^x,\mu_{a_{xf}})\mathbf{J}(\theta^x,\mu_{a_{xf}})}{\sigma^2_\theta}+\frac{\mathbf{J}^T(I^x_{AC},\mu_{a_{xf}})\mathbf{J}(I^x_{AC},\mu_{a_{xf}})}{\sigma^2_{I_{ac}}}+\xi\mathbf{I}\right][\Delta\vec{\mu}]=$$

$$\left[\frac{\mathbf{J}^T(\theta^x,\mu_{a_{xf}})}{\sigma^2_\theta}\left(\vec{\theta}^x_{obs}-\vec{\theta}^x_{cal}\right)+\frac{\mathbf{J}^T(I^x_{AC},\mu_{a_{xf}})}{\sigma^2_{I_{AC}}}\left(\vec{I}^x_{AC_{obs}}-\vec{I}^x_{AC_{cal}}\right)\right] \quad (3.1)$$

where $\Delta\vec{\mu}_{a_{xf}}$ provides a small change for updating $\mu_{a_{xf}}$. The value ξ is a regularization parameter which is multiplied by the identity matrix, **I**. Because the Jacobian matrices are ill conditioned due to the small sensitivity of $\mu_{a_{xf}}$ far away from the source and detector, the regularization parameter compensates by making the matrices more diagonally dominant. The parameter ξ is then adjusted by a Marquardt-Levenberg algorithm at every iteration [2]. In order to solve the linear algebraic equations (Equation 3.1) for $\Delta\vec{\mu}_{a_{xf}}$, a LU decomposition back substitution method is used. The updated optical property map is then found by adding $\Delta\vec{\mu}_{a_{xf}}$ to the values from the previous iteration.

The forward solution is re-calculated using the new updated values in order to determine the reconstruction error,

$$\chi^2_x=\frac{1}{4n}\sum_{k=1}^{4}\sum_{i=1}^{n}\left[\left(\frac{\theta^x_{cal,i,k}-\theta^x_{obs,i,k}}{\sigma_\theta}\right)^2+\left(\frac{I^x_{AC_{cal,i,k}}-I^x_{AC_{obs,i,k}}}{\sigma_{I_{AC}}}\right)^2\right] \quad (3.2)$$

where k is the source number, n is the total number of detectors (56 for the 17 × 17 grid or 224 for the 33 × 33 grid), θ^x_{cal} and $I^x_{AC_{cal}}$ are the predicted detector data and θ^x_{obs} and $I^x_{AC_{obs}}$ are the simulated experimental detector data for the excitation light. The values of σ_θ and $\sigma_{I_{AC}}$ are the typical standard deviations of noise in the measurements and are taken to be 0.1° and 1%, respectively. Every node on the grid will yield an equation and the only known variables are at the detector positions. Since there are many more nodes than detectors, the inversion scheme is under-constrained and not guaranteed to converge on the actual optical property map.

The entire procedure of iteratively adjusting $\mu_{a_{xf}}$ to minimize the χ^2_x error continues until a predetermined convergence criterion is met or a maximum of 50 iterations is reached. The criterion is met if any of the following quantities: (i) the value of χ^2_x, (ii) the absolute change in χ^2_x, or (iii) the relative change in χ^2_x become lower than 1.0 ×10^{-5}. Typical times to complete the inverse solution are approximately 45 minutes for the 17 × 17 grid and approximately 4 hours on the 33 × 33 grid on a Ultra 2 Sun workstation.

If only a map of $\mu_{a_{xf}}$ is desired, the program stops. Otherwise, the map of $\mu_{a_{xf}}$ is used in order to compute a second map of either ϕ or τ from detector data at the emission wavelength (Figure 3). Currently, the computation for maps of ϕ and τ are conducted in two separate programs in order to evaluate their individual performances.

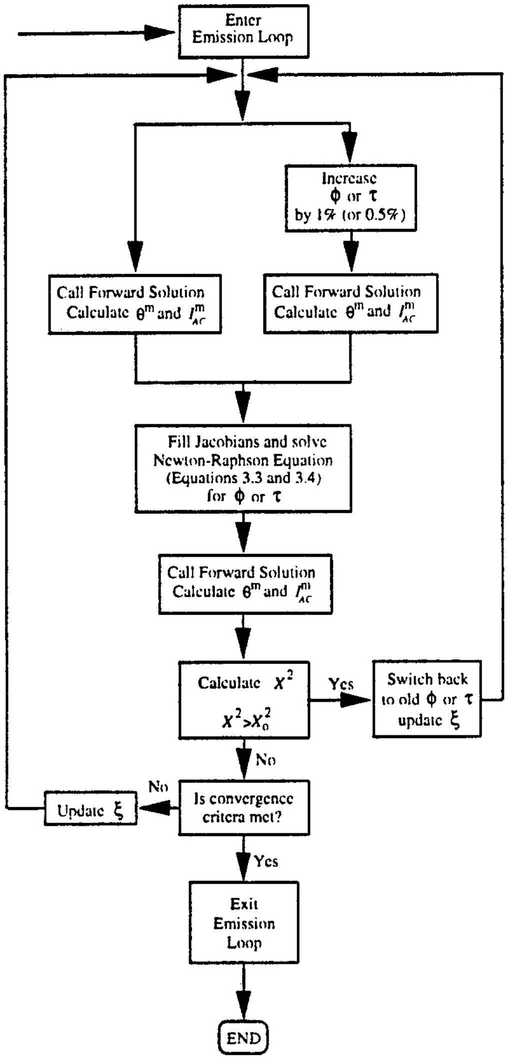
Enter Emission Loop
Increase Φ or τ by 1% (or 0.5%)
Call Forward Solution Calculate θ^m and I^m_AC
Call Forward Solution Calculate θ^m and I^m_AC
Fill Jacobians and solve Newton-Raphson Equation (Equations 3.3 and 3.4) for Φ or τ
Call Forward Solution Calculate θ^m and I^m_AC
Calculate χ² χ²>χ²₀
Yes
Switch back to old Φ or τ update ξ
No
No
Update ξ
Is convergence critera met?
Yes
Exit Emission Loop
END

FIG. 3. Flow diagram for ϕ or τ inversions based on photon migration measurements made at the emission wavelength.

The algorithm for the emission loop is similar to the one described above. First, the forward solution is calculated to obtain θ^m and I^m_{AC} measurements at the detector positions for the emission light using the homogeneous map described above except with the updated values of $\mu_{a_{xf}}$. Next, two Jacobian matrices are constructed: $\mathbf{J}(\theta^m,\phi)$ and $\mathbf{J}(I^m_{AC},\phi)$ for the reconstruction of ϕ, or $\mathbf{J}(\theta^m,\tau)$ and $\mathbf{J}(I^m_{AC},\tau)$ for reconstruction of τ. Each element of these Jacobian matrices is defined as $j_{ij} = \partial\theta^m_i/\partial\phi_j$, $j_{ij} = \partial I^m_{AC_i}/\partial\phi_j$, $j_{ij} = \partial\theta^m_i/\partial\tau_j$, and $j_{ij} = \partial I^m_{AC_i}/\partial\tau_j$, respectively. Again, each element of the Jacobian matrix describes the response of the source-detector pair at position i to changes in ϕ or τ at each pixel j. The partial derivatives are approximated as described above where $\partial\theta^m/\partial\phi \approx \Delta\theta^m/\Delta\phi$, $\partial I^m_{AC}/\partial\phi \approx \Delta I^m_{AC}/\Delta\phi$, $\partial\theta^m/\partial\tau \approx \Delta\theta^m/\Delta\tau$, and $\partial I^m_{AC}/\partial\tau \approx \Delta I^m_{AC}/\Delta\tau$.

Equations 3.3 and 3.4 provide updates of ϕ and τ by adding $\Delta\vec{\phi}$ and $\Delta\vec{\tau}$, respectively, to the values of ϕ and τ from the previous iteration,

$$\left[\frac{\mathbf{J}^T(\theta^m,\phi)\mathbf{J}(\theta^m,\phi)}{\sigma_\theta^2}+\frac{\mathbf{J}^T(I^m_{AC},\phi)\mathbf{J}(I^m_{AC},\phi)}{\sigma^2_{I_{AC}}}+\xi\mathbf{I}\right]\left[\Delta\vec{\phi}\right]=$$
$$\left[\frac{\mathbf{J}^T(\theta^m,\phi)}{\sigma_\theta^2}\left(\vec{\theta}^m_{obs}-\vec{\theta}^m_{cal}\right)+\frac{\mathbf{J}^T(I^m_{AC},\phi)}{\sigma^2_{I_{AC}}}\left(\vec{I}^m_{AC_{obs}}-\vec{I}^m_{AC_{cal}}\right)\right] \quad (3.3)$$

and

$$\left[\frac{\mathbf{J}^T(\theta^m,\tau)\mathbf{J}(\theta^m,\tau)}{\sigma_\theta^2}+\frac{\mathbf{J}^T(I^m_{AC},\tau)\mathbf{J}(I^m_{AC},\tau)}{\sigma^2_{I_{AC}}}+\xi\mathbf{I}\right]\left[\Delta\vec{\tau}\right]=$$
$$\left[\frac{\mathbf{J}^T(\theta^m,\tau)}{\sigma_\theta^2}\left(\vec{\theta}^m_{obs}-\vec{\theta}^m_{cal}\right)+\frac{\mathbf{J}^T(I^m_{AC},\tau)}{\sigma^2_{I_{AC}}}\left(\vec{I}^m_{AC_{obs}}-\vec{I}^m_{AC_{cal}}\right)\right]. \quad (3.4)$$

Again, the forward solution is re-calculated using the updated values in order to determine the reconstruction error,

$$\lambda_m^2=\frac{1}{4n}\sum_{k=1}^{4}\sum_{i=1}^{n}\left[\left(\frac{\theta^m_{cal,i,k}-\theta^m_{obs,i,k}}{\sigma_\theta}\right)^2+\left(\frac{I^m_{AC_{cal,i,k}}-I^m_{AC_{obs,i,k}}}{\sigma_{I_{AC}}}\right)^2\right] \quad (3.5)$$

where θ^m_{cal}, $I^m_{AC_{cal}}$ are the predicted detector data and θ^m_{obs} and $I^m_{AC_{obs}}$ are the simulated experimental detector data for the emission light. The values for σ_θ and $\sigma_{I_{AC}}$ are the same as in the absorption reconstruction, 0.1° and 1.0%, respectively. The entire procedure of iteratively adjusting ϕ or τ to minimize the χ^2_m error continues until the same convergence criterion as above is met or 50 iterations have passed.

Three different types of simulations were separately performed. They included reconstructions on the basis of absorption, $\mu_{a_{xf}}$, quantum efficiency, ϕ or lifetime, τ. In all three classes of simulated experiments, an optical heterogeneity on the 17 × 17 grid was 0.063 cm^2 which constituted 0.39% of the total area. For the 33 × 33 grid, the heterogeneity was 0.141 cm^2 or 0.88% of the total area. During the reconstructions of both ϕ and τ unphysically high optical property values around the periphery and especially near the source locations were obtained. These values were replaced with the average background value with a constraint statement inside the program.

For all the reconstructions, values of $\mu_{a_{xf}}$ range from 0.010 to 0.200 cm^{-1}. These values of absorption correspond to an ICG concentration of approximately 0.076 to 1.53 μM [7]. These ICG concentrations are well below lethal levels and are approximately 5 to 60 times lower than the therapeutic concentrations currently administered with many photodynamic agents [8,9]. The value for the isotropic scattering coefficient, μ'_s, was taken to be 10 cm^{-1} inside the object and the background.

IV. RECONSTRUCTION OF THE ABSORPTION COEFFICIENT FROM EXCITATION LIGHT

Figure 4 show a reconstruction based on a 10:1 difference in $\mu_{a_{xf}}$ between the object and its surroundings using the 17 × 17 grid. As described above, this ratio is the current performance observed with contrast agents. The values of $\mu_{a_{xf}}$ in the object and background were taken to be 0.200 cm^{-1} and 0.020 cm^{-1}, respectively. Figure 4 shows the (a) ideal spatial map, and (b) reconstructed image. Although the actual object location is at pixel (11,7), the largest value in the reconstruction, 0.042 cm^{-1}, was found at pixel (12,7) which is one pixel closer to the detectors in the y-direction. The reconstruction of $\mu_{a_{xf}}$ at location (11,7) was 0.035 cm^{-1} which is only 17% lower than the pixel (12,7) but 75% larger than the average background value. Because the program preserves the average pixel value, a smoothing of the reconstructed

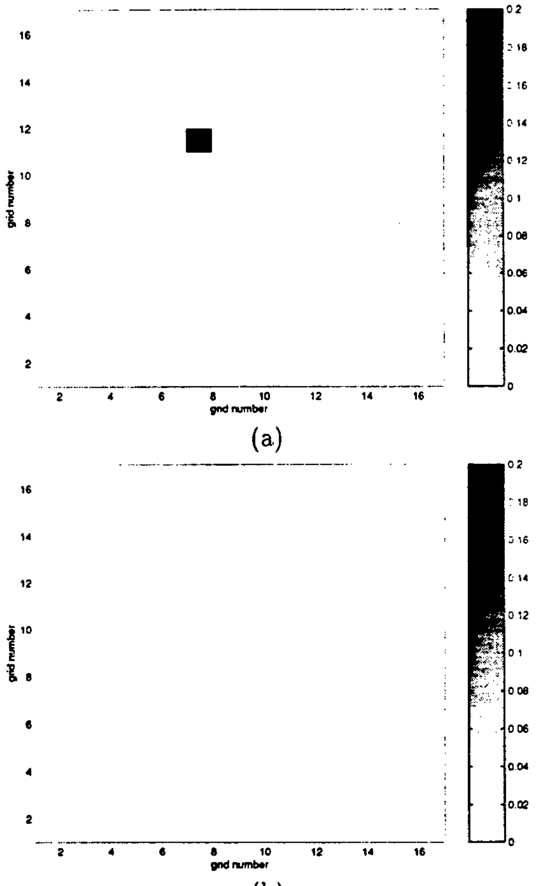

(a)

(b)

FIG. 4. Reconstructed spatial map for a 10:1 uptake ratio for an absorbing heterogeneity on a 17 × 17 grid. Figure (a) represents the actual spatial map, and (b) represents the reconstructed image. The actual values of $\mu_{a_{xf}}$ in the object and the surroundings were 0.200 cm^{-1} and 0.020 cm^{-1}, respectively, and the reconstruction yielded values of 0.035 cm^{-1} and 0.020 cm^{-1}, respectively.

image is observed causing the magnitude of $\mu_{a_{xf}}$ for both the object and the surroundings to be incorrect.

Next, the performance of a 10:1 uptake ratio for a reconstruction using a 33 × 33 grid was investigated (Figure 5). A more refined grid will yield smaller discretization errors because the derivatives are better approximated. However, the inversion problem is under-constrained, as discussed above, and is not guaranteed to converge on a unique solution. Therefore, a more refined grid might not yield better reconstructions since the number of nodes (equations to be solved) increases quadratically while the number of detectors (known variables) only increases linearly.

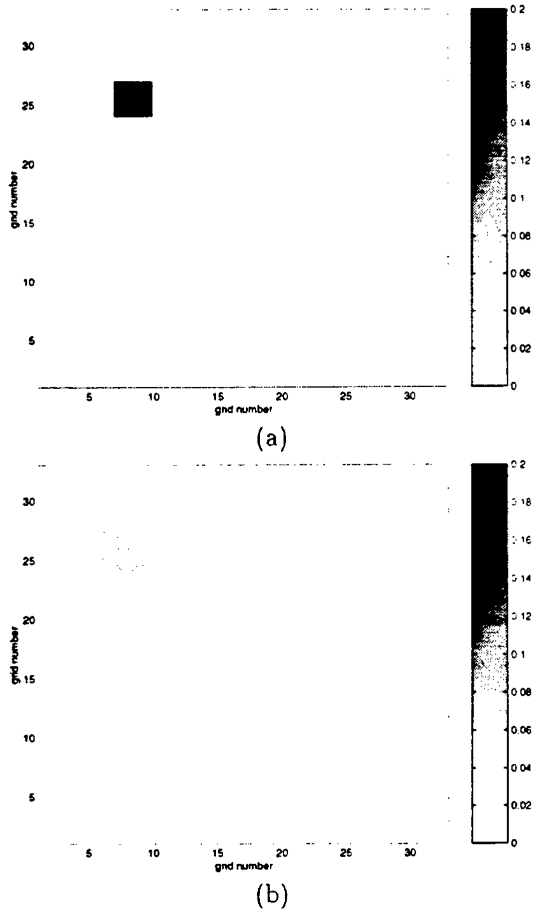

(a)

(b)

FIG. 5. Reconstructed spatial map for an absorbing heterogeneity on a 33 × 33 grid. Figure (a) represents the actual image, and (b) represents the reconstructed image. The actual values of $\mu_{a_{xf}}$ in the object and the surroundings were 0.200 cm^{-1} and 0.020 cm^{-1}, respectively, and the reconstructions yielded values of 0.084 cm^{-1} and 0.021 cm^{-1}, respectively.

The same optical parameters and reconstruction constraints as with the 17 × 17 grid (Figure 4) were maintained. Figure 5 shows (a) the actual spatial map and (b) the reconstructed image. This time the reconstruction correctly locates the object since the largest pixel value of 0.084 cm^{-1} is found at pixel (25,8). Although, the magnitude for $\mu_{a_{xf}}$ in both the object and the surroundings is incorrect due to the smoothing effect, an improvement over the 17 × 17 grid is seen. This reconstruction also converges after only 3 iterations which is faster than the 17 × 17 reconstruction which took 8 iterations.

V. RECONSTRUCTION OF QUANTUM EFFICIENCY FROM EMISSION LIGHT

The performance of the inverse algorithm for reconstructing maps of quantum efficiency, ϕ, using detector data at the emission wavelength is discussed in this section. For all the inversions discussed here, the exact value of $\mu_{a_{xf}}$ inside the object was input into the initial homogeneous guess. This procedure causes the inversion algorithm to converge after one iteration in the excitation loop and the exact value of $\mu_{a_{xf}}$ to be used in the emission loop in order to only investigate the reconstruction on ϕ. Also, the known value of τ both inside the object and background were input as part of the initial guess.

Figure 6 shows the (a) actual solution, and (b) reconstructed image using a 17 × 17 grid. The values of ϕ inside the object and surroundings were 0.10 and 0.010, respectively. Also, the values of $\mu_{a_{xf}}$ in the object and surroundings were 0.200 cm^{-1} and 0.020 cm^{-1}, respectively. The experiment ended after 50 iterations without meeting any of the convergence criteria. The optical property map of the reconstruction shows that the location of the object is successfully located but the value of ϕ inside the object only reaches 0.082 (18% smaller than the actual value). Also, the background pixel values are noisy with an average value of 0.012 which is 20% larger than the actual value.

Next, a 10:1 uptake of dye was investigated using the finer grid which is illustrated in Figure 7. The same optical parameters as before were used. The results for the reconstruction are inconclusive since the optical property map was too noisy to obtain any useful information. The reconstruction yielded an average pixel value of 0.051 for ϕ over the entire map which is approximately 400% larger than the actual background value. To perform a reconstruction of this kind on a 33 × 33 grid more data is necessary, either using more detectors or more frequency information.

VI. RECONSTRUCTION OF LIFETIME FROM EMISSION LIGHT

The performance of the inversion algorithm for reconstructing lifetime, τ, using detector data at the emission wavelength is discussed in this section. Similar to the reconstructions of ϕ, all the inversions in this section use the exact value of $\mu_{a_{xf}}$ inside both the object and background for the initial optical property map.

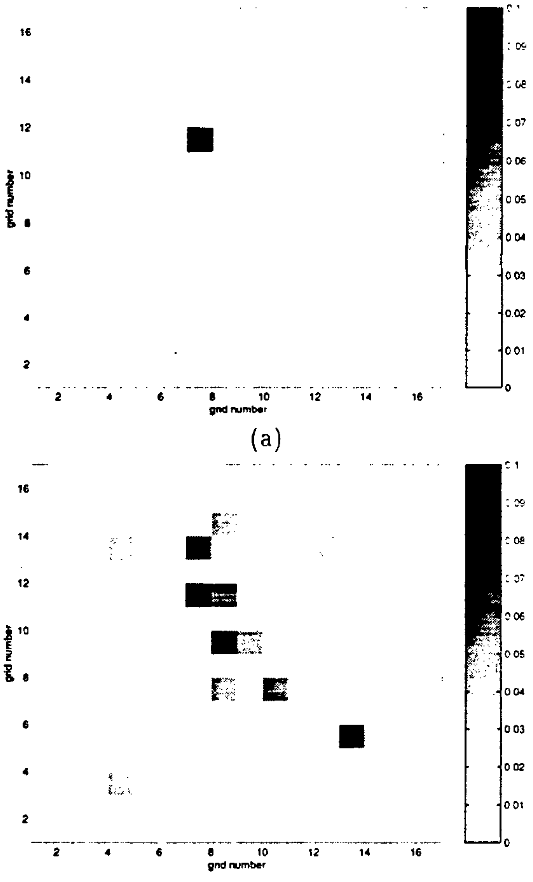

(a)

(b)

FIG. 6. Reconstructed spatial map of fluorescent quantum efficiency, ϕ, on a 17 × 17 grid for a 10:1 uptake of dye inside the heterogeneity. Figure (a) represents the actual image, and (b) shows the corresponding reconstruction. The actual values of ϕ in the object and the surroundings were 0.100 and 0.010, respectively. and the reconstructions yielded values of 0.082 cm and 0.012 cm^{-1}, respectively.

The lifetime reconstruction for a 10:1 uptake of dye, was investigated on both a 17 × 17 and 33 × 33 grid. For all τ reconstructions, τ had an arbitrary lifetime of 1.00 ns inside the object and a 10.0 ns everywhere else. As with ϕ reconstructions, the values of $\mu_{a_{xf}}$ in the object and surroundings were 0.200 cm^{-1} and 0.020 cm^{-1}, respectively. The first set of images is for the course grid. Figure 8 shows the (a) actual spatial map and the (b) reconstructed spatial map of τ. Because τ inside the object was lower than in the background, the object location is defined as the pixel with the lowest value of τ. Both the location and magnitude of τ inside the object are correctly found since the reconstructed value for pixel (11,7) is 0.996 ns, only 0.04% lower than the actual value. The reconstruction for the background converges to 10.1 ns even though the background contains a small amount of noise which is symmetric about the object. This noise is most likely an artifact from the large fluence that emerges from the four source locations.

The next set of reconstructions were identical to the last except that a finer grid, 33 × 33, was used. Figure 9 shows the (a) actual image along with the (b) corresponding reconstruction for τ. The algorithm does not correctly reconstruct the heterogeneity but a disturbance in the upper left quadrant where the object is located is obtained. The smallest pixel value of 1.00 × 10^{-5} ns is found at grid number (26,8) which is one pixel location above the actual object location. Unlike the absorption case, the refined grid does not yield better results, in fact, this result suggests that the algorithm based on lifetime cannot be used to detect the exact location of a heterogeneity containing a 10:1 uptake of dye using a 33 × 33 grid unless more information is given.

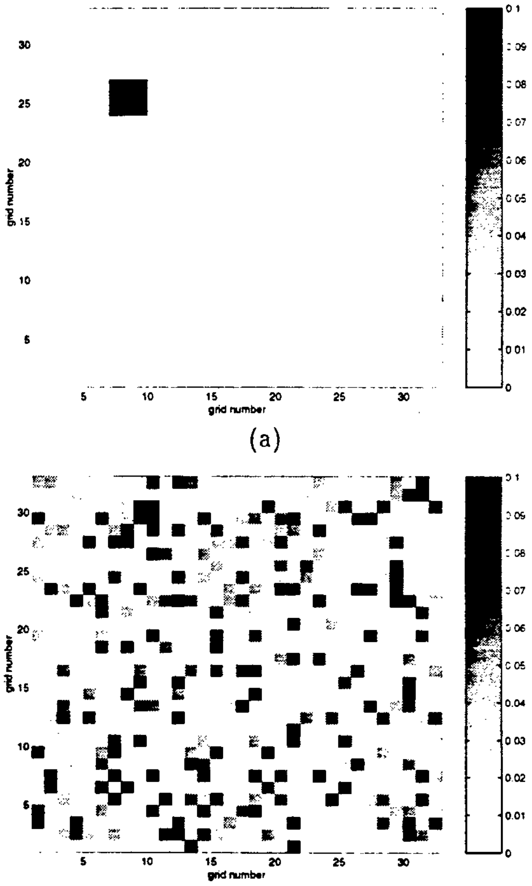

(a)

(b)

FIG. 7. Reconstructed spatial map of fluorescent quantum efficiency, ϕ, on a 33 × 33 grid for a 10:1 uptake of dye inside the heterogeneity. Figure (a) shows the actual image and (b) is the corresponding reconstruction. The actual value of ϕ in the object and background was 0.100 and 0.010, respectively. The algorithm was unable to reconstruct the object. The average quantum efficiency over the entire map for the reconstruction was 0.053.

The final reconstruction was for a 100:1 uptake of dye inside the object using the finer grid. The values of τ inside the object and the backgound were kept the same as above. Also, the values of $\mu_{a_{xf}}$ in the object was kept the same, 0.200 cm^{-1}. This time however, the value of $\mu_{a_{xf}}$ for the the surroundings was set to 0.002 cm^{-1}. Figure 10 shows (a) the actual image, and (b) the reconstruction. The smallest value of τ, 0.98 ns, was found at pixel location (25,8). This pixel along with its eight surrounding neighbors have an average value of 1.01 ns which is 1.0% larger than the true value. Therefore, at 100:1 uptake, both the magnitude and the location of the object are correctly obtained. The same kind of symmetric noise about the object that was observed in the 10:1 reconstruction on the 17 × 17 grid (Figure 8) is observed. Again, the noise seems to be a artifact of the source locations.

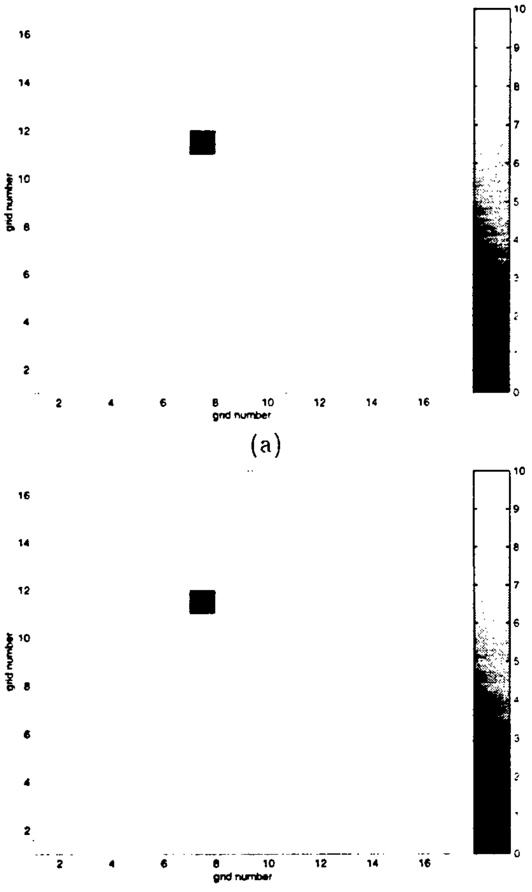

(a)

(b)

FIG. 8. Reconstructed spatial map of fluorescent lifetime, τ, on a 17 × 17 grid for a 10:1 uptake of dye inside the heterogeneity. Figure (a) shows the actual image and (b) is the corresponding reconstruction. The actual lifetimes for the object and background are 1.0 and 10.0 ns, respectively. The reconstruction converges correctly to 1.0 ns in the object. The background converges to 10.067 ns which is 0.67% larger than the actual value of 10 ns.

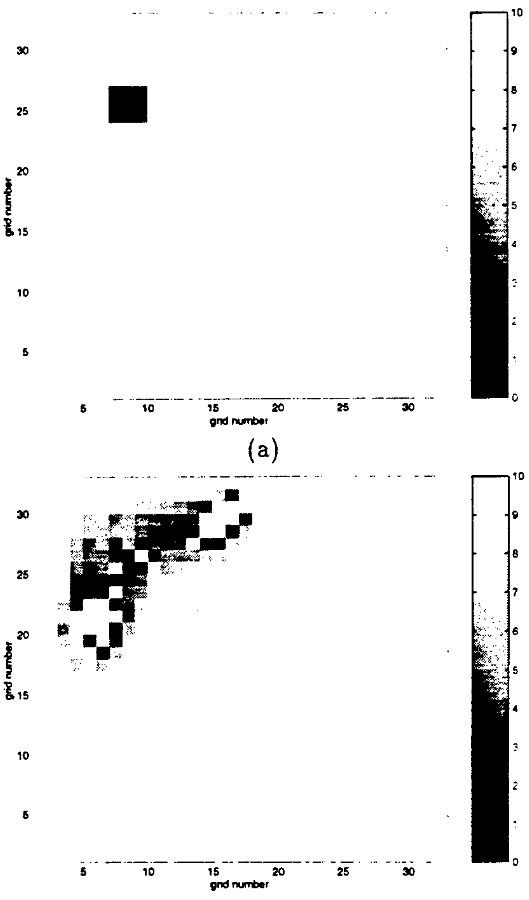

(a)

(b)

FIG. 9. Reconstructed spatial map of fluorescent lifetime, τ, on a 33 × 33 grid for a 10:1 uptake of dye inside the heterogeneity. Figure (a) represents the actual image and (b) is the corresponding reconstruction.

VII. CONCLUSIONS

Numerical simulations were conducted in order to examine the resolution and accuracy of our reconstruction method. These results show the potential of photon migration for the optical detection of a heterogeneity inside a scattering medium. The simulated experiments based on $\mu_{a_{xf}}$ can locate an absorbing heterogeneity inside a tissue simulating phantom, however the magnitude of $\mu_{a_{xf}}$ inside the heterogeneity is smaller than the actual solution. The simulated experiments also show the ability to reconstruct the interior optical property maps for both quantum efficiency and lifetime using detector information at the emission wavelength. Reconstructing maps of lifetime not only provides object location but also may provide information regarding the biochemical environment. This information about the local environment can help to differentiate normal from diseased tissue. Since targeted delivery of a contrast agent may not always be feasible, lifetime sensitive dyes which are specific to different environmental conditions found in normal and diseased tissue may enhance detection.

The noise for the fluorescent measurements needs to be determined since it is unlikely to be the same as the excitation data (0.1° for θ^{x} and 1% for I_{AC}^{x}). Also, both inversions assume that the noise is uniform over the entire region which may not be the actual situation, and updates to the inversion scheme, which take the noise as a function of position into account, need to be implemented.

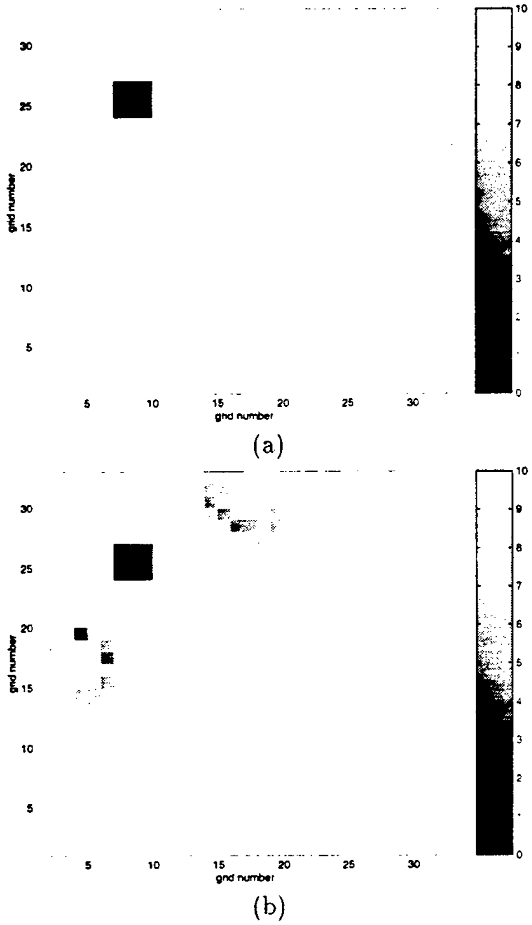

(a)

(b)

FIG. 10. Reconstructed spatial map of fluorescent lifetime, τ, on a 33 × 33 grid for a 100:1 uptake of dye inside the heterogeneity. Figure (a) represents the actual image and (b) is the corresponding reconstruction. The reconstructed background has an average value of 11.1 ns which is 11.1% from the true value of 10 ns. The reconstructed lifetime inside the object converged to an average value of 1.01 ns which is 1.0% from the true value of 1.00 ns.

To further improve the reconstructions, detector information at multiple modulation frequencies needs to be incorporated into the algorithm. Multiple frequency information will provide more detector information helping with the under-constrained nature of the inversion problem. Another way to improve the inversion is to solve the forward problem on a grid with a higher resolution than the optical property grid. This methodology will increase the number equations while keeping the number of unknowns constant thus making the inversion better constrained.

ACKNOWLEDGMENTS

This work was supported in part by the National Institutes of Health (R01CA61413, R0167176-01 and K04CA687374-01).

[1] T. J. Yorkey, J. G. Webster, and W. J. Tompkins, "Comparing reconstruction algorithms for electrical impedance tomography," IEEE Trans. Biomed. Eng. **BME-34**, 843-852 (1987).

[2] B. W. Pogue, M. S. Patterson, H. Jiang, and K. D. Paulsen, "Initial assessment of a simple system for frequency domain diffuse optical tomography," Phys. Med. Biol. **40**, 1709-1729 (1995).

[3] D. Y. Paithankar, A. U. Chen, B. W. Pogue, M. S. Patterson, and E. M. Sevick-Muraca, "Imaging of fluorescent yield and lifetime from multiply scattered light reemitted from random media," Appl. Opt. **36**, 2260-2272 (1997).

[4] M. O'Leary, D. Boas, D. Li, B. Chance, and A. Yodh, "Fluorescent lifetime imaging in turbid media," Optics Letters **21**, 158-160 (1996).

[5] J. Chang, H. Graber, and R. Barbour, "Luminescence Optical Tomography in Dense Scattering Media," JOSA A. 14 (1997).

[6] J. C. Adams, "MUDPACK: Multigrid portable FORTRAN software for the efficient solution of linear elliptic partial differential equations," Appl. Math. Comput. **34**, 113-146 (1989).

[7] E. Sevick-Muraca, G. Lopez, J. Reynolds, T. Troy, and C. Hutchinson, "Fluorescence and absorption contrast mechanisms for biomedical optical imaging using frequency-domain techniques," J. Photochem. Photobiol. **66**, 55-64 (1997).

[8] *Photodynamic Therapy basic principles and clinical application*, B. W. Henderson and T. J. Dougherty, eds., (Marcel Dekker, Inc., 1992).

[9] S. L. Marcus, "Photodynamic Therapy of Human Cancer," IEEE **80**, 869-889 (1992).

Fluorescence Lifetime Imaging and Spectroscopy in Random Media

Tamara L. Troy and Eva M. Sevick-Muraca

The Photon Migration Laboratory
School of Chemical Engineering
Purdue University
West Lafayette, IN 47907-1283 USA

http://photon.ecn.purdue.edu/~chepmi/ppml.html

submitted for publication in
Applied Fluorescence in Chemistry, Biology and Medicine

TABLE OF CONTENTS

Page

1. PART I -PRINCIPLES OF PHOTON MIGRATION 5

    1.1 Time and Frequency Domain Photon Migration 5
    1.2 Transport Property: Absorption Coefficient 6
    1.3 Transport Property: Scattering Coefficient 7
    1.4 Transport Property: Anisotropy Coefficient 7
    1.5 Governing Equations Describing the Transport of Light 8
        1.5.1 One-Speed Approximation to the Transport Equation 9
        1.5.2 Diffusion Equation Describing Light Propagation in Tissues . 9
        1.5.3 Source Location and Boundary Conditions 10
    1.6 Non-Radiative Mechanisms for Exogenous Contrast 10
        1.6.1 Contrast Owing to Absorption 11
        1.6.2 Contrast Owing to Dye with Fluorescent Characteristics . . . 12
        1.6.3 Diffusion Equations Describing Excitation and Emission Photon Migration 16
        1.6.4 Potential Fluorescent Contrast Agents for Photon Migration Imaging 17

2. PART II–CONTRAST FOR PHOTON MIGRATION IMAGING: FLUORESCENCE LIFETIME 19

    2.1 Single Pixel Measurements for Photon Migration Imaging 19
    2.2 Phantom Apparatus 19
    2.3 Frequency Domain Instrumentation and Set-Up 20
        2.3.1 Heterodyne Detection Approach with Modulated Laser Source 20
        2.3.2 Heterodyne Detection Approach with Pulsed Laser Source . . 21
        2.3.3 Instrumentation 21
    2.4 Contrast Owing to Perfect Absorption and Perfect Uptake of Fluorescence 22
    2.5 Contrast Owing to the Influence of Lifetime 24
    2.6 Discussion 24

3. PART III–RECONSTRUCTION OF FLUORESCENCE QUANTUM EFFICIENCY AND LIFETIME 26

Page
3.1 INVERSE IMAGING PROBLEM 26
  3.1.1 Forward Problem 27
  3.1.2 Solution to the Inverse Problem 29

4. PART IV–RECONSTRUCTION OF ABSORPTION AND FLUORESCENCE QUANTUM EFFICIENCY AND LIFETIME IN A SCATTERING MEDIUM 33

4.1 Results for the Reconstruction Algorithm 33
4.2 Reconstruction of the Absorption Coefficient from Excitation Light . 33
4.3 Reconstruction of Quantum Efficiency from Emission Light 34
4.4 Reconstruction of Lifetime from Emission Light 35
4.5 Discussion 36
4.6 Conclusion 37

LIST OF REFERENCES 51

With the development of near-infrared (NIR) laser diodes, the synthesis of fluorescent dyes with excitation and emission spectra in the NIR wavelength regime has accelerated in the past decade for microscopy applications. Owing to the window of low absorbance in tissues in this wavelength regime, an opportunity also exists for the deployment of fluorescent dyes as *in vivo* diagnostic agents. Figure 1.1 illustrates the typical absorbance spectra of tissues showing that at wavelengths less than 650 nm, hemoglobin absorbance provides the predominant attenuation of light in tissues, and above 900 nm water absorbance provides the predominant attenuation of light in tissues. In the "therapeutic window" of 650–900 nm, a window of low absorption exists in which light will be preferentially scattered over being absorbed. Consequently, it is possible to transmit multiply scattered NIR light across several centimeters of tissue. In addition, it is possible to excite NIR fluorophores deep within tissues and to collect the fluorescence re-emitted from the air-tissue interface. Since fluorescence provides a sensitive means for assessing local biochemistry via changes in quantum efficiency and lifetime, the ability to diagnose tissues based on spectroscopic evaluation of lifetime and quantum efficiency of exogenous diagnostic agents is possible. Agents whose emission characteristics vary with tissue pH [1, 2] and pO_2 [3] have been employed to detect diseased tissues by the nature of differing fluorescent properties as well as to provide diagnostic information regarding the diseased tissue volume. While typical contrast agents employed for the detection of diseased tissues depend on and are limited by the poor preferential uptake, the alteration of fluorescent properties provides a unique mechanism for inducing additional contrast [4]. For example, using time–gating to collect the long-lived fluorescence from hematoporphyrin derivative (HpD), Cubbeddu and coworkers [5, 6] were able to differentiate normal tissues from intradermally or subcutaneously implanted murine tumors in mice. More recently, it has been reported that the fluorescent decay of HpD is appreciably slower in experimental mice tumors than in their surrounding normal healthy tissues. Consequently, the use of a fluorescent dye may provide contrast owing to changes in fluorescent properties within tissue compartments.

The difficulty, however, lies in understanding the use of multiply scattered excitation light to excite a fluorophore in the tissue, and secondly, to extract information of lifetime and quantum efficiency from the multiply scattered fluorescence detected at the air–tissue interface. If the optical properties of the tissue are spatially uniform and the fluorescent dye has constant fluorescent properties, then the problem is one of *fluorescent lifetime spectroscopy* in tissues. However, if the detection of diseased tissues is to be tackled, the problem becomes one of *fluorescent lifetime spectroscopic imaging*, since optical properties and fluorescent properties of diagnostic agents may vary with spatial location.

In this chapter, frequency domain photon migration fluorescence imaging is described as a method for generating an optical map or image of fluorescent lifetime and quantum efficiency from exterior measurements of modulation phase and modulation amplitude on tissues or highly scattering media. In Part I, the theory behind the propagation of excitation light and generation of fluorescent light within scattering media such as tissues is presented. Part II describes experimental measurements which show that the delay in phase and decrease in amplitude of fluorescence measured in simulated tissue phantoms varies as a function of dye lifetime. Part III describes the general theory behind the derivation of an optical property map from measurements of modulation phase and amplitude of fluorescent light detected at the tissue surface. Part IV presents actual images generated from simulated measurements of modulation phase and amplitude. Finally, the prognosis for moving these theoretical and computational studies into an experimental demonstration is commented upon.

1. PART I –PRINCIPLES OF PHOTON MIGRATION

1.1 Time and Frequency Domain Photon Migration

Photon migration techniques consist of measuring the time-dependent light propagation of multiply scattered light as it is transmitted through tissue. Two techniques are used to monitor the time-dependence of photon migration in a scattering medium: (i) time domain and (ii) frequency domain techniques. In the time domain technique, a picosecond impulse of light is launched into a scattering medium and the intensity of the detected light is recorded as a function of picosecond to nanosecond time. As time progresses, fewer photons are detected with longer "times-of-flight." Figure 1.2 shows the broadened pulse that is re-emitted and measured representing the distribution of photon "times-of-flight" traveled by the detected photons. In the frequency domain (Figure 1.3), incident light whose intensity is sinusoidally modulated is continuously launched into a scattering sample. As the "photon density wave" of light propagates, it experiences a phase lag and an amplitude reduction relative to the incident light. The phase-shift and amplitude modulation are related to the optical properties of the medium. Both the modulation phase and amplitude are measured as a function of multiple frequencies. The modulation ratio is defined as the modulation amplitude divided by the average intensity.

The intensity of the re-emitted light as a function of time (time domain), or the phase and amplitude of the modulated, re-emitted light as a function of the modulation frequency (frequency domain) contains identical information regarding the transport of light through the scattering medium. Time and frequency domain measurements are mathematically related to each other by the Fourier transform.

Photon migration imaging consists of (i) the forward problem of measuring the time-dependent characteristics of light propagation and (ii) the inverse problem of reconstructing an image of normal and diseased tissues based on their contrasting optical properties. In the following, the properties which impact the propagation of excitation light are reviewed.

1.2 Transport Property: Absorption Coefficient

The absorption coefficient, μ_a, is the inverse of the mean distance a photon will travel before being absorbed. In tissue, oxy- and deoxy-hemoglobin are the predominant endogenous absorbers in the therapeutic window (Figure 1.1). In this wavelength range, most tissues have an absorption coefficient in the range of 10^{-2} to 10^{-1} cm^{-1} [8].

In the absence of scattering, the absorption coefficient can be found from the attenuation of light directly using the Beer-Lambert Law,

$$\mu_a = -\frac{1}{L}\ln\frac{I}{I_o} = \epsilon_\lambda[C], \tag{1.1}$$

where μ_a is the absorption coefficient of the medium (cm^{-1}); L is the optical path length light travels (cm); I is the intensity of the detected light (number of photons/($\text{cm}^2\cdot\text{s}$)); I_o is the intensity of the incident light (number photons/($\text{cm}^2\cdot\text{s}$)); ϵ_λ is the extinction coefficient at wavelength λ (cm^{-1} mM^{-1}); and $[C]$ is the concentration of the light absorbing species (mM). Note that the number of photons per second can be converted into units of power (Watts) by multiplying by the photon's energy.

Equation 1.1 describes an absorption coefficient that is inversely related to the optical path length, L. In the presence of a scattering medium such as tissue, there is no unique path length, but rather a distribution of path lengths (Figure 1.4). Therefore, determination of the absorption coefficient in a scattering medium is not possible from the Beer-Lambert relationship.

1.3 Transport Property: Scattering Coefficient

The scattering coefficient, μ_s, describes the distance photons travel between scattering events. Scattering in tissue occurs due to the index of refraction mismatch between fluid and cellular organelles. Mitochondria are postulated to be the predominant scatterer in tissues [9, 10].

When multiple scattering occurs, light no longer follows a straight path. Instead, photons travel a distribution of optical path lengths, rendering the Beer-Lambert law invalid. As shown in Figure 1.4, the total optical path length, L, is now defined as the sum of all individual path, ℓ_i's, between scatters and the scattering coefficient is defined as the inverse of the mean scattering length, ℓ^*,

$$\mu_s = \frac{1}{\ell^*}. \tag{1.2}$$

Since "photon migration" describes a random walk of photons between scatterers, it is often more convenient to define the scattering parameter as the isotropic scattering coefficient [$\mu_s' = \mu_s(1-g)$] where the anisotropy coefficient, g, is defined below. In the near infrared wavelength range, the values of μ_s' for tissues typically range from 10 to 50 cm^{-1} [8].

1.4 Transport Property: Anisotropy Coefficient

The anisotropy coefficient, g, is defined as the mean cosine of the scattering angle at which a photon deflects from a scatterer. Flock *et al.* [11] have shown that the Henyey-Greenstein phase function describes the angular scatter of light in tissue. This phase function describes the relationship between g and the collimated transmittance, T_c, at a scattering angle θ where

$$T_c(\theta) = \frac{(1-g^2)}{(1+g^2-2g\cos\theta)^{3/2}} . \tag{1.3}$$

Collimated transmittance is a measure of the light intensity which is transmitted through the sample as a function of scattering angle, θ. Using a least squares analysis of several measurements of T_c versus θ, the anisotropy coefficient can be obtained from Equation 1.3. The anisotropy coefficient varies between isotropic ($g = 0$) and forward ($g = 1$) scattering. In all tissues, light is known to be forward scattering and the anisotropy coefficient is reported to be around 0.9 [12]. The Henyey-Greenstein phase function is widely used in tissue optics studies not only because it provides a good representation of experimental tissue measurements but also because it is mathematically simple.

1.5 Governing Equations Describing the Transport of Light

The scattering, absorption, and anisotropy coefficients are parameters that govern the propagation of light in any medium. Analysis of light transport is analogous to that of the motion of neutrons in a reactor core where neutrons diffuse from regions of high to low density [13]. When photons rather than neutrons are employed, the one-speed radiative transport equation describes light propagation in a scattering medium. The radiative transport equation is written in terms of the integro-differential equation governing the local number of photons, $n(\vec{r}, E, \hat{\Omega}, t)$, at position $\vec{r}$ and time t, and traveling with energy E and angular direction $\hat{\Omega}$ [14],

$$\begin{aligned}\frac{\partial n(\vec{r}, E, \hat{\Omega}, t)}{\partial t} &= -c\hat{\Omega} \cdot \nabla n - c\mu_t n(\vec{r}, E, \hat{\Omega}, t) + s(\vec{r}, E, \hat{\Omega}, t) + \\ &\int_{4\pi} d\hat{\Omega}' \int_o^\infty dE' c' \mu_s'(E' \rightarrow E, \hat{\Omega}' \rightarrow \hat{\Omega}) n(\vec{r}, E', \hat{\Omega}', t)\,. \end{aligned} \tag{1.4}$$

The term on the left hand side (LHS) represents the local accumulation of photons while the first term on the right hand side (RHS) represents the flux of photons into the system. The second term on the RHS represents the loss of photons traveling with energy E in direction $\hat{\Omega}$ due to absorption and scattering events. The total cross section for these extinction processes, μ_t, is given by the sum of the absorption and scattering cross sections, $\mu_t = \mu_a + \mu_s'$ (cm^{-1}). The third term on the RHS represents the source, and along with the second term accounts for the rate of addition of photons traveling direction $\hat{\Omega}$ with energy E which have been scattered from direction $\hat{\Omega}'$ and energy E'. To account for scattering from photons traveling all directions and energies, this last term on the RHS is integrated over all solid angles, $\int_{4\pi} = \int_o^{2\pi}\int_o^{\pi} \sin\theta d\theta d\phi$, and energies. The symbol c represents the speed of photons (cm/s).

1.5.1 One-Speed Approximation to the Transport Equation

When all the neutrons or photons travel at the same speed, the neutron transport equation can be reduced to the one-speed approximation by eliminating the dependence on energy, E. By writing the local concentration of photons in terms of an angular flux, φ (number of photons/(cm^2·steradians·s) where $\varphi(\vec{r},\hat{\Omega},t) = cn(\vec{r},\hat{\Omega},t)$, the one-speed equation is [13]

$$\frac{1}{c}\frac{\partial\varphi}{\partial t} = -\hat{\Omega}\cdot\nabla\varphi - \mu_t(\vec{r})\varphi(\vec{r},\hat{\Omega},t) + s(\vec{r},\hat{\Omega},t) + \int_{4\pi} d\hat{\Omega}'\mu_s'(\hat{\Omega}'\to\hat{\Omega})\varphi(\vec{r},\hat{\Omega}',t)\;. \quad (1.5)$$

The term $\hat{\Omega}\cdot\nabla\varphi$ represents the negative rate of addition of photons traveling an angular direction $\hat{\Omega}$. The term $\mu_t(\vec{r})\varphi(\vec{r},\Omega,t)$ accounts for the loss of photons traveling in direction $\hat{\Omega}$ due to scatter and absorption. The integral term represents photons scattering from direction $\hat{\Omega}'$ into the direction $\hat{\Omega}$. The term $s(\vec{r},\hat{\Omega},t)$ represent a source of photons (number of photons/(cm^3·steradians·s)) traveling in a direction $\hat{\Omega}$ at a position $\vec{r}$ and time t [13].

1.5.2 Diffusion Equation Describing Light Propagation in Tissues

Following the derivation of Duderstadt and Hamilton [13], the one-speed equation can be reduced to the diffusion equation describing light propagation in tissues

$$\frac{1}{c}\frac{\partial\Phi}{\partial t} = \nabla\cdot D(\vec{r})\nabla\Phi - \mu_a(\vec{r})\Phi(\vec{r},t) + S(\vec{r},t)\,. \quad (1.6)$$

Equation 1.6 represents the time domain diffusion equation which can analogously be written in the frequency domain as [14, 15]

$$\frac{i\omega}{c}\Phi^{AC}(\vec{r},\omega) - \vec{\nabla}\cdot D\vec{\nabla}\Phi^{AC}(\vec{r},\omega) + \mu_a\Phi^{AC} = M\delta(\vec{r_s}-\vec{r}), \quad (1.7)$$

where Φ^{AC} is the AC component of the fluence at position $\vec{r}$ and frequency ω; M is the modulation of the point source; and $\vec{r_s}$ denotes the source position.

1.5.3 Source Location and Boundary Conditions

A collimated light source incident on a scattering medium is slowly transformed into a diffuse source as it encounters scatterers. Patterson *et al.* [16] have analytically shown that in order to accurately represent an incident laser light source at the surface, the simulated source location has to be set to

$$z_o = \frac{1}{\mu_s'} \,. \tag{1.8}$$

Therefore, in order to accurately simulate a laser source located on the surface, the placement of the simulated source needs to be one isotropic scattering length inside the physical boundary. A sinusoidally modulated light source can be represented by a complex number [17]

$$S = S_o[\cos(\theta) + i\sin(\theta)] \,, \tag{1.9}$$

where θ and S_o are the phase and the amplitude of the source, respectively.

The three most common boundary conditions used to solve the diffusion equation at the air-scatterer interface of a random medium are the (i) zero fluence boundary condition, (ii) the partial current boundary condition and (iii) the extrapolated boundary condition. The zero fluence boundary condition defines $\Phi = 0$ on and outside the boundary. Although the zero fluence condition is physically inaccurate, it is mathematically simple and gives solutions to the diffusion equation which agree well with experimental data for biological systems [8].

1.6 Non-Radiative Mechanisms for Exogenous Contrast

As discussed above, the diffusion equation (Equations 1.6 and 1.7) describes the propagation of light in a highly scattering medium. This equation depends on three parameters: (i) the speed of light, c, (ii) the isotropic scattering coefficient, μ_s', and (iii) the absorption coefficient, μ_a. Since all these parameters govern the migration of photons in tissue, an exogenous compound which alters the characteristics of any of these parameters can be used to induce contrast for imaging and provide information for diagnostic information.

1.6.1 Contrast Owing to Absorption

The propagation of a photon density wave through a medium containing a region of light absorbing dye is different from the propagation of a wave in a medium with uniform optical properties as illustrated in Figure 1.5. The "homogeneous" propagation is similar to a wave formed by a pebble being dropped in a shallow pond. The propagating wave dampens as it travels across the surface but the wave maintains coherence. When the wave encounters an optical heterogeneity (or diseased tissue with different optical properties), it will reflect, diffract, and be absorbed [18]. The "heterogeneous" situation is similar to a pebble being dropped in the shallow pond with a solid obstruction in the wave's path. The solid obstruction will absorb and partially reflect a re-scattered wave. At any position, the diffusing wave will be the sum of the incident wave and the scattered wave.

Since these differences in light propagation enable contrast, photon migration measurements are conducted relative to an absence (homogeneous) condition. The phase contrast, $\Delta\theta$, and modulation contrast, ΔM, are defined as

$$\Delta\theta = \theta_{presence} - \theta_{absence} \tag{1.10}$$

$$\Delta M = \frac{M_{presence}}{M_{absence}}, \tag{1.11}$$

where $\theta_{presence}$ and $M_{presence}$ are respectively, the measured modulation phase and modulation ratio in the presence of a heterogeneity. Likewise, $\theta_{absence}$ and $M_{absence}$ are respectively, the measured modulation phase and modulation ratio in the absence of a heterogeneity. If the optical contrast relative to an absence condition is significant enough to cause $\Delta\theta \neq 0$ and $\Delta M \neq 1.0$, then it may be possible to reconstruct an interior optical property map from exterior measurements of modulation phase and amplitude as described in Part III.

Since phase and amplitude contrast depend on differences caused by an absorbing heterogeneity, the physics which change the detected wave need to be examined. Figure 1.6 (a) describes frequency domain photon migration imaging which consists of launching a sinusoidally modulated light source at position $\vec{r}_s$ and measuring the detected signal at position $\vec{r}_d$. The propagation of the wave through the medium causes a decrease in modulation and an increase in phase at position $\vec{r}$ relative to the incident wave. The magnitude of a scattered wave depends on the heterogeneity's distance from the source, its dimensions, and the absorption difference between it and the surroundings. The magnitude of a scattered wave will be greatest closest to the source. The greatest magnitude possible will occur when there is no loss mechanisms (no absorption) in the surroundings and the heterogeneity is a perfect absorber (a black body, or μ_a is infinity). Nonetheless, even for a perfect absorber, the incident propagated wave will constitute the predominant signal measured at the detector. Consequently, the scattered wave from an absorber will be small in comparison to the incident propagated wave and the contrast offered by absorption should be low. In other words, absorption contrast consists of the ability to detect a small scattered wave within a very large signal.

1.6.2 Contrast Owing to Dye with Fluorescent Characteristics

Another means to induce contrast is through fluorescence. Imagine an optical heterogeneity which contains a contrast agent that not only absorbs, but also fluoresces light (Figure 1.6 (b)). In essence, if an interference filter is placed at the detector so that only fluorescence light is seen, the heterogeneity would act like a beacon. Since there is no small signal to identify from a large background signal, the contrast should be significantly greater than that offered by absorption. Usually perfect uptake is not possible and one could imagine that while there is 10 fold or at most 20 fold more dye in a tissue volume of interest than in the surrounding tissues, the problem becomes one of picking the brightest beacon from a number of beacons uniformly distributed in the tissue (Figure 1.6 (c)). Under these conditions, the fluorescent properties (such as lifetime and quantum efficiency) of the compound may be used to impart additional contrast than that offered simply by a fluorophore concentration difference between the heterogeneity and its surroundings.

1.6.2.1 Physics of Photoluminence

Fluorescence is the emission of a photon which results when a molecule in an excited state relaxes to its original ground state (Figure 1.7). The excited molecules can either relax non-radiatively to the ground state (without emitting fluorescence) or stay in the excited state for a period of time before returning to the ground state and emitting a fluorescent photon. Often when pi orbitals are close, an electron in the electronically activated level will experience a change in its spin state. Since relaxation to the ground state populated with same spin state is forbidden, the activated molecule will remain in the excited state for a longer period of time. In this case the emission is termed phosphorescence. Due to the loss of energy associated when the fluorescent or phosphorescent molecules return to the ground state, the emission light occurs at a longer wavelength than the excitation light [19].

The fluorescent properties of a compound are characterized by the quantum efficiency, ϕ, and the lifetime, τ, of the molecule. The quantum efficiency is the ratio of the number of fluorescent photons emitted to the number of excitation photons absorbed by the fluorophore. The lifetime of the molecule is the average time that the molecule stays in the activated state and is measured as the average time between absorption of an excitation photon and emission of a fluorescent photon. Both lifetime and quantum efficiency are sensitive to the local bio-chemical environment. For example, porphyrin fluorescence is quenched by oxygen enabling quantitative detection of oxygen from the shortening of its lifetime and reduction of its quantum efficiency [19].

1.6.2.2 Measurement of Photolumination Properties in Dilute, Non-scattering Suspensions

The lifetime, τ, and quantum efficiency, ϕ, of a molecule can be determined using both a time and frequency domain analysis. In the time domain, a pulse of light excites a dilute non-scattering solution of fluorophores and the decay of the generated fluorescent intensity is recorded as a function of time after the initial impulse.

The amount of fluorescent light, I_m, is defined by the absorption coefficient of the fluorophores, $\mu_{a_{xf}}$, the quantum efficiency, ϕ, and the lifetime, τ, of the molecule [19],

$$I^m(t) = \frac{\phi\mu_{a_{xf}}}{\tau}e^{-1/\tau} = I_o e^{-1/\tau}, \tag{1.12}$$

where I_o is the maximum fluorescent intensity. The lifetime of a fluorophore is equal to the time required for the intensity to decay to 1/e of its initial value.

Frequency domain measurements of lifetime, τ, and quantum efficiency, ϕ, are made by exciting a dilute, non-scattering solution of fluorophore with a sinusoidally modulated source and measuring either the emitted modulation phase or modulation ratio of the fluorescent signal relative to the incident excitation light. The modulation phase of the fluorescent light is independent of the fluorophore concentration and the quantum efficiency,

$$\theta^m(\omega) = \tan^{-1}(\omega\tau), \tag{1.13}$$

where ω is the modulation frequency of the light source. The modulation ratio, however, is dependent on quantum efficiency, ϕ, and $\mu_{a_{xf}}$,

$$M^m(\omega) = \frac{\phi\mu_{a_{xf}}}{\sqrt{1+(\omega\tau)^2}}, \tag{1.14}$$

and can therefore be used to determine both lifetime, τ, and quantum efficiency, ϕ, of a sample. If the modulation ratio is referenced to the modulation ratio obtained under continuous wave or constant illumination ($\omega = 0$), the resulting ratio is a function of modulation frequency and lifetime, τ,

$$\frac{M^m(\omega)}{M^m(0)} = \frac{1}{\sqrt{1+(\omega\tau)^2}}\,. \tag{1.15}$$

Equations 1.13 – 1.15 are obtained from the Fourier transform of Equation 1.12.

The measurement of the emission properties of τ and ϕ are determined in a dilute, non-scattering medium. Since the fluorescent lifetime, τ, is on the same order as photon "times-of-flight," the equations above are not valid in a scattering medium due to the additional time delay and amplitude decrease associated with photon migration.

In order to accurately determine the emission properties in a scattering medium, photon migration times need to be deconvolved from time dependent measurements.

As an alternative, long lived (phosphorescent) probes have been suggested for photon migration measurements of the re-emission properties in a highly scattering medium since the phosphorescent lifetimes are longer than photon "times-of-flight." However, Hutchinson *et al.* [20, 21] found that the signal originating from a medium containing phosphorescent agents is confined to surface or sub-surface regions. Since phosphorescent agents cannot be used to determine the lifetime deep within scattering media, fluorescent contrast agents are suggested.

1.6.2.3 Collisional Quenching Mechanisms

Collisional quenching is the mechanism in which the fluorescent intensity decreases due to collisional encounters between a fluorophore and a quencher. For this process to happen, the quencher must diffuse to the fluorophore while the fluorophore is in the excited state. Some examples of collisional quenchers are oxygen, chloride, chlorinated hydrocarbons, xenon, hydrogen peroxide, bromate, and iodide [19]. The lifetime of a fluorophore can be related to the concentration of a quencher using the Stern-Volmer equation [19],

$$\frac{\tau_o}{\tau} = 1 + K_{SV}[Q], \tag{1.16}$$

where τ_o is the lifetime of the probe in the absence of a quencher, τ is the lifetime of the probe in the presence of a quencher, K_{SV} is the Stern-Volmer constant and $[Q]$ is the quencher concentration. As the concentration of the quencher increases, the excited state of the probe is quenched causing a reduction in the lifetime. Since the (bio-) chemical environment (amount of quencher present) impacts fluorescence lifetime, τ, fluorescent lifetime imaging may be used for metabolite sensing. It is important to note that Equation 1.16 does not depend on the concentration of fluorophore.

A class of lifetime sensitive fluorophores, called multi-plex dyes [22] involve "tuning" cyanine dyes to exhibit different spectra lifetimes depending on local environments and binding characteristics. This ability to change the emission characteristics between normal and diseased tissue using dyes whose characteristics change by varying pH [1, 2] and O_2 [3] may not only enhance detection but also may contain diagnostic information regarding the disease.

1.6.3 Diffusion Equations Describing Excitation and Emission Photon Migration

To use fluorescent contrast agents in the forward and the inverse imaging problems, fluorescent generation and propagation must be accurately modeled. The light propagation due to fluorescence in a scattering medium can be described by the coupled diffusion equations for light propagation [20, 23, 24],

$$-\nabla \cdot D_x(\vec{r})\nabla\Phi^x(\vec{r},\omega) + \left[\frac{i\omega}{c_x} + \mu_{a_{xi}}(\vec{r}) + \mu_{a_{xf}}(\vec{r})\right]\Phi^x(\vec{r},\omega) = S(\vec{r},\omega), \qquad (1.17)$$

$$-\nabla \cdot D_m(\vec{r})\nabla\Phi^m(\vec{r},\omega) + \left[\frac{i\omega}{c_m} + \mu_{a_m}(\vec{r})\right]\Phi^m(\vec{r},\omega) = \phi\mu_{a_{xf}}\frac{1 - i\omega\tau}{1 + (\omega\tau)^2}\Phi^x(\vec{r},\omega). \qquad (1.18)$$

In the above equations, Φ^x and Φ^m are the AC components of fluence for excitation (superscript x) and emission (superscript m) light (photons/cm^2); $\mu_{a_{xi}}$ is the absorption due to chromophores (cm^{-1}); $\mu_{a_{xf}}$ is the absorption due to fluorophores (cm^{-1}); μ_{a_m} represent the absorption of the emission light due to chromophores (cm^{-1}); μ_{s_x} and μ_{s_m} are the scattering coefficients of excitation and emission light (cm^{-1}), respectively; ϕ and τ are the quantum efficiency and lifetime (ns) of the fluorophore, respectively; and D_x and D_m are the optical diffusion coefficients for the excitation and emission light (cm) where

$$D_x = \frac{1}{3[\mu_{a_x} + (1-g)\mu_{s_x}]} \qquad (1.19)$$

and

$$D_m = \frac{1}{3(\mu_{a_m} + (1-g)\mu_{s_m})}\,. \qquad (1.20)$$

Equations 1.17, and 1.18 are coupled by the excitation fluence, Φ^x, and the absorption due to fluorescence, $\mu_{a_{xf}}$. The solutions for these equations, Φ^x and Φ^m, are complex.

It is important to note that fluorescence is assumed linear with the excitation fluence (e.g. photo-bleaching invalidates the model). The modulation phase, θ, and modulation amplitude, I_{AC}, of the excitation and emission light are represented by the real and imaginary components of the emission and excitation fluence,

$$\theta^{x,m} = \tan^{-1}\left[\frac{Im\Phi^{x,m}}{Re\Phi^{x,m}}\right] \tag{1.21}$$

$$I_{AC}^{x,m} = \sqrt{[Re\Phi^{x,m}]^2 + [Im\Phi^{x,m}]^2}\,, \tag{1.22}$$

and the modulation ratio is obtained by dividing I_{AC} by the average intensity (or I_{DC}),

$$M^{x,m} = \frac{\sqrt{[Re\Phi^{x,m}]^2 + [Im\Phi^{x,m}]^2}}{I_{DC}} = \frac{I_{AC}}{I_{DC}}\,. \tag{1.23}$$

The mathematical framework for predicting modulation phase and modulation amplitude at emission wavelengths assumes an angle exponential decay kinetics, but can be easily modified for other kinetics.

1.6.4 Potential Fluorescent Contrast Agents for Photon Migration Imaging

An example of a class of potential optical contrast agents are porphyrin derivatives. Porphyrin molecules have characteristic ring structures derived from four pyrrole rings joined together by four methene bridges as shown in Figure 1.8. Porphyrin derivatives are typically employed in photodynamic therapy (PDT). PDT is a method in which a hematoporphyrin derivative drug is administered for photo-therapeutic destruction of cancer [25]. In this therapy, a photosensitizing drug, which has a high affinity for tumor tissue, is systematically administered to the patient. The tumor area is then irradiated with red light which photoactivates the dye to a triplet state to produce cytotoxic by-products causing irreversible cellular damage. Many problems limit the efficacy of photodynamic therapy such as damage to skin exposed to sunlight. Nonetheless, while PDT agents depend upon triplet states for their therapeutic action, the singlet state may enable contrast for diagnostic imaging.

Indocyanine Green (ICG) (Figure 1.9) is another optically active contrast agent that is approved by the Food and Drug Administration (FDA) for diagnostic studies. It is currently used to diagnose retinal and chorodial diseases by enhancing the images of the retinal vasculature of the eye [26]. In burn diagnostics, ICG is administered to the blood stream after which the burn area is illuminated to monitor the amount of blood flow to the area. Because blood flow is proportional to the depth of the burn, ICG is used to measure the severity of the wound [27]. ICG is also used to determine hepatic function by monitoring the amount of dye that clears the circulatory system of the liver as function of time. Sevick *et al.* [4] measured the extinction coefficient, ϵ_λ, of ICG to be 1,300 $(\mathrm{M\ cm})^{-1}$ at 780 nm and 22,000 $(\mathrm{M\ cm})^{-1}$ at 830 nm. They also report the quantum efficiency, ϕ, and lifetime, τ, of ICG to be 0.016 and 0.56 ns, respectively. Although their measurements were conducted with ICG diluted in water, the properties are assumed to be reflective of those in 0.5% Intralipid.

2. PART II–CONTRAST FOR PHOTON MIGRATION IMAGING: FLUORESCENCE LIFETIME

2.1 Single Pixel Measurements for Photon Migration Imaging

To experimentally assess the feasibility of external contrast agents, the impact of absorbing and fluorescing heterogeneities on light propagation in a tissue simulating phantom was examined. Also, the influence of lifetime on photon migration measurements was investigated. Single pixel measurements of modulation phase, θ, and modulation ratio, M, were measured as a function of modulation frequency, ω, in the presence and absence of: (i) light-absorbing, and (ii) fluorescing objects.

2.2 Phantom Apparatus

The tissue phantom, illustrated in Figure 2.1, consisted of a Plexiglas cylindrical tank, 20 cm in diameter and 30.5 cm in height, filled with 8 liters of 0.5% by volume Intralipid solution (Kabi Pharmacia, Clayton, NC). This concentration of Intralipid mimics the scattering properties of tissue ($\mu_s' \approx 10$ cm^{-1}) [28]. Two small holes, an arc distance of 2.0 cm apart, were drilled half way up the side of the tank in order to couple the 1000 micron fiber optic (HCP-M1000T-08, Spectron Specialty Optics Co., Avon, CT) source and detector directly to the phantom. The fiber optics were placed approximately 1 mm inside the medium to avoid boundary effects caused by the wall of the tank. On the outside of the tank, silicon gel (Dow Corning Co., high vacuum grease, Midland, MI) was placed around the fibers, to prevent leakage of Intralipid.

The perfect absorbing heterogeneity was a 6 mm diameter glass rod painted black. The fluorescent body consisted of a 9 mm inner diameter cylindrical glass container filled with micromolar solutions of either 3,3'-Diethyl-thiatricarbocyanine iodide (DTTCI) (ACROS Organics, Fairlawn, NJ), a common laser dye, or ICG (Sigma Chemical Company, St. Louis, MO) diluted in 0.5% Intralipid solution. Dilution in Intralipid maintained a scattering coefficient inside the heterogeneity to be identical to the surrounding medium. Measurements of θ and M were conducted as the heterogeneity was moved various distances away from the wall midpoint between the source and detector. The object position was measured from the leading edge of the heterogeneity where a position of zero denotes contact between the heterogeneity and the wall of the tank.

2.3 Frequency Domain Instrumentation and Set-Up

The light propagation at both the excitation and emission wavelengths was measured using frequency domain measurements. The measurements were conducted at modulation frequencies between 80 and 240 MHz using a pulsed Ti:Sapphire laser, coupled to the detection system consisting of an ISS K2 phase fluorometer (ISS, Champaign, IL).

2.3.1 Heterodyne Detection Approach with Modulated Laser Source

To use simple electronics to detect the signal, a heterodyne technique was used. This detection method involves modulating the detectors at a frequency plus a small offset from the modulation frequency of the source. For example, the sinusoidal source is described by the expression

$$A\cos(\omega t + \theta), \tag{2.1}$$

where A is the amplitude, ω is the modulation frequency and θ is the phase of the source. The gain of the detector is modulated by $\omega + \Delta\omega$ so that the detector response is represented by

$$\cos[(\omega + \Delta\omega)t], \tag{2.2}$$

where $\Delta\omega$ is the small offset frequency of the detector. Then the signal obtained by the detector is

$$A\cos(\omega t+\theta)\times\cos[(\omega+\Delta\omega)t]=\frac{A}{2}\cos(\Delta\omega t+\theta)+\frac{A}{2}\cos[(2\omega+\Delta\omega)t+\theta]. \quad (2.3)$$

A low pass filter is used to filter out frequencies above $\Delta\omega$, the signal received by the detector is

$$\frac{A}{2}\cos(\Delta\omega t+\theta). \quad (2.4)$$

It is important to note that the phase and amplitude information of the high frequency signal is preserved.

2.3.2 Heterodyne Detection Approach with Pulsed Laser Source

When the light source is a mode locked pulsed laser, the signal can no longer be described by Equation 2.1. Instead, the source is represented by

$$\sum_{n=1}^{\infty} A_n\cos(n\omega t+\theta_n), \quad (2.5)$$

where the above equation is the frequency domain representation of a mode locked pulsed laser [29]. Again the detector is modulated at a frequency plus a small offset as described by Equation 2.2, the signal obtained by the detector is

$$\begin{aligned}\cos[(\omega+\Delta\omega)t]\times[A_1\cos(\omega t+\theta_1)+A_2\cos(2\omega t+\theta_2)+\ldots] &=\\ &+\frac{A_1}{2}\{\cos(\Delta\omega t+\theta_1)+\cos[(2\omega+\Delta\omega)t+\theta_1]\} \quad (2.6)\\ &+\frac{A_2}{2}\{\cos[(\omega+\Delta\omega)t+\theta_2]+\cos[(3\omega+\Delta\omega)t+\theta_2]\}+\ldots\end{aligned}$$

Filtering out frequencies above $\Delta\omega$, the signal received by the detector is

$$\frac{A_1}{2}\cos(\Delta\omega t+\theta_1) \quad (2.7)$$

which is completely analogous to Equation 2.4.

2.3.3 Instrumentation

The excitation light source consists of a Ti:Sapphire laser pumped by a 10 Watt Argon ion laser (Spectra Physics, CA) to produce a pulse train of 2 ps at a repetition rate of 80 MHz (Figure 2.2). The output wavelength of the Ti:Sapphire laser is set to 780 nm. To establish a phase lock with the detection equipment, an 80 MHz signal origination from the Ti:Sapphire laser is sent to a divide–by–8 circuit resulting in a 10 MHz signal. This 10 MHz signal is sent to a frequency synthesizer (Model 2022D, Marconi, Allendale, NJ) which controls the modulation of the detectors. The detectors are modulated at frequencies of 80, 160 and 240 MHz. The light from the Ti:Sapphire laser has 1.3 Watts of average power.

The pulse train is focused onto a beam splitter. The unreflected portion of the pulse train (approximately 90% of the signal) serves as the light source and is focused onto a fiber optic coupled to the side of the cylindrical tank. The reflected portion of the signal is focused onto another fiber optic cable which delivers the signal to a reference photomultiplier tube (PMT). This light serves as the reference signal. The scattered excitation and emission light detected at the periphery of the phantom is delivered to a sample PMT also using a fiber optic cable. An 830 nm interference filter (10-830-4-1.00, CVI Laser Co, Albuquerque, NM) is placed in front of the sample PMT and is used to make frequency domain measurements at the emission wavelengths.

The gain of the PMTs are modulated at a harmonic of the source frequency but offset by 100 Hz in order to produce a heterodyne signal. The output from both PMTs is sent to an ISS board for data acquisition. The modulated phase and amplitude are extracted from the signal at the 100 Hz cross correlation frequency through simple electronics and software (ISS, Champaign, IL).

2.4 Contrast Owing to Perfect Absorption and Perfect Uptake of Fluorescence

The modulation phase and modulation ratio were measured to evaluate the contrast offered by (i) a perfect absorber and (ii) a fluorescent volume in a lossless scattering medium (no absorption in the surrounding). Since the fluorescent object had perfect uptake of dye and since the absorber was a black rod, they represent the best possible contrast owing to absorption and fluorescence. For this experiment DTTCI served as the fluorescent contrast agent.

Measurements of modulation phase, θ, and modulation ratio, M, were conducted as the heterogeneities were moved from the peripheral location towards the center of the phantom. Figure 2.3 shows the phase contrast, $\Delta\theta$ ($\theta_{presence} - \theta_{absence}$), due to the presence of both an absorbing and a fluorescing heterogeneity at 80, 160, and 240 MHz modulation frequencies. The largest phase contrast is measured at 240 MHz and the signal is only altered by approximately 20° for absorption, however for fluorescence, an alteration of approximately 60° is observed. Therefore, these results show that the best contrast available from absorption (i.e., a perfect absorber) causes a smaller measurable disturbance in photon migration than a micromolar concentration of fluorescent dye. Also, the fluorescent signal is detected approximately 1 cm deeper than the absorbance signal.

Measurements of modulation ratio, M, for the perfect absorber and the fluorescent volume were not performed. However, a similar experiment conducted by Lopez [30] using a 9 mm diameter perfect absorbing fluorescent object shows that the modulation contrast ($M_{presence}/M_{absence}$) of the fluorescent object at 240 MHz is approximately 0.1 while the absorber only offers 0.6 contrast. These results are consistent with what is expected.

In a realistic situation, the administration of contrast agents results in the imperfect uptake of dye into tissue regions of interest. Recently, Lopez *et al.* [4, 30] have conducted measurements of phase and modulation contrast with imperfect uptake ratios of 1:100 and 1:10 with a similar experimental apparatus as described above. They found the resulting phase contrast to be dramatically smaller than the situation of perfect uptake. However, the magnitude of contrast offered by fluorescence phase contrast and modulation contrast still exceeds absorption contrast, which is in agreement with the work above. As discussed in Part I, the additional time-delay associated with the lifetime of a fluorescent molecule during the emission process causes a greater phase and modulation contrast over that of absorption.

2.5 Contrast Owing to the Influence of Lifetime

The next experiment assessed the influence of lifetime on contrast. In an analogous single pixel experiment to the one described above, Intralipid solutions with micromolar concentrations of DTTCI and ICG were investigated and compared to each other since DTTCI and ICG have different lifetimes of 1.18 and 0.56 ns, respectively [4].

Dilute non-scattering solutions of both DTTCI and ICG were separately analyzed in a small glass cuvette. Using the instrumentation discussed above, measurements of modulation phase and modulation ratio were conducted with the source at a right angle from the detector. Using a third dye, IR-140 (ACROS Organics, Fairlawn, NJ), as a standard, the lifetimes of DTTCI and ICG were obtained by evaluating the equations discussed in Section 1.6.2.1.

Both the modulation phase and modulation ratio were measured as a function of frequency as DTTCI and ICG scattering solutions were moved from the periphery to the center of the phantom. Figure 2.4 and Figure 2.5 illustrate the phase contrast for DTTCI and ICG, respectively. As the lifetime of the dye increases, the phase contrast should also increase and the modulation ratio should decrease (see Part I). Since the lifetimes of DTTCI and ICG are 1.05 and 0.58 ns respectively, the phase contrast for DTTCI should be larger and the modulation contrast should be smaller. This is indeed the case since DTTCI shows values of $\Delta\theta = 60°$ and $\Delta M = 0.3$ and ICG shows values of $\Delta\theta = 46°$ and $\Delta M = 0.5$. These results confirm that frequency domain measurements contain information of fluorescent lifetime.

2.6 Discussion

The results in this section show that fluorescence offers improved contrast over absorption. Since measurements were conducted on a perfect absorber, the findings suggest that the endogenous contrast due to absorption from increased hemoglobin associated with angiogenesis may be too small for realistic measurements for optical tomography (Figure 1.6). The second study shows that frequency domain measurements contain lifetime information which can provide diagnostic information about the local bio-chemical environment (see Equation 1.16). However, these measurements need to be coupled to an inversion algorithm in order to extract the lifetime from the scattered signal (see Part III for more details). The single pixel measurements presented here show great promise for the detection of diseased tissues laden with contrast agents using photon migration measurements. But single pixel measurements only provide one dimensional information and therefore cannot be used to resolve an interior image of optical properties. To obtain enough information to locate a heterogeneity, measurements at multiple locations need to be obtained.

3. PART III–RECONSTRUCTION OF FLUORESCENCE QUANTUM EFFICIENCY AND LIFETIME

3.1 INVERSE IMAGING PROBLEM

Recently, we have developed multi-pixel measurements for rapid data acquisition of modulation phase and amplitude of re-emitted optical signals [31]. Using a gain-modulated image intensifier coupled to a CCD camera, acquisition of 128 × 128 measurements of modulation phase and amplitude are enabled in approximately 10 milliseconds at excitation wavelengths and 1 second at emission wavelengths. In order to employ these measurements to reconstruct interior maps of lifetime and quantum efficiency from exterior frequency domain measurements made at the periphery, an inverse algorithm needs to be employed. Currently, two approaches for solving the inverse imaging problem have been demonstrated. Both approaches involve solutions to the diffusion equation where the first method uses perturbation expansions of the photon diffusion equation [32, 33, 34, 35] and the second solves the diffusing equation directly using a finite difference or a finite element approach [36, 37, 38, 39, 40].

In this work, we employ the latter approach to reconstruct optical property maps of absorption, fluorescent quantum efficiency, and fluorescent lifetime of an optical heterogeneity without *a priori* information of position or volume. Specifically, the tissue volume of interest is mathematically represented by discretized volume elements in which the optical properties of absorption, fluorescence quantum efficiency and lifetime are constructed. The inversion schemes incorporate an iterative Newton-Raphson technique to update values of the optical properties at every volume element in order to minimize the least-squares-difference between the experimental and calculated detector responses at the periphery. The method is similar to that used by

Yorkey *et al.* [41] for electrical impedance tomography, Pogue *et al.* [37] for absorption and scattering reconstructions, and Paithankar *et al.* [40] who performed reconstructions on both fluorescent lifetime, τ, and fluorescent yield (the product of the absorption coefficient due to fluorophores and quantum efficiency, $\phi\mu_{a_{xf}}$). In this section, interested readers will find the numerical technique used in solving the forward problem along with the approach to solving the inverse imaging problem. Finally, applications of the inversion to simulated data are presented in Part IV illustrating the feasibility of fluorescent quantum efficiency and lifetime imaging in tissues and other scattering media. Part III may be omitted by those readers un-interested in the mathematics of solving the forward and inverse imaging problems.

3.1.1 Forward Problem

The coupled diffusion equations for excitation and emission light propagation (Equations 1.17 and 1.18) are complex linear elliptic equations which can be analytically solved as boundary value problems when the optical properties are independent of spatial position. The complex fluence can be used to predict modulation phase and amplitude from the real and imaginary components. However, when there is a spatial variation in optical properties (such is the case when an optical heterogeneity is present) numerical solutions are necessary. In this work, the finite difference method was used to solve for both the excitation fluence, $\Phi^x(\vec{r},\omega)$, and the emission fluence, $\Phi^m(\vec{r},\omega)$. The method of finite differences involves discretizing the area of interest into a grid and a linear system is obtained by approximating derivatives in the diffusion equation by differences.

In this study, a two-dimensional simulated tissue phantom as shown in Figure 3.1 was employed. The phantom is modeled as a 4 $\times$ 4 cm^2 square surface with a 17 $\times$ 17 grid representing the area of potentially differing optical properties. The source and the detector locations were placed one pixel in from the edge of the phantom to overcome the effects of the zero fluence boundary condition. A source is centered on each side of the phantom for a total of 4 sources. The grid contains 56 detectors per source evenly spaced around the phantom. The placement of the source represents an isotropic excitation source located 0.25 cm or 2.5 scattering lengths from the surface. Since all the experiments discussed here are performed using simulated data, the placement of the source will not affect the solution to the inversion. However, when this algorithm is coupled to experimental measurements, the placement of the source needs to be correctly represented.

For solutions of the forward problem, the known optical properties of the background and the object are input as parameters into the program and then the fluence at each grid point is calculated. The fluence values are used at the detector positions and the modulation phase, $\theta^{x,m}$, and the log of the modulation amplitude, $I_{AC}^{x,m}$, are calculated from both the real and imaginary components of the excitation or emission fluence, $\Phi^{x,m}$, where

$$\theta^{x,m} = \tan^{-1}\left[\frac{Im\Phi^{x,m}}{Re\Phi^{x,m}}\right] \times \frac{360}{2\pi} \tag{3.1}$$

$$I_{AC}^{x,m} = \log_{10}\sqrt{[Im\Phi^{x,m}]^2 + [Re\Phi^{x,m}]^2}. \tag{3.2}$$

To run a single simulated experiment, only one source is active. For each forward solution, values of $\theta^{x,m}$ and $I_{AC}^{x,m}$ are calculated at all the detector positions. Once these detector values are obtained, the forward solution is repeated for the next source location. This procedure continues until all four sources are investigated. A total of four simulated experiments constitute the data to be acquired experimentally. Consequently, the simulations will yield a total of 224 detector measurements. In all the simulated experiments, the sources are modulated at a frequency of 100 MHz. Typical forward calculations on a Ultra 2 Sun workstation took approximately 1.3 s.

After detector data is evaluated for $\theta^{x,m}$ and $I_{AC}^{x,m}$, simulated Gaussian noise with a standard deviation of 0.1° for phase and 1% for modulation amplitude is added using a MATLAB routine. The Gaussian noise is added to account for the noise which would be encountered in a real experiment. The simulated forward results with added noise are then input to the inversion algorithm.

3.1.2 Solution to the Inverse Problem

The solution to the inverse problem requires reconstructing images of the interior volume from exterior measurements of $\theta^{x,m}$ and $I_{AC}^{x,m}$. Since more information from exterior measurements enable better image reconstruction, more detectors and multiple modulation frequencies should improve image reconstructions. The inversion algorithm is conducted in two parts on the basis of (i) absorption at the excitation wavelength due to fluorophores, $\mu_{a_{xf}}$, and (ii) quantum efficiency, ϕ, or lifetime, τ, at the emission wavelength. The two parts are similar except the reconstruction based on $\mu_{a_{xf}}$ uses detector data at the excitation wavelength while the other part uses data at the emission wavelength.

Figure 3.2 depicts the flow diagram for these inversion algorithms. To begin the inverse calculation based on $\mu_{a_{xf}}$, an initial homogeneous guess for the optical property map is given. Typical values are those found in normal tissues. From these values the forward solution is calculated to obtain θ^x and I_{AC}^x measurements at the detector positions for the excitation light. Next, two Jacobian matrices, $\mathbf{J}(\theta^x,\mu_{a_{xf}})$ and $\mathbf{J}(I_{AC}^x,\mu_{a_{xf}})$, are constructed where an entry of each matrix is defined as $j_{ij} = \partial\theta_i^x/\partial\mu_{a_{xf},j}$ and $j_{ij} = \partial I_{AC_i}^x/\partial\mu_{a_{xf},j}$, respectively. Each element of the matrix describes the response of the source-detector pair at position i to changes in $\mu_{a_{xf}}$ at each pixel j. The partial derivatives are numerically approximated by calling the forward solution (Cud2) a second time for a 1% increase of the original pixel value for $\mu_{a_{xf}}$ and subtracting the difference (i.e. $\partial\theta^x/\partial\mu_{a_{xf}} \approx \Delta\theta^x/\Delta\mu_{a_{xf}}$ and $\partial I_{AC}^x/\partial\mu_{a_{xf}} \approx \Delta I_{AC}^x/\Delta\mu_{a_{xf}}$).

To update $\mu_{a_{xf}}$, an iterative Newton-Raphson technique involving the Jacobians was used,

$$\left[\frac{\mathbf{J}^T(\theta^x,\mu_{a_{xf}})\mathbf{J}(\theta^x,\mu_{a_{xf}})}{\sigma_\theta^2} + \frac{\mathbf{J}^T(I_{AC}^x,\mu_{a_{xf}})\mathbf{J}(I_{AC}^x,\mu_{a_{xf}})}{\sigma_{I_{AC}}^2} + \xi\mathbf{I}\right]\left[\Delta\vec{\mu}_{a_{xf}}\right] =$$
$$\left[\frac{\mathbf{J}^T(\theta^x,\mu_{a_{xf}})}{\sigma_\theta^2}\left(\vec{\theta}_{obs}^x - \vec{\theta}_{cal}^x\right) + \frac{\mathbf{J}^T(I_{AC}^x,\mu_{a_{xf}})}{\sigma_{I_{AC}}^2}\left(\vec{I}_{AC_{obs}}^x - \vec{I}_{AC_{cal}}^x\right)\right], \qquad (3.3)$$

where $\Delta\vec{\mu}_{a_{xf}}$ provides an increment change for updating $\mu_{a_{xf}}$ and ξ is a regularization parameter multiplied by the identity matrix, **I**. Because the Jacobian matrices are ill conditioned due to the small sensitivity of $\mu_{a_{xf}}$ far away from the source and detector, the regularization parameter compensates by making the matrices more diagonally dominant. The parameter ξ is then adjusted by a Marquardt-Levenberg algorithm at every iteration [37]. In order to solve the linear algebraic equations (Equation 3.3) for $\Delta\vec{\mu}_{a_{xf}}$, a LU decomposition back substitution method is used. The updated optical property map is then found by adding $\Delta\vec{\mu}_{a_{xf}}$ to the values from the previous iteration.

The forward solution is re-calculated using the new updated values in order to determine the reconstruction error,

$$\chi^2_x = \frac{1}{4nd}\sum_{k=1}^{4}\sum_{i=1}^{nd}\left[\left(\frac{\theta^x_{cal,i} - \theta^x_{obs,i}}{\sigma_\theta}\right)^2 + \left(\frac{I^x_{AC_{cal,i}} - I^x_{AC_{obs,i}}}{\sigma_{I_{AC}}}\right)^2\right], \qquad (3.4)$$

where nd is the total number of detectors (56), θ^x_{cal} and $I^x_{AC_{cal}}$ are the predicted detector data and θ^x_{obs} and $I^x_{AC_{obs}}$ are the simulated experimental detector data for the excitation light. Again, σ_θ and $\sigma_{I_{AC}}$ are the typical standard deviations of noise in the measurements taken to be 0.1° and 1%, respectively. For comparison, our multi-pixel measurements have errors on the order of 0.2° and 1.8%. The values of σ_θ and $\sigma_{I_{AC}}$ are scale factors that describe the confidence in the measurement. Every node on the grid will yield an equation and the only known variables are at the detector positions. Since there are many more nodes than detectors, the inversion scheme is underconstrained and not guaranteed to converge on the actual optical property map.

The entire procedure of iteratively adjusting $\mu_{a_{xf}}$ to minimize the χ^2_x error continues until a predetermined convergence criterion is met. The criterion is met if any of the following quantities: (i) the value of χ^2_x, (ii) the absolute change in χ^2_x, or (iii) the relative change in χ^2_x become lower than 1.0 $\times 10^{-5}$ or a maximum of 50 iterations is reached. Typical times to complete the inverse solution are approximately 45 minutes on a Ultra 2 Sun workstation.

If only a map of $\mu_{a_{xf}}$ is desired, the program stops. Otherwise, the map of $\mu_{a_{xf}}$ is used in order to compute a second map of either ϕ or τ. Currently, the computation of the maps of ϕ and τ are conducted in two separate programs in order to evaluate their individual performances.

After the loop in which the map $\mu_{a_{xf}}$ is calculated, the forward solution is now calculated to obtain θ^m and I_{AC}^m measurements at the detector positions for the emission light using the homogeneous map described above except with the updated values of $\mu_{a_{xf}}$. Next, two Jacobian matrices are constructed: $\mathbf{J}(\theta^m,\phi)$ and $\mathbf{J}(I_{AC}^m,\phi)$ for the reconstruction of ϕ, or $\mathbf{J}(\theta^m,\tau)$ and $\mathbf{J}(I_{AC}^m,\tau)$ for reconstruction of τ. Each element of these Jacobian matrices is defined as $j_{ij} = \partial\theta_i^m/\partial\phi_j$, $j_{ij} = \partial I_{AC_i}^m/\partial\phi_j$, $j_{ij} = \partial\theta_i^m/\partial\tau_j$, and $j_{ij} = \partial I_{AC_i}^m/\partial\tau_j$, respectively. Again, each element of the Jacobian matrix describes the response of the source-detector pair at position i to changes in ϕ or τ at each pixel j. The partial derivatives are approximated as described above where $\partial\theta^m/\partial\phi \approx \Delta\theta^m/\Delta\phi$, $\partial I_{AC}^m/\partial\phi \approx \Delta I_{AC}^m/\Delta\phi$, $\partial\theta^m/\partial\tau \approx \Delta\theta^m/\Delta\tau$, and $\partial I_{AC}^m/\partial\tau \approx \Delta I_{AC}^m/\Delta\tau$.

Equations 3.5 and 3.6 provide updates of ϕ and τ by adding $\Delta\vec{\phi}$ and $\Delta\vec{\tau}$, respectively, to the values of ϕ and τ from the previous iteration,

$$\begin{aligned}&\left[\frac{\mathbf{J}^T(\theta^m,\phi)\mathbf{J}(\theta^m,\phi)}{\sigma_\theta^2}+\frac{\mathbf{J}^T(I_{AC}^m,\phi)\mathbf{J}(I_{AC}^m,\phi)}{\sigma_{I_{AC}}^2}+\xi\mathbf{I}\right]\left[\Delta\vec{\phi}\right]= \\ &\left[\frac{\mathbf{J}^T(\theta^m,\phi)}{\sigma_\theta^2}\left(\vec{\theta}_{obs}^m-\vec{\theta}_{cal}^m\right)+\frac{\mathbf{J}^T(I_{AC}^m,\phi)}{\sigma_{I_{AC}}^2}\left(\vec{I}_{AC_{obs}}^m-\vec{I}_{AC_{cal}}^m\right)\right]\end{aligned} \tag{3.5}$$

and

$$\begin{aligned}&\left[\frac{\mathbf{J}^T(\theta^m,\tau)\mathbf{J}(\theta^m,\tau)}{\sigma_\theta^2}+\frac{\mathbf{J}^T(I_{AC}^m,\tau)\mathbf{J}(I_{AC}^m,\tau)}{\sigma_{I_{AC}}^2}+\xi\mathbf{I}\right]\left[\Delta\vec{\tau}\right]= \\ &\left[\frac{\mathbf{J}^T(\theta^m,\tau)}{\sigma_\theta^2}\left(\vec{\theta}_{obs}^m-\vec{\theta}_{cal}^m\right)+\frac{\mathbf{J}^T(I_{AC}^m,\tau)}{\sigma_{I_{AC}}^2}\left(\vec{I}_{AC_{obs}}^m-\vec{I}_{AC_{cal}}^m\right)\right].\end{aligned} \tag{3.6}$$

Again, the forward solution is re-calculated using the updated values in order to determine the reconstruction error,

$$\chi_m^2=\frac{1}{4nd}\sum_{k=1}^{4}\sum_{i=1}^{nd}\left[\left(\frac{\theta_{cal,i}^m-\theta_{obs,i}^m}{\sigma_\theta}\right)^2+\left(\frac{I_{AC_{cal,i}}^m-I_{AC_{obs,i}}^m}{\sigma_{I_{AC}}}\right)^2\right], \tag{3.7}$$

where θ_{cal}^m, $I_{AC_{cal}}^m$ are the predicted detector data and θ_{obs}^m and $I_{AC_{obs}}^m$ are the simulated experimental detector data for the emission light. The values for σ_θ and $\sigma_{I_{AC}}$ are the same as in the absorption reconstruction, 0.1° and 1.0%, respectively. The entire procedure of iteratively adjusting ϕ or τ to minimize the χ_m^2 error continues until the same convergence criterion as above is met or 50 iterations have passed.

4. PART IV–RECONSTRUCTION OF ABSORPTION AND FLUORESCENCE QUANTUM EFFICIENCY AND LIFETIME IN A SCATTERING MEDIUM

4.1 Results for the Reconstruction Algorithm

Three different types of simulations were separately performed. They included reconstructions on the basis of either absorption, $\mu_{a_{xf}}$, quantum efficiency, ϕ or lifetime, τ. In all three classes of simulated experiments, an optical heterogeneity was 0.063 cm^2 which constituted 0.39% of the total area. During the reconstructions of both ϕ and τ unphysically high optical property values around the periphery and especially near the source locations were obtained. These values were replaced with the average background value with a constraint statement inside the program.

For all the reconstructions, values of $\mu_{a_{xf}}$ range from 0.010 to 0.200 cm^{-1}. These values of absorption correspond to an ICG concentration of approximately 0.076 to 1.53 μM [4]. These ICG concentrations are well below lethal levels and are approximately 5 to 60 times lower than the therapeutic concentrations currently administered with many photodynamic agents [42, 43].

4.2 Reconstruction of the Absorption Coefficient from Excitation Light

This section describes the simulations performed on the basis absorption due to fluorophores, $\mu_{a_{xf}}$, at the excitation wavelength. Figure 4.1 illustrates both simulated and reconstructed data as an optical tissue heterogeneity is moved diagonally towards the detectors at three different object locations. The heterogeneity contains twenty fold more absorbing dye than its surroundings (see Table 4.1). The experiment shows that the heterogeneity location is successfully reconstructed. However, since the program preserves the average pixel value, a smoothing of the reconstructed image is observed causing the magnitude of $\mu_{a_{xf}}$ for both the object and the surroundings to be incorrect as shown in Table 4.1. As the object moves closer to the detectors, less error in the reconstruction is obtained since the value of $\mu_{a_{xf}}$ inside the object increases while the value in the background decreases. In fact, the value of $\mu_{a_{xf}}$ at the closest object position is 0.068 cm^{-1} (case c) is twice the values of the farthest position (0.034 cm^{-1}, case a). This reduction of error is expected since there is more signal yielding a larger disturbance to be measured at the detectors. In other words, a heterogeneity present close to the source and detector will have more influence on the inversion problem since the pixels closer to the source and detectors have more influence on the measured signal making the solution better defined. Successful reconstructions have also been performed for a more realistic uptake of 10:1 as well as higher resolutions (33×33 grid) [44].

4.3 Reconstruction of Quantum Efficiency from Emission Light

The performance of the inverse algorithm for reconstructing maps of quantum efficiency, ϕ, using detector data at the emission wavelength is discussed in this section. For all the inversions discussed here, the exact value of $\mu_{a_{xf}}$ inside the object was input into the initial homogeneous guess. This procedure causes the inversion algorithm to converge after one iteration in the excitation loop and the exact value of $\mu_{a_{xf}}$ to be used in the emission loop in order to only investigate the reconstruction on ϕ. Table 4.2 lists all the optical properties and experimental parameters used in the forward solutions to generate the simulated detector data and compares the values from the forward solution to those obtained by the inversion solution.

Figure 4.2 shows the (a) actual solution, (b) the reconstruction, and (c) the value of ϕ inside the object as a function of iteration number. The experiment ended after 50 iterations without meeting any of the convergence criteria. The optical property map of the reconstruction shows that the location of the object is successfully located but the value of ϕ inside the object only reaches 0.082 (18% smaller than the actual value of 0.100). Also, the background pixel values are noisy with an average value of 0.012 which is 20% larger than the actual value of 0.010.

4.4 Reconstruction of Lifetime from Emission Light

The performance of the inversion algorithm for reconstructing lifetime, τ, using detector data at the emission wavelength is discussed in this section. Similar to the reconstructions of ϕ, all the inversions in this section use the exact value of $\mu_{a_{xf}}$ inside both the object and background for the initial optical property map. This procedure causes the inversion algorithm to converge after one iteration in the excitation loop and the exact value of $\mu_{a_{xf}}$ to be used in the emission loop to investigate the reconstruction of τ only.

The lifetime reconstruction for a 10:1 uptake of dye, the current uptake ratio for available contrast agents, was investigated. Table 4.3 lists all the optical properties and experimental parameters used in the forward solution to generate the detector data and compares the values from the forward solution to those obtained by the inverse solution. This particular simulation had an arbitrary lifetime value of 1.00 ns inside the object and a 10.0 ns everywhere else. Figure 4.3 (a) shows the actual spatial map, (b) the reconstructed spatial map, and (c) the average value of τ as a function of iteration number inside the object. Because τ inside the object was lower than in the background, the object location is defined as the pixel with the lowest value of τ. Both the location and magnitude of τ inside the object are correctly found since the reconstructed value for pixel (11,7) is 0.996 ns, only 0.04% lower than the actual value. The reconstruction for the background gives a good convergence of 10.1 ns even though the background contains a small amount of noise which is symmetric about the object. This noise is most likely an artifact from the large fluence that emerges from the four source locations.

4.5 Discussion

Numerical simulations were conducted in order to examine the resolution and accuracy of the reconstruction method. These results show the potential of photon migration for the optical detection of a heterogeneity inside a scattering medium. The simulated experiments based on $\mu_{a_{xf}}$ can locate an absorbing heterogeneity inside a tissue simulating phantom, however the magnitude of $\mu_{a_{xf}}$ inside the heterogeneity is smaller than the actual solution. The simulated experiments also show the ability to reconstruct the interior optical property maps for both quantum efficiency and lifetime using detector information at the emission wavelength. Reconstructing maps of lifetime not only provides object location but also may provide information regarding the environment (see Section 1.16 for discussion on the Stern-Volmer equation). This information about the local bio-chemistry can help to differentiate normal from diseased tissue.

To couple these inversion algorithms with experimental measurements, all the optical coefficients of the background need to be scaled by a factor of $(3/2)^{1/2}$ to account for the two dimensional nature of the algorithm and the three dimensional nature of the experiment [45]. The noise for the fluorescent measurements needs to be determined since it is unlikely to be the same as the excitation data (0.1° for θ^x and 1% for I^x_{AC}). Also, both inversions assume that the noise is uniform over the entire region which may not be the actual situation, and updates to the inversion scheme, which take the noise as a function of position into account, need to be implemented.

To further improve the reconstructions, detector information at multiple modulation frequency needs to be incorporated into the algorithm. Multiple frequency information will provide more detector information helping with the underconstrained nature of the inversion problem.

4.6 Conclusion

Absorption and fluorescent methods of inducing contrast were examined using single pixel measurements. The results in this study show that fluorescence has improved contrast over absorption due to the additional mechanism from the kinetics of the fluorescence decay process. Also, it was demonstrated that lifetime differences alter the propagation of the detected signal. Since targeted delivery of a contrast agent may not always be feasible, lifetime sensitive dyes which are specific to different environmental conditions found in normal and diseased tissue may enhance detection.

Acknowledgments

This work was supported in part by the National Institutes of Health (R01CA61413, R0167176-01 and K04CA687374-01).

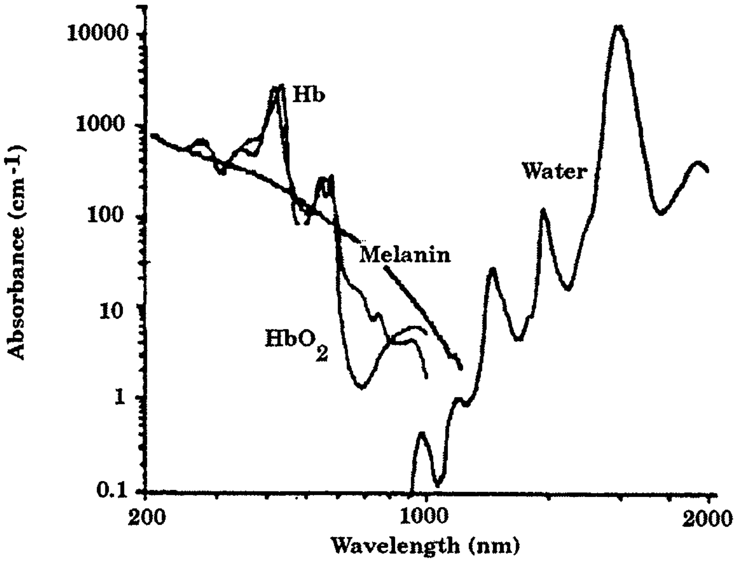

Figure 1.1. Dependence of absorption on wavelength illustrating the "therapeutic window" in which the propagation of light through tissue is high. Reproduced from Reference [7].

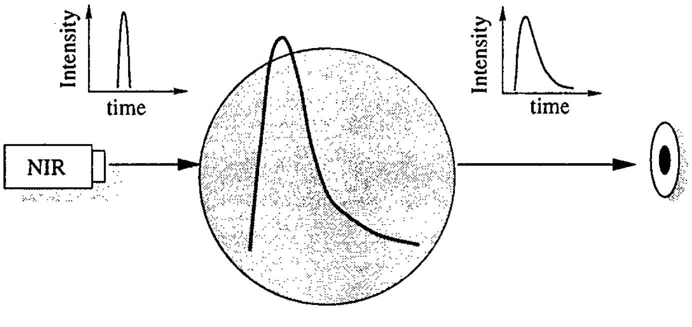

Figure 1.2. In the time domain, an impulse of light is launched into a scattering medium. The detected pulse is broadened due to the increase in photon "times-of-flight."

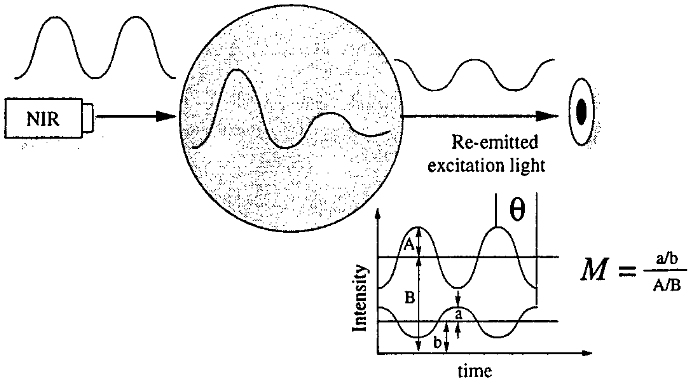
NIR
Re-emitted
excitation light
θ
A
B
a
b
Intensity
time
M = a/b / A/B

Figure 1.3. In the frequency domain, a sinusoidally modulated source is launched into a scattering medium. The detected signal's phase is shifted and amplitude is decreased relative to the incident light.

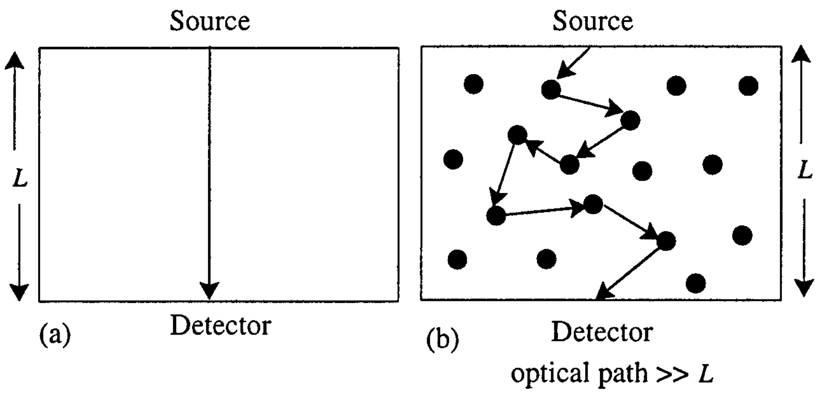
Source
Source
L
L
(a)
Detector
(b)
Detector
optical path >> L

Figure 1.4. Light propagation in a (a) non-scattering and (b) scattering medium.

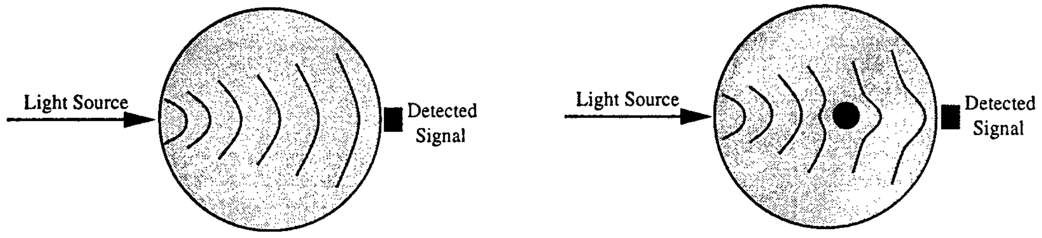
Light Source
Detected
Signal
Light Source
Detected
Signal

Figure 1.5. Schematic describing the propagation of a photon density wave across a medium in the absence and presence of a heterogeneity with optical contrast.

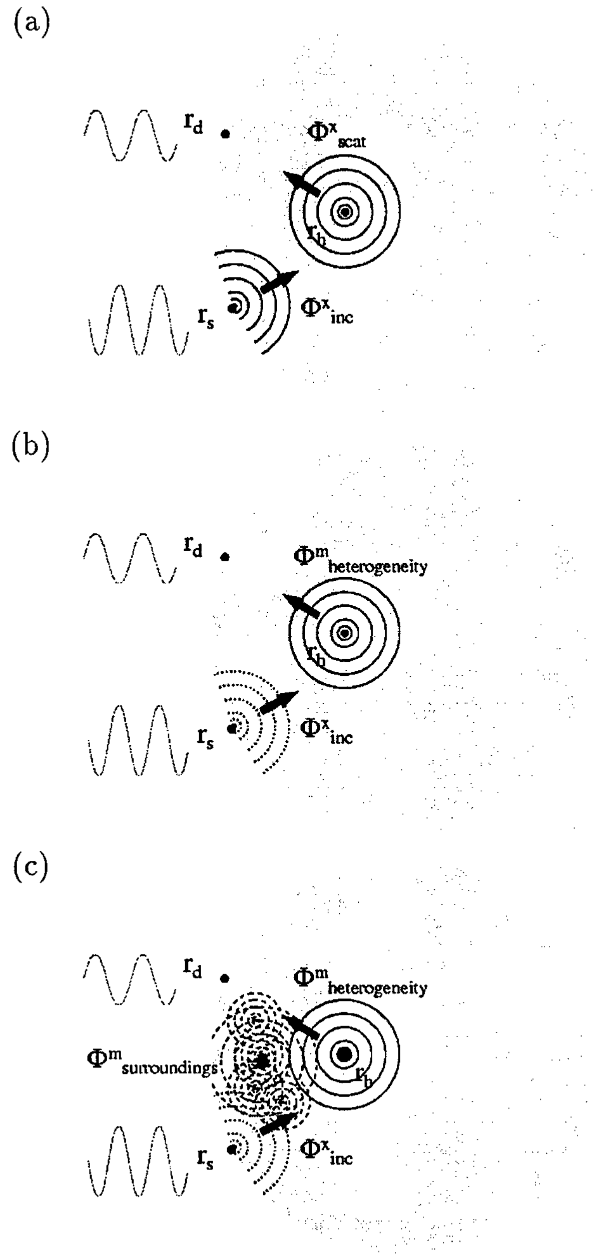
(a)
rd
Φx scat
rb
rs
Φx inc
(b)
rd
Φm heterogeneity
rb
rs
Φx inc
(c)
rd
Φm heterogeneity
Φm surroundings
rb
rs
Φx inc

Figure 1.6. Schematic illustrating frequency domain photon migration measurements of a sinusoidally modulated excitation light source at position $\vec{r}_s$ and the detected excitation and emission (fluorescent) signals at position $\vec{r}_d$ when contrast is owing to (a) absorption, (b) perfect uptake of a fluorescent dye, and (c) imperfect uptake of fluorescent dye.

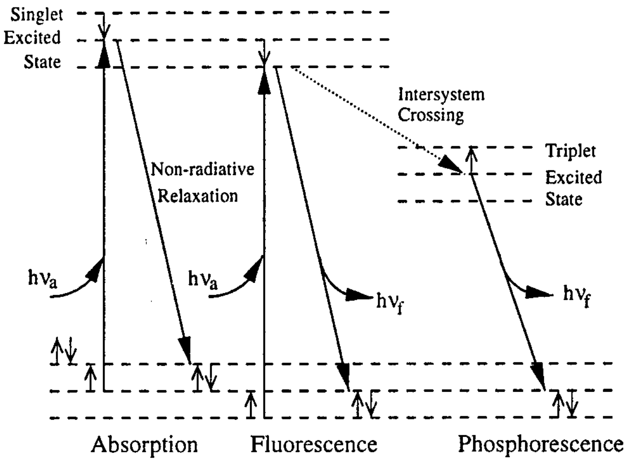
Singlet
Excited
State
Intersystem
Crossing
Triplet
Excited
State
Non-radiative
Relaxation
hν_a
hν_a
hν_f
hν_f
Absorption
Fluorescence
Phosphorescence

Figure 1.7. Jablonski diagram illustrating the electronic transitions associated with absorption, fluorescence and phosphorescence.

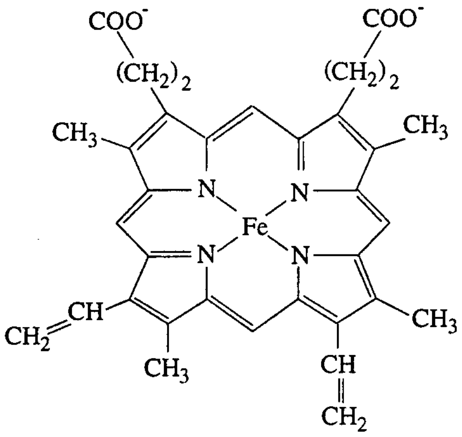

Figure 1.8. Molecular structure of heme showing the characteristic heterocyclic rings that are common to porphyrin compounds.

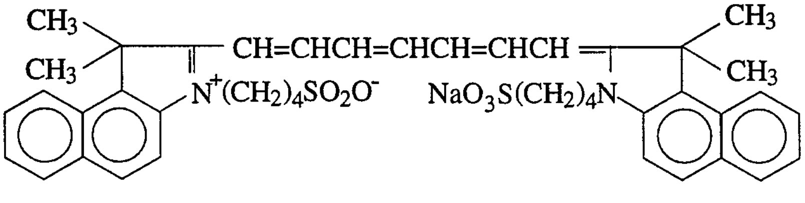

Figure 1.9. Molecular structure of Indocyanine Green (ICG).

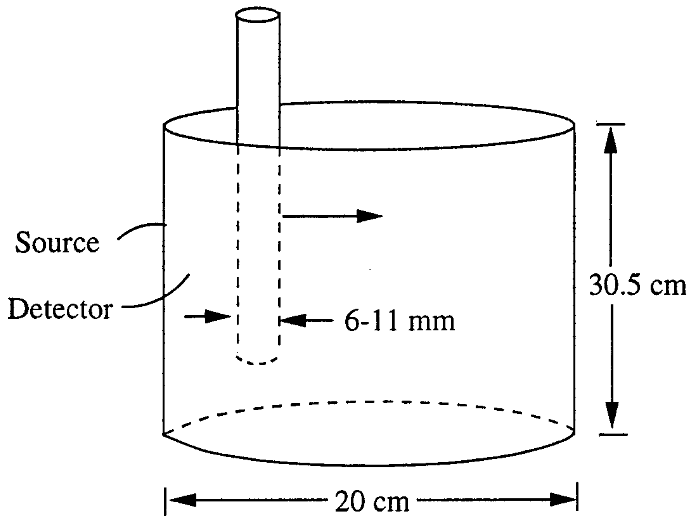
Source
Detector
6-11 mm
30.5 cm
20 cm

Figure 2.1. Schematic of the cylindrical tank used in the single pixel measurements of modulation phase and modulation ratio for absorbing and fluorescing heterogeneities.

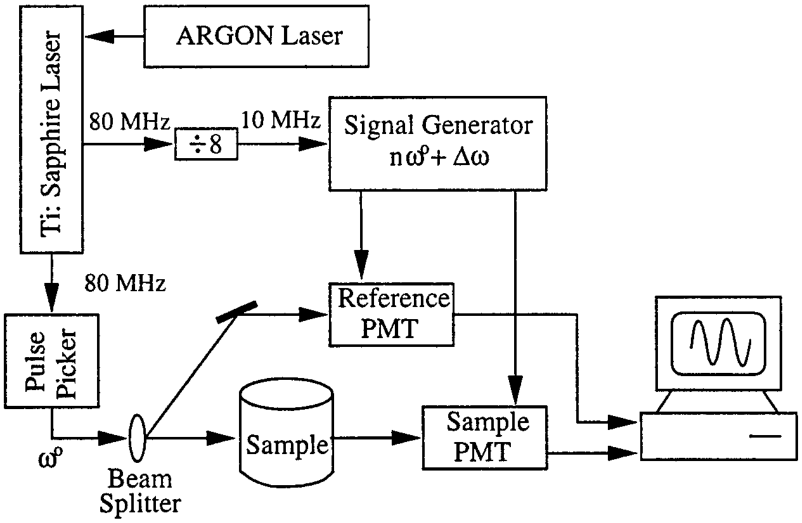
ARGON Laser
Ti: Sapphire Laser
80 MHz
÷8
10 MHz
Signal Generator
nω°+ Δω
80 MHz
Pulse Picker
Reference PMT
Sample
Sample PMT
ω°
Beam Splitter

Figure 2.2. Frequency domain system for single pixel measurements using a Ti:Sapphire laser as the light source.

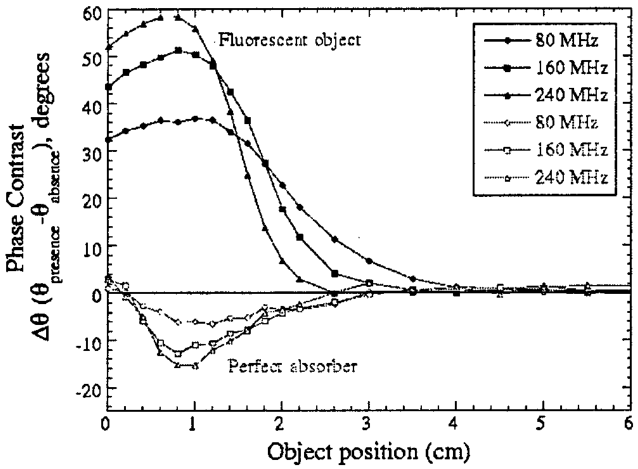

Figure 2.3. Phase contrast, $\Delta\theta(\theta_{presence} - \theta_{absence})$, as a function of object position for both a perfect absorbing object (open symbols) and a fluorescent object (closed symbols) measured at 80, 160 and 240 MHz.

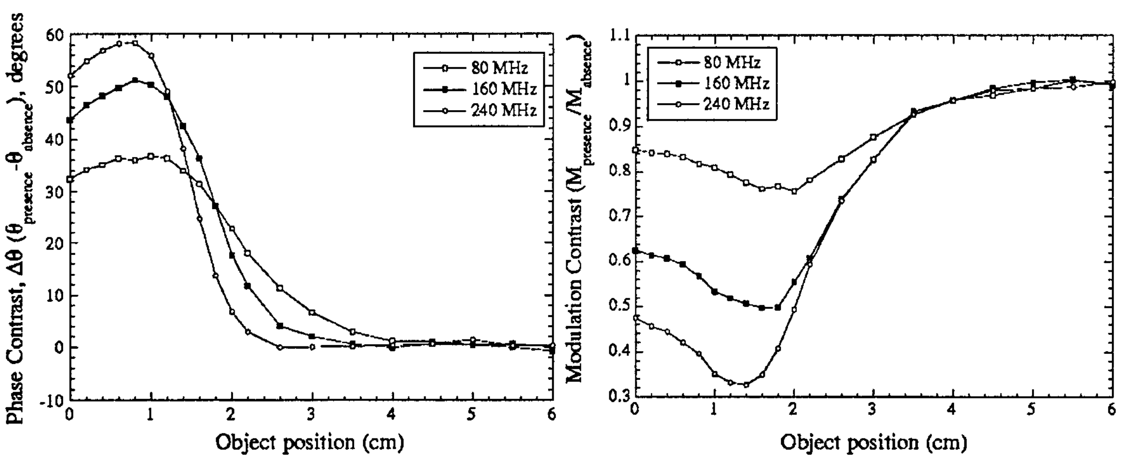

(a)

(b)

Figure 2.4. Experimental measurements of (a) phase contrast, $\Delta\theta$ $(\theta_{presence} - \theta_{absence})$, and (b) modulation contrast, ΔM $(M_{presence}/M_{absence})$, versus object position for a micromolar solution of DTTCI at modulation frequencies of 80, 160 and 240 MHz. A 9.5 mm diameter heterogeneity was used to hold the dye solution inside the 20 cm diameter tank.

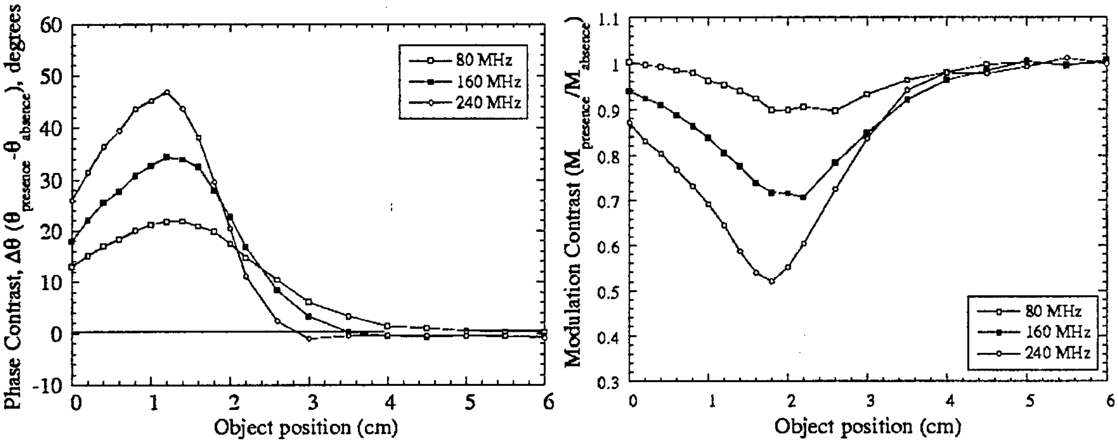

(a) (b)

Figure 2.5. Experimental measurements of (a) phase contrast, $\Delta\theta$ $(\theta_{presence} - \theta_{absence})$, and (b) modulation contrast, ΔM $(M_{presence}/M_{absence})$, versus object position for a micromolar solution of ICG at modulation frequencies of 80, 160 and 240 MHz. A 9.5 mm diameter heterogeneity was used to hold the dye solution inside the 20 cm diameter tank.

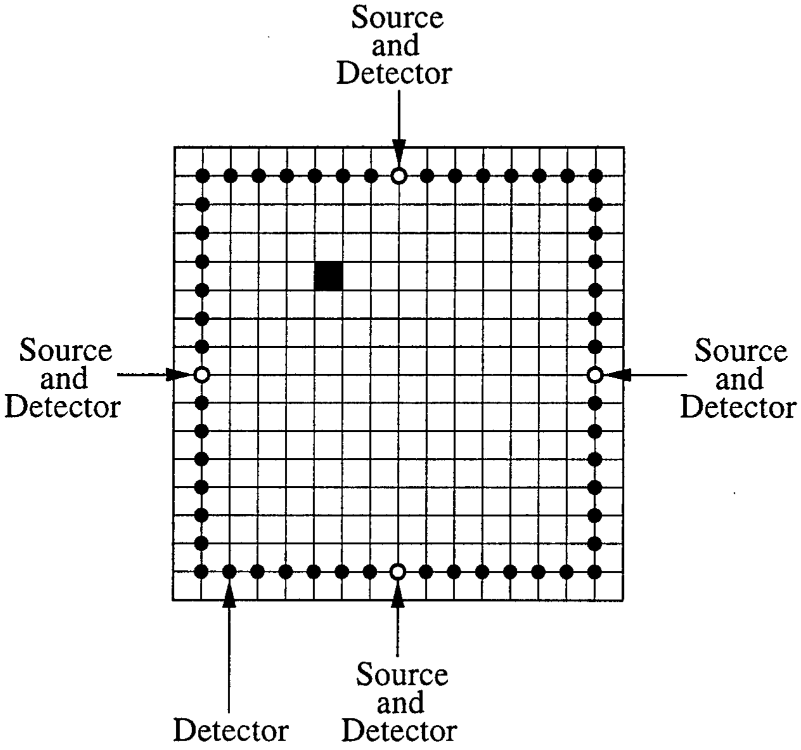
Source and Detector
Source and Detector
Source and Detector
Detector
Source and Detector

Figure 3.1. Schematic of the two–dimensional simulated tissue phantom showing the location of the 4 sources and 56 detectors around the perimeter for the 17 × 17 mesh on a 16 cm^2 area. The small square object inside the phantom represents a simulated diseased tissue volume.

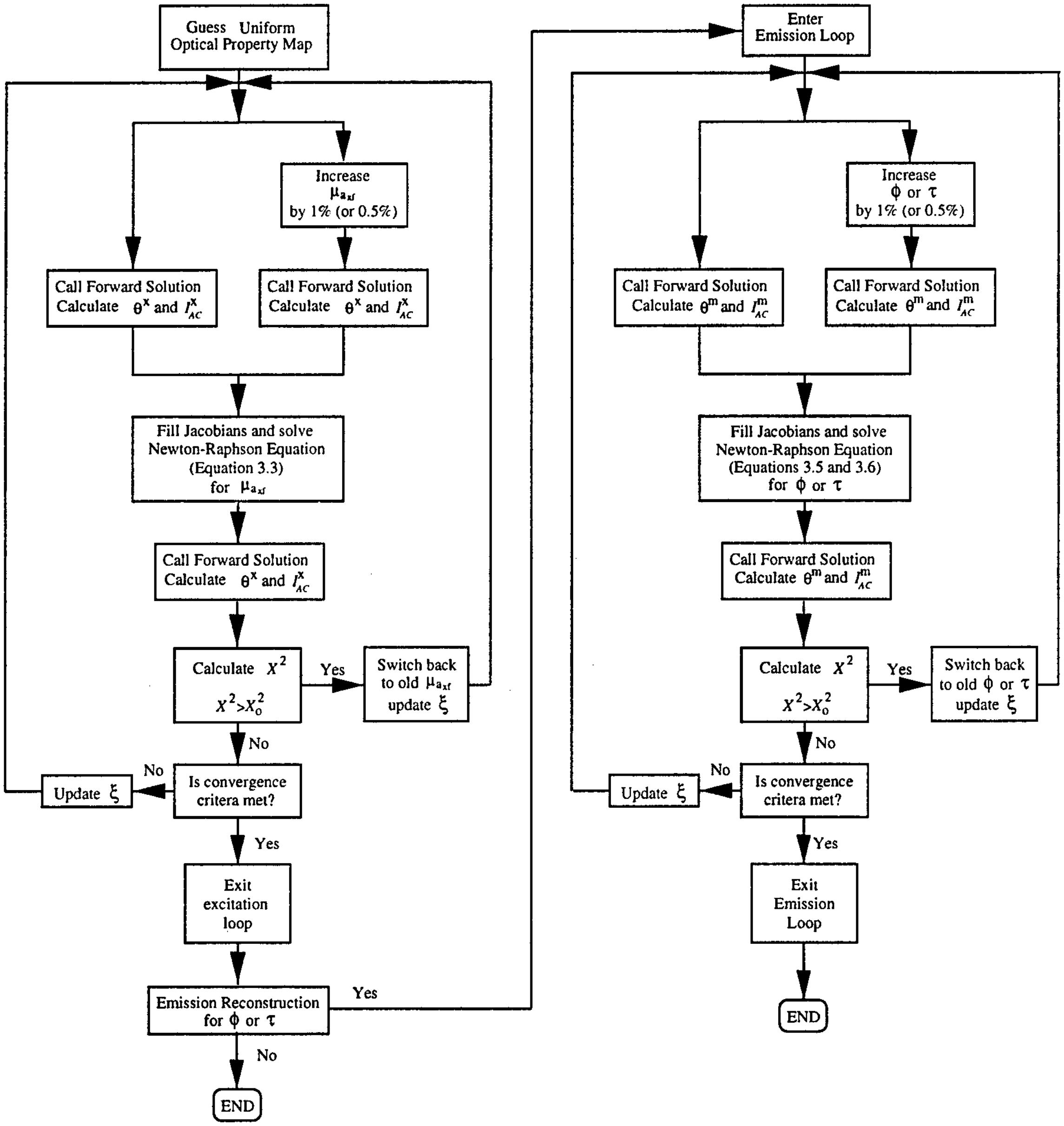
Guess Uniform Optical Property Map
Increase $\mu_{a_{xf}}$ by 1% (or 0.5%)
Call Forward Solution Calculate θ^x and I^x_{AC}
Call Forward Solution Calculate θ^x and I^x_{AC}
Fill Jacobians and solve Newton-Raphson Equation (Equation 3.3) for $\mu_{a_{xf}}$
Call Forward Solution Calculate θ^x and I^x_{AC}
Calculate X^2 $X^2>X^2_o$
Yes
Switch back to old $\mu_{a_{xf}}$ update ξ
No
Update ξ
No
Is convergence critera met?
Yes
Exit excitation loop
Emission Reconstruction for ϕ or τ
Yes
No
END
Enter Emission Loop
Increase ϕ or τ by 1% (or 0.5%)
Call Forward Solution Calculate θ^m and I^m_{AC}
Call Forward Solution Calculate θ^m and I^m_{AC}
Fill Jacobians and solve Newton-Raphson Equation (Equations 3.5 and 3.6) for ϕ or τ
Call Forward Solution Calculate θ^m and I^m_{AC}
Calculate X^2 $X^2>X^2_o$
Yes
Switch back to old ϕ or τ update ξ
No
Update ξ
No
Is convergence critera met?
Yes
Exit Emission Loop
END

Figure 3.2. Flow diagram of the reconstruction algorithm. The excitation loop reconstructs $\mu_{a_{xf}}$ and the emission loop either reconstructs ϕ or τ.

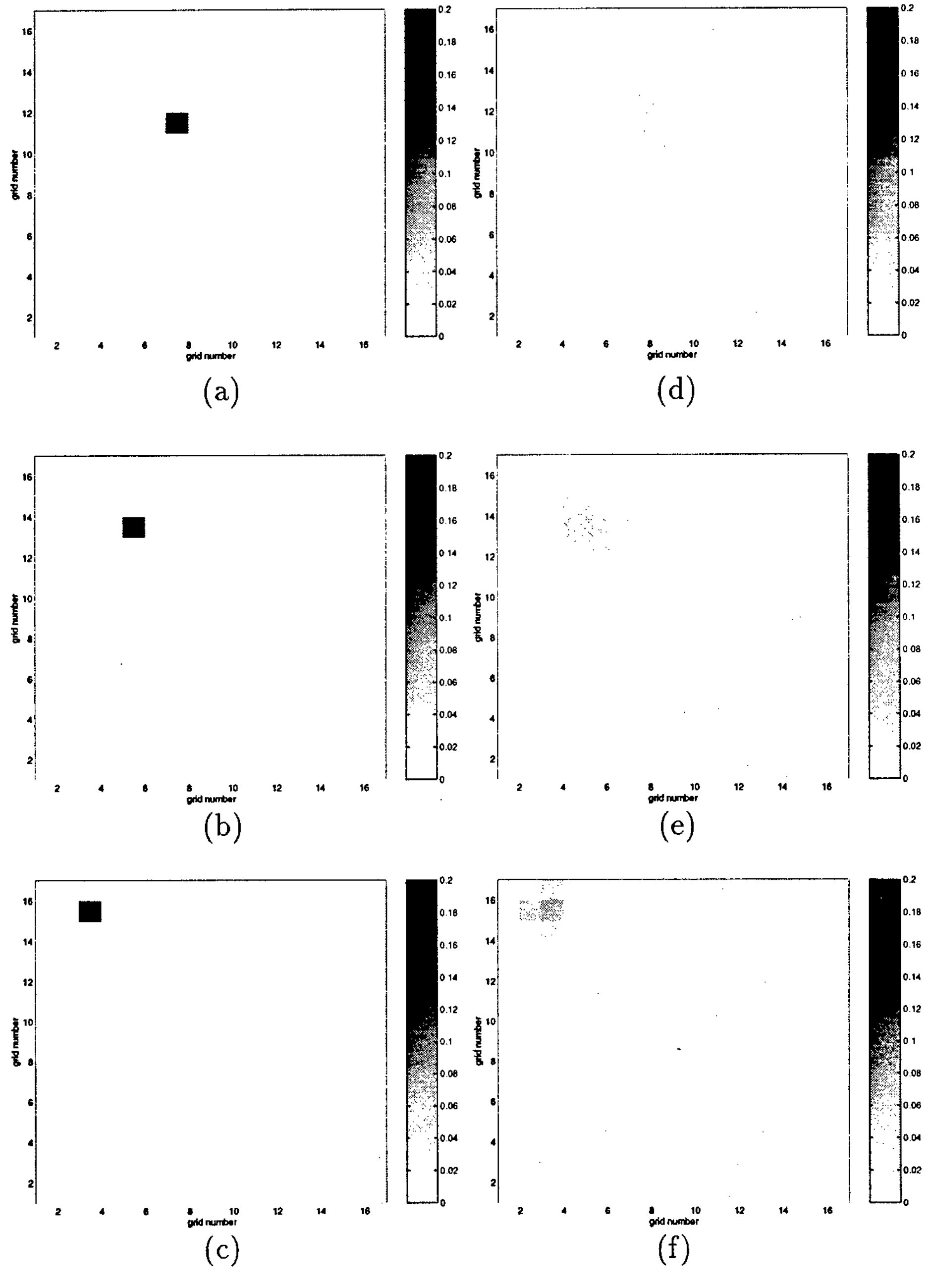

(a) (d)

(b) (e)

(c) (f)

Figure 4.1. Reconstructed spatial maps of an absorbing heterogeneity as a function of position for a 20:1 uptake ratio of dye inside the object. Figures (a), (b) and (c) are actual spatial maps and Figures (d), (e) and (f) are their corresponding reconstructions. The actual values of $\mu_{a_{xf}}$ in the object and the surroundings are 0.200 cm^{-1} and 0.010 cm^{-1} respectively.

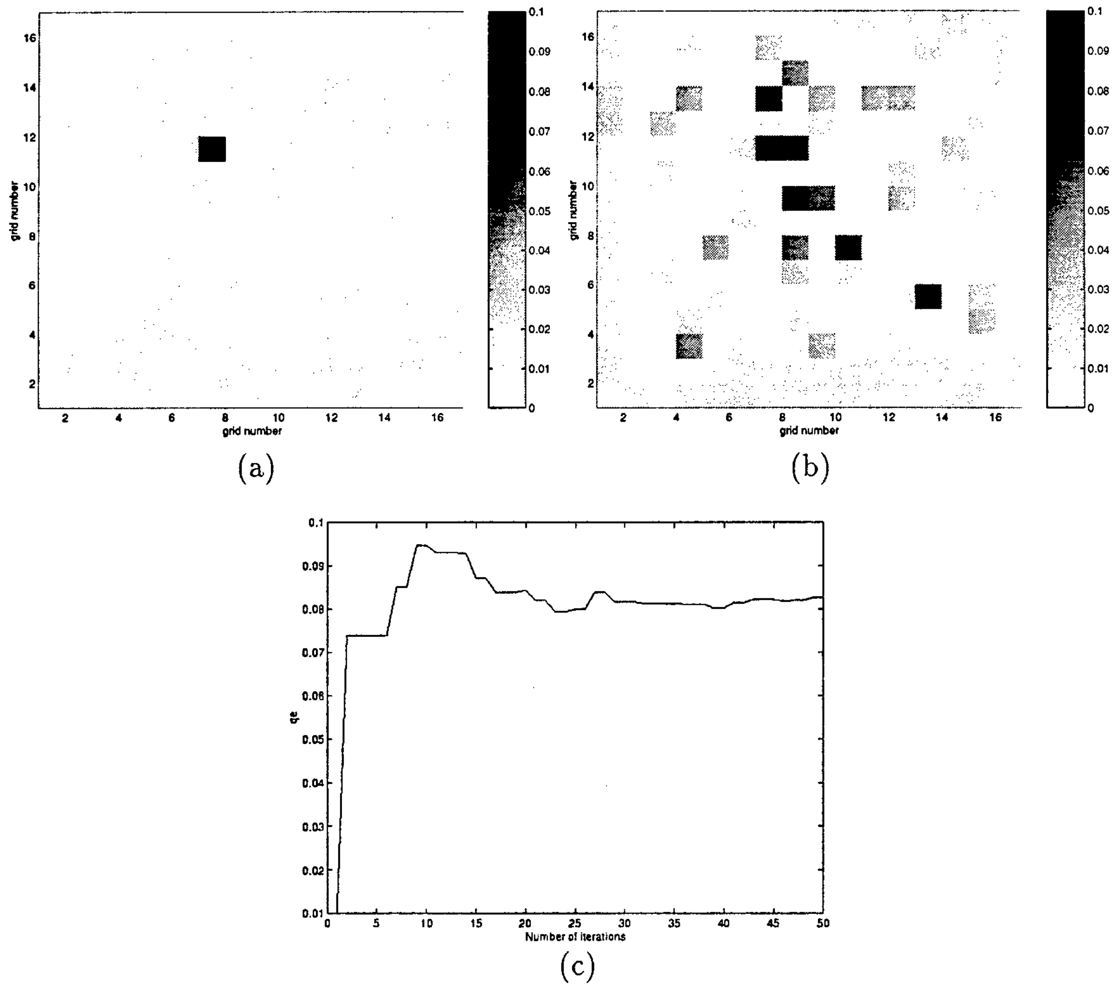

(a) (b)

(c)

Figure 4.2. Reconstructed spatial map of fluorescent quantum efficiency, ϕ, for a 10:1 uptake of dye inside the heterogeneity. Figure (a) represents the actual image, (b) shows the corresponding reconstruction and (c) shows the value of ϕ inside the object as a function of iteration number. The actual values of ϕ in the object and the surroundings were 0.100 cm^{-1} and 0.010 cm^{-1}, respectively, and the reconstructions yielded values of 0.082 cm^{-1} and 0.012 cm^{-1}, respectively.

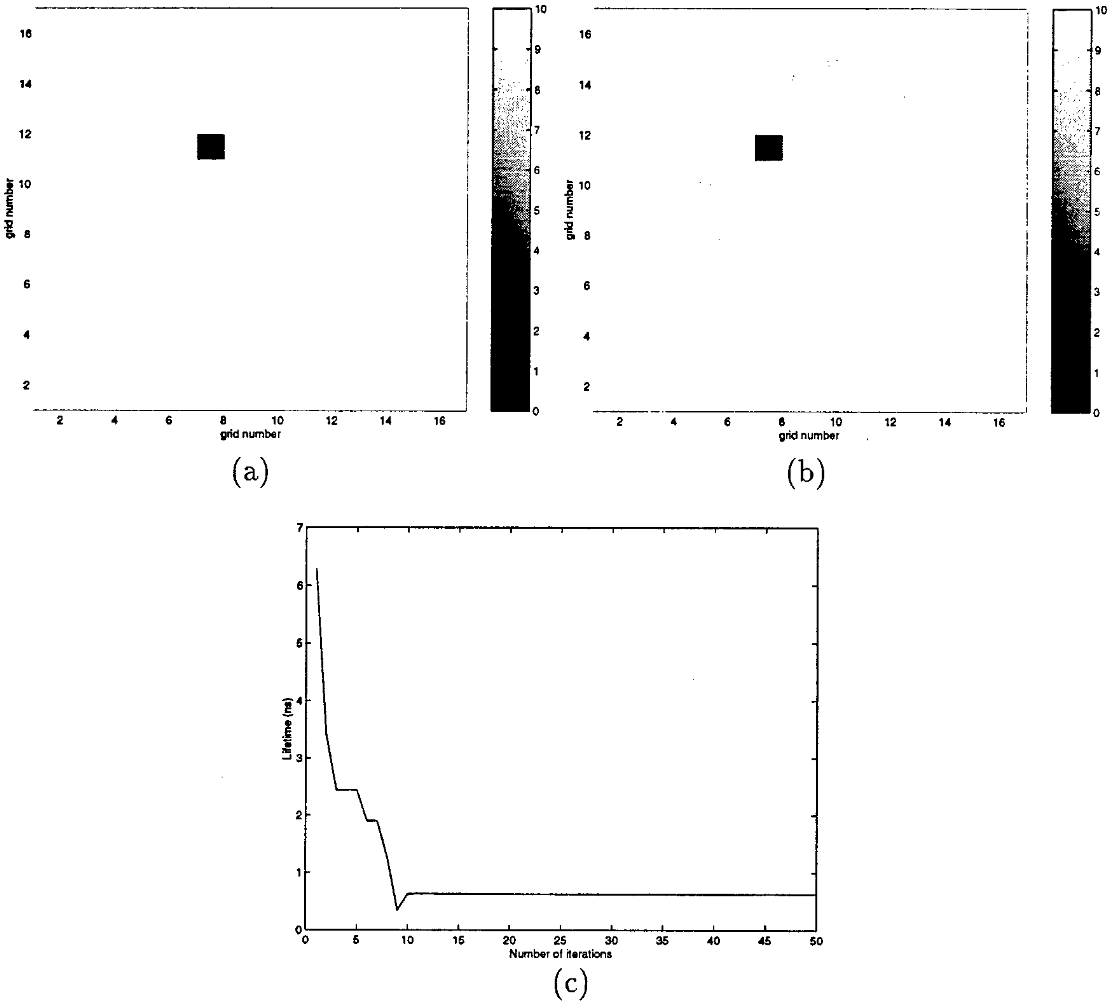

(a)

(b)

(c)

Figure 4.3. Reconstructed spatial map of fluorescent lifetime, τ, for a 10:1 uptake of dye inside the heterogeneity. Figure (a) shows the actual image, (b) is the corresponding reconstruction and (c) depicts the convergence of τ in the object as a function of iteration number. The actual lifetimes for the object and background are 1 and 10 ns respectively. The reconstruction converges correctly to 1 ns in the object. The background converges to 10.067 ns which is 0.67% larger than the actual value of 10 ns.

Table 4.1 Optical properties and experimental parameters used as inputs for the forward problem along with values of $\mu_{a_{xf}}$ obtained from the reconstructions for three different object locations.

	actual				reconstructed		
	background		object		background	object	
case	$\mu_{a_{xi}}$, $\mu_{a_{xf}}$ (cm^{-1})	μ_{s_x} (cm^{-1})	$\mu_{a_{xf}}$ (cm^{-1})	position	$\mu_{a_{xf}}$ (cm^{-1})	$\mu_{a_{xf}}$ (cm^{-1})	position
a	0.010	10.0	0.200	(11,7)	0.011	0.034	(11,7)
b	0.010	10.0	0.200	(13,5)	0.011	0.042	(13,5)
c	0.010	10.0	0.200	(15,3)	0.010	0.068	(15,3)

Table 4.2 Optical properties and experimental parameters used as inputs for the forward problem along with values of ϕ obtained from the reconstructions.

actual								reconstructed	
background						object		background	object
$\mu_{a_{xi}}$, $\mu_{a_{mi}}$ (cm^{-1})	$\mu_{a_{xf}}$ (cm^{-1})	μ_{s_x}, μ_{s_m} (cm^{-1})	$\mu_{a_{mi}}$ (cm^{-1})	τ (ns)	ϕ	$\mu_{a_{xf}}$ (cm^{-1})	ϕ	ϕ	ϕ
0.000	0.020	10.0	0.002	1.00	0.010	0.200	0.100	0.012	0.082

Table 4.3 Optical properties and experimental parameters used as inputs for the forward problem along with values of lifetime obtained from the reconstructions.

actual								reconstructed	
background						object		background	object
$\mu_{a_{xi}}$, $\mu_{a_{mi}}$ (cm^{-1})	$\mu_{a_{xf}}$ (cm^{-1})	μ_{s_x}, μ_{s_m} (cm^{-1})	$\mu_{a_{mi}}$ (cm^{-1})	ϕ	τ (ns)	$\mu_{a_{xf}}$ (cm^{-1})	τ (ns)	τ (ns)	τ (ns)
0.000	0.020	10.0	0.002	0.034	10.0	0.200	0.100	10.1	0.996

LIST OF REFERENCES

[1] S. Mordon, J. M. Devoisselle, and V. Maunoury, "In vivo pH measurements and imaging of tumor tissue using pH sensitive fluorescent probe (5,6-carboxyfluorescein): instrumental and experimental studies," Photochem. Photobiol. **60**, 274–279 (1994).

[2] D. A. Russell, R. H. Pottier, and D. P. Valenzeno, "Continuous, noninvasive measurement of *in vivo* pH in conscious mice," Photochem. Photobiol. **59**, 309–313 (1994).

[3] S. A. Vinogradov, L. W. Lo, W. T. Jenkins, S. M. Evans, C. Koch, and D. F. Wilson, "Noninvasive imaging of the distribution in oxygen in tissue in vivo using near-infrared phosphors," Biophys. J. **70**, 1609–1617 (1996).

[4] E. Sevick-Muraca, G. Lopez, J. Reynolds, T. Troy, and C. Hutchinson, "Fluorescence and absorption contrast mechanisms for biomedical optical imaging using frequency-domain techniques," J. Photochem. Photobiol. **66**, 55–64 (1997).

[5] R. Cubeddu, G. Canti, P. Taroni, and G. Valentini, "Time-gated fluorescence imaging for the diagnosis of tumors in murine model," Photochemistry and Photobiology **57**, 480–485 (1993).

[6] R. Cubeddu, G. Canti, A. Pifferi, P. Taroni, and G. Valentini, "Fluorescence lifetime imaging of experimental tumors in hematoporphyrin derivative sensitized mice," Photochemistry and Photobiology **66**, 229–236 (1997).

[7] H. W. Lim and N. A. Soter, *Clinical Photomedicine* (Marcel Dekker, New York, 1993).

[8] R. C. Haskell, L. O. Svaasand, T.-T. Tsay, T. Feng, M. S. McAdams, and B. J. Tromberg, "Boundary conditions for the diffusion equation in radiative transfer," J. Opt. Soc. Am. A **11**, 2727–2741 (1994).

[9] B. Beauvoit, S. M. Evans, T. W. Jenkins, E. E. Miller, and B. Chance, "Correlation between the light scattering and the mitochondrial content of normal tissues and transplantable rodent tumors," Analytical Biochemistry **226**, 167–174 (1995).

[10] B. Chance, H. Liu, T. Kitai, and Y. Zhang, "Effects of solutes on optical properties of biological materials: models, cells and tissues," Analytical Biochemistry **227,** 351–362 (1995).

[11] S. T. Flock, B. C. Wilson, and M. S. Patterson, "Hybrid Monte Carlo diffusion theory modeling of light distribution in tissue," Proc. SPIE **908,** 20–28 (1988).

[12] V. G. Peters, D. R. Wyman, M. S. Patterson, and G. L. Frank, "Optical properties of normal and diseased human breast tissues in the visible and near infrared," Phys. Med. Biol. **35,** 1317–1334 (1990).

[13] J. J. Duderstadt and L. J. Hamilton, *Nuclear Reactor Analysis* (Wiley, New York, New York, 1976).

[14] S. Chandrasekhar, *Radiative Transfer* (Dover, New York, New York, 1958).

[15] A. Ishimaru, *Wave propagation and scattering in random media* (Academic Press, New York, New York, 1973), Vol. 1.

[16] M. S. Patterson, B. Chance, and B. Wilson, "Time resolved reflectance and transmittance for the noninvasive measurement of tissue optical properties," Appl. Opt. **28,** 2331–2336 (1989).

[17] J. Reynolds, A. Przadka, S. Yeung, and K. Webb, "Optical diffusion imaging: a comparative numerical and experimental study," Appl. Opt. **35,** 3671–3679 (1996).

[18] M. O'Leary, D. Boas, B. Chance, and A. Yodh, "Refraction of diffuse photon density waves," Physical Review Letters **69,** 2658–2661 (1992).

[19] J. Lakowicz, *Principles of Fluorescence Spectroscopy* (Plenum Press, New York, 1983).

[20] E. M. Sevick and C. L. Burch, "Origin of phosphorescence signals reemitted from tissues," Opt. Lett. **19,** 1928–1930 (1994).

[21] E. M. Sevick-Muraca and C. Hutchinson, "Probability description of fluorescent and phosphorescent signal generation in tissues and other random media," SPIE **2387,** 274–283 (1995).

[22] G. Batchteler, K. H. Drexhage, J. Arden-Jacob, K. T. Han, M. Kollner, R. Muller, M. Sauer, S. Seeger, and J. Wolfrum, "Sensitive fluorescence using laser diodes and multiplex dyes," J. Luminescence **60,** 511–514 (1994).

[23] M. S. Patterson and B. W. Pogue, "Mathematical model for time-resolved and frequency-domain fluorescence spectroscopy in biological tissues," Appl. Opt. **33,** 1963–1974 (1994).

[24] C. L. Hutchinson, J. R. Lakowicz, and E. M. Sevick-Muraca, "Fluorescence lifetime based sensing in tissues: A computational study," Biophys. J. **68,** 1574–1582 (1995).

[25] B. C. Wilson and M. S. Patterson, "The physics of photodynamic therapy," Phys. Med. Biol. **31,** 327–360 (1986).

[26] W. W. Lee, D. Wilson, and L. Singerman, "Correction of spatial distortion and registration in ophthalmic fluorescein angiography," IEEE **16,** 508–509 (1994).

[27] S. A. May, "Photonic approaches to burn diagnostics," Biophotonics International pp. 44–50 (1994).

[28] H. J. van Staveren, C. J. M. Moes, J. van Marie, S. A. Prahl, and M. J. C. van Gemert, "Light scattering in Intralipid-10% in the wavelength range of 400-1100 nm," Appl. Opt. **30,** 4507–4514 (1991).

[29] A. Yariv, *Introduction to Optical Electronics*, 3rd ed. (Holt-Saunders International Editions, New York, 1985).

[30] G. Lopez, *Absorption and fluorescent contrast mechanisms for the detection and diagnosis of breast cancer using single pixel frequency-domain photon migration techniques* (masters thesis, Purdue University, West Lafayette, IN, 1997).

[31] J. S. Reynolds, T. Troy, and E. M. Sevick-Muraca, "Multi-pixel techniques for frequency-domain photon migration imaging," Biotechnology Progress **13,** 669–680 (1997).

[32] M. O'Leary, D. Boas, B. Chance, and A. Yodh, "Reradiation and imaging of diffuse photon density waves using fluorescent inhomogeneities," J. Lumin. **60** & **61,** 281–286 (1994).

[33] D. A. Boas, M. A. O'Leary, B. Chance, and A. G. Yodh, "Scattering of diffuse photon density waves by spherical inhomogeneities with turbid media: analytic solution and applications," Proc. Natl. Acad. Sci. USA **91,** 4887–91 (1994).

[34] M. O'Leary, D. Boas, B. Chance, and A. Yodh, "Experimental images of heterogeneous turbid media by frequency-domain diffusion-photon tomography," Optics Letters **20,** 426–428 (1995).

[35] Y. Yao, Y. Wang, Y. Pei, W. Zhu, and R. L. Barbour, "Frequency-domain optical imaging of absorption and scattering distributions by a Born iterative method," J. Opt. Soc. Am. A. **14,** 325–342 (1997).

[36] S. R. Arridge, M. Schweiger, M. Hiraoka, and D. T. Delpy, "Performance of an iterative reconstruction algorithm for near infrared absorption and scatter imaging," SPIE **1888,** 360–371 (1993).

[37] B. W. Pogue, M. S. Patterson, H. Jiang, and K. D. Paulsen, "Initial assessment of a simple system for frequency domain diffuse optical tomography," Phys. Med. Biol. **40,** 1709–1729 (1995).

[38] H. Jiang, K. D. Paulsen, U. L. Osterberg, B. W. Pogue, and M. S. Patterson, "Simultaneous reconstruction of absorption and scattering maps in turbid media from near-infrared frequency-domain data," Opt. Lett. **20,** 2128–2130 (1995).

[39] H. Jiang, K. D. Paulsen, U. L. Osterberg, B. W. Pogue, and M. S. Patterson, "Optical image reconstruction using frequency domain data: simulations and experiments," J. Opt. Soc. Am. A. **13,** 253–266 (1996).

[40] D. Y. Paithankar, A. U. Chen, B. W. Pogue, M. S. Patterson, and E. M. Sevick-Muraca, "Imaging of fluorescent yield and lifetime from multiply scattered light reemitted from random media," Appl. Opt. **36,** 2260–2272 (1997).

[41] T. J. Yorkey, J. G. Webster, and W. J. Tompkins, "Comparing reconstruction algorithms for electrical impedance tomography," IEEE Trans. Biomed. Eng. **BME-34,** 843–852 (1987).

[42] *Photodynamic Therapy basic principles and clinical application*, B. W. Henderson and T. J. Dougherty, eds., (Marcel Dekker, Inc., 1992).

[43] S. L. Marcus, "Photodynamic Therapy of Human Cancer," IEEE **80,** 869–889 (1992).

[44] T. L. Troy, *Biomedical Optical Imaging with Frequency Domain Photon Migration Measurements: Experiments and Numerical Image Reconstructions* (PhD. thesis, Purdue University, West Lafayette, IN, 1997).

[45] C. L. Burch, *Monte Carlo simulations of photon migration in highly scattering media* (masters thesis, Vanderbilt University, Nashville, TN, 1993).

Role of higher-order scattering in solutions to the forward and inverse optical-imaging problems in random media

E. M. Sevick-Muraca, D. L. Heintzelman, J. Lee, T. L. Troy, and D. Y. Paithankar

From analytical and numerical solutions that predict the scattering of diffuse photon density waves and from experimental measurements of changes in phase shift θ and ac amplitude demodulation *M* caused by the presence of single and double cylindrical heterogeneities, we show that second- and higher-order perturbations can affect the prediction of the propagation characteristics of diffuse photon density waves. Our experimental results for perfect absorbers in a lossless medium suggest that the performance of fast inverse-imaging algorithms that use first-order Born or Rytov approximations might have inherent limitations compared with inverse solutions that use iterative solutions of a linear perturbation equation or numerical solutions of the diffusion equation. © 1997 Optical Society of America

Key words: Photon migration imaging, image reconstruction, frequency-domain, inverse problem, biomedical optical imaging.

1. Introduction

With the development of near-infrared (NIR)-emitting laser diodes and the realization that NIR light can travel several centimeters through tissue, numerous groups have embarked upon development of optical imaging as a new medical imaging modality. Although approaches such as monitoring the vanishingly small component of coherent light with sophisticated techniques of Kerr filtering,[1] time gating,[2] and conservation of light polarization[3] vary, other approaches focus on monitoring the predominant optical signal re-emitted from tissues: the multiply scattered signal. Continuous wave,[4] time domain,[5] and frequency domain[6–8] measurements of multiply scattered light have been performed in simulated and experimental tissue phantom studies as well as in human studies.[9] However, the use of these measurements for reconstructing maps of internal tissue optical properties for diagnostic imaging has been problematic because the geometric correlation between incident and detected radiation is destroyed by multiple scattering.

While some investigators have used direct image reconstruction approaches that use measured optical data to directly form an image,[9–11] others have sought full solution to the inverse-imaging problem, which relates external time-dependent measurements made at the periphery to an optical property map of interior volumes through the optical diffusion equation.[6–8,12–16] Two approaches for solving the inverse solution have been adopted. In the first approach, the fluence associated with a propagating photon density wave launched at source position ρ_s and detected at the tissue periphery at position ρ_d [denoted $\Phi(\rho_s, \rho_d)$] is related to the fluence assumed in the absence of any optical heterogeneities [denoted $\Phi_{\text{inc}}(\rho_s, \rho_d)$] and the internal optical property perturbation map $\Delta(\rho)$ through a Fredholm integral equation of the first kind:

$$\Phi(\rho_s, \rho_d) = \Phi_{\text{inc}}(\rho_s, \rho_d) + \int G(\rho, \rho_d)\Phi_0(\rho_s, \rho)\Delta(\rho)\partial^3\rho, \quad (1)$$

where $G(\rho, \rho_d)$ is the Green's function to the diffusion equation,

$$G(\rho, \rho_D) = \frac{1}{4\pi(\rho - \rho_D)} \exp\{i[(-\mu_a + i\omega/c_n)/D]^{1/2}(\rho - \rho_D)\},$$

describing the propagation of light from position ρ to the detector at ρ_d, and Φ_0 is the incident wave impinging at position ρ. If one assumes that the incident wave impinging upon the position ρ can be

---

The authors are with the School of Chemical Engineering, Purdue University, West Lafeyette, Indiana 47907.

Received 22 May 1997.
0003-6935/97/349058-10$10.00/0
© 1997 Optical Society of America

approximated by the fluence predicted in the absence of heterogeneities (i.e., $\Phi_0 \rightarrow \Phi_{\text{inc}}$, known as the Born approximation), upon measurement of fluence at a variety of source–detector separations and upon discretization of Eq. (1), an optical map of perturbations $\Delta(\rho)$ can be obtained to a first-order approximation.[15] However, the Born approximation $\Phi_0 \rightarrow \Phi_{\text{inc}}$ does not account for second- and higher-order effects that might arise from the rescattering of photon density waves associated with neighboring inhomogeneities. In addition, this approach assumes that perturbations in optical properties at a position ρ_j do not influence the propagation of light from position ρ_{j+1} to detector ρ_d as described by the Green's function $G(\rho, \rho_d)$.

Investigators use the Born iterative method (BIM) to account for strong perturbations and for second- and higher-order scattering effects by using the first-order approximation of optical property perturbations $\Delta(\rho)$ to iteratively calculate Φ_0 or the fluence incident at position ρ. Yao *et al.*[16] have shown that the BIM tends to compensate for the underprediction of the scattering and absorption properties of a single heterogeneity in an otherwise uniform medium that would occur when the Born approximation (or single iteration) is used. In addition to the BIM, the distorted Born iterative method (DBIM) represents a refinement in that it also recompiles the Green's functions $G(\rho, \rho_d)$ to reflect changes in light propagation and it should speed convergence. Yet to date there has been no investigation that addresses how these iterative reconstruction algorithms affect the resolution or, more precisely, how these linear perturbation approaches can be used to accurately image closely positioned, multiple heterogeneities between which nonlinear second- and higher-order scattering effects exist.

In contrast with this inversion approach, Jiang *et al.*[7,8] and Arridge *et al.*[14] have used full numerical solution to the diffusion equation that describes the interdependence of voxel optical properties and their contribution to the re-emitted optical signal detected from cw and frequency domain measurements. With this approach, the second- and higher-order scattering arising from multiple inhomogeneities, which are not accounted for in the first iterations of Born and Rytov approximations, are incorporated in the forward and inverse solutions. The inversion consists of the relating of spatial changes of optical properties on detected frequency domain measurements through numerical solution of the diffusion equation and then solving an update to the map of optical properties from the difference between the signals that are measured and those that are predicted by the forward solution to the diffusion equation. Note that convergence on the optical properties is achieved with these numerical approaches and not with the iterative Born and Rytov approaches. Nonetheless, while the computational investment of iterative but analytically based inversions is less than that of full numerical solution of the diffusion equation, the relative performance of these two inverse-solution approaches has yet to be evaluated.

For this reason we embarked on a study to assess the contributions of neighboring heterogeneities by using experimental, numerical, and analytical computations of scattered photon density waves from perfect light-absorbing cylinders. Specifically we experimentally and computationally monitor the multiple scattering of photon density waves between two neighboring perfect cylindrical absorbers embedded in a tissue-mimicking scattering medium to assess the higher-order perturbation effects on a re-emitted, detected photon density wave. In the following we briefly review the theory of higher-order perturbation effects as predicted from the experimental frequency domain measurements as well as from the Helmholtz equations. In addition, we present experimental measurements and numerical solutions of the optical diffusion equation that show the errors, which can be significant, introduced by neglecting second-order effects. These errors can define the limits of resolution for two perfect absorbers in the inverse-solution approaches that do not use BIM, DBIM, or the full numerical solution of the optical diffusion equation. We comment on these effects when contrast is caused by mechanisms other than a perfect absorber.

2. Theoretical Background for Perturbations Associated with Diffuse Photon Density Waves

Our work to assess the contributions of higher-order perturbations has been motivated by the work of Boas *et al.*[15] Their approach for image reconstruction from diffusely propagating photon density waves uses analytical expressions to describe the complex fluence of a propagating photon density wave $\Phi(\rho)$ in the presence of m heterogeneities by superposition of incident $\Phi_{\text{inc}}(\rho)$ and scattered $\Phi_{\text{scat},k}{}^{n}(\rho)$ waves, from body k and of the order of n:

$$\Phi(\rho) = \Phi_{\text{inc}}(\rho) + \sum_{n=1}^{\infty} \sum_{k=1}^{m} \Phi_{\text{scat},k}{}^{n}(\rho). \tag{2}$$

The second-order effects caused by the scattering of a photon density wave between two objects are illustrated in Fig. 1, from the work of Boas and co-workers, and delineate the contribution of these effects to the detected photon density wave $\Phi(\rho)$. Second- and higher-order-scattering effects arise from the rescattering of an incident wave between the two bodies. Boas *et al.* assume that second-order-scattering effects (denoted by the dotted line in Fig. 1) are negligible under most circumstances. We explore this assumption, using experimental, numerical, and analytical predictions of second-order contributions.

A. Analysis of Experimental Measurements of Photon Density Waves

To measure second-order contributions we experimentally measured the detected photon density wave in the presence of one light-absorbing object alone, Φ_{k1}; object two alone, Φ_{k2}; and with both objects present, $\Phi_{k1,k2}$, as a function of object positions ρ_1 and

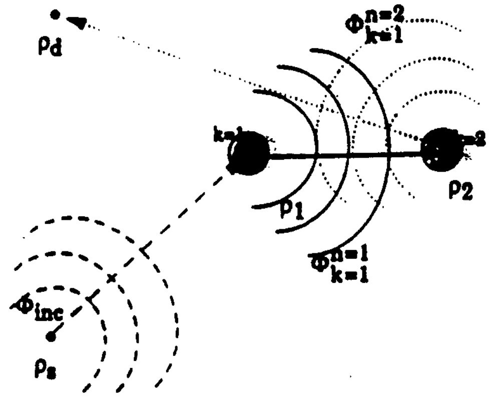

Fig. 1. Schematic illustrating the incident wave Φ_{inc} originating from the source at position ρ_s (dashed lines); the first-order scattered wave $\Phi_{scat,k1}{}^{n=1}$ arising from the first heterogeneity (solid lines); and the second-order wave $\Phi_{scat,k2}{}^{n=2}$ arising from rescatter of the first-order wave off the second heterogeneity (dotted lines).

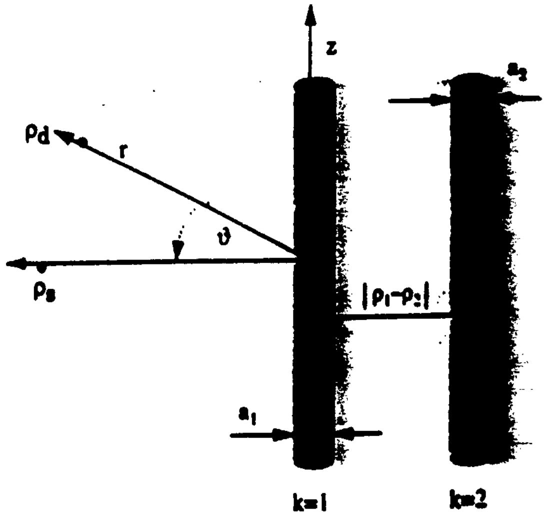

Fig. 2. Schematic detailing the geometry used in the calculation of scattered waves from analytical expression. The centroid of the cylinder is the origin, with z denoting the length, angle ϑ denoting the angle in the plane containing the source and the detector, and r denoting the radial direction.

ρ_2 and separation between the two objects $\rho_1-\rho_2$ (see Fig. 2). From Eq. (2), expressions can be written for measurements of Φ_{k1} and Φ_{k2} made at detector position ρ_d in the presence of single objects:

$$\Phi_{k1}(\rho_d) = \Phi_{inc}(\rho_d) + \Phi_{scat,k1}{}^{n=1}(\rho_d), \tag{3}$$

$$\Phi_{k2}(\rho_d) = \Phi_{inc}(\rho_d) + \Phi_{scat,k2}{}^{n=1}(\rho_d), \tag{4}$$

where $k1$ denotes the presence of the first body alone and $k2$ denotes the presence of the second body. With simple algebraic manipulation of Eqs. (2)–(4), an expression accounting for higher-order-scattering effects can be written for the photon density wave in the presence of both objects $\Phi_{k1,k2}(\rho_d)$:

$$\begin{aligned}\Phi_{k1,k2}(\rho_d) = {} & \Phi_{k1}(\rho_d) + \Phi_{k2}(\rho_d) - \Phi_{inc}(\rho_d) \\ & + \Phi_{scat,k1,k2}{}^{n=2}(\rho_d) + \Phi_{scat,k1,k2}{}^{n=3}(\rho_d) + \ldots .\end{aligned} \tag{5}$$

For this study, it is assumed that third- and higher-order scattered waves are considered to have insignificant contributions to the measured fluence when compared with those of first- and second-order scattered waves.

From frequency domain measurements of phase shift θ and ac amplitude M, values of the complex fluence $\Phi = Me^{-i\theta}$ can be obtained (1) in the presence of the first object alone, $\Phi_{k1}(\rho_d)$; (2) in the presence of the second object alone, $\Phi_{k2}(\rho_d)$; (3) in the presence of both objects, $\Phi_{k1,k2}(\rho_d)$; and (4) in the absence of any inhomogeneities, $\Phi_{inc}(\rho_d)$. If second-order effects, i.e., $\Phi_{scat,k1,k2}{}^{n=2}(\rho_d)$, are negligible, from Eq. (5) it follows that measurements of $\Phi_{k1,k2}(\rho_d)$ should be predicted by measurements of $\Phi_{k1}(\rho_d)$, $\Phi_{k2}(\rho_d)$, and $\Phi_{inc}(\rho_d)$:

$$\Phi_{k1,k2}(\rho_d) = \Phi_{k=1}(\rho_d) + \Phi_{k=2}(\rho_d) - \Phi_{inc}(\rho_d). \tag{6}$$

Because we report our results in terms of phase shift and amplitude demodulation. Eq. (6) can be written as

$$\theta_{k1,k2}(\rho_d) = \tan^{-1}\left(\frac{M_{k1}\sin\theta_{k1} + M_{k2}\sin\theta_{k2} - M_{inc}\sin\theta_{inc}}{M_{k1}\cos\theta_{k1} + M_{k2}\cos\theta_{k2} - M_{inc}\cos\theta_{inc}}\right), \tag{7}$$

$$M_{k1,k2}(\rho_d) = [(M_{k1}\cos\theta_{k1} + M_{k2}\cos\theta_{k2} - M_{inc}\cos\theta_{inc})^2 + (M_{k1}\sin\theta_{k1} + M_{k2}\sin\theta_{k2} - M_{inc}\sin\theta_{inc})^2]^{1/2}. \tag{8}$$

B. Analytical Predictions of Phase Shift and Amplitude Modulation Owing to Two Perfect Absorbing Cylinders

The complex fluence describing the propagation of a photon density wave can also be computed analytically from the Helmholtz equations.[15,16] The complex fluence propagating from a source point at ρ_s through an infinite random medium and received at position ρ, in the absence of an optical heterogeneity, is given by

$$\Phi_{inc}(\rho) = S_{source}(\rho_s)\,\frac{\exp\left[i\left(\dfrac{-\mu_a + i\omega/c_n}{D}\right)^{1/2}(\rho-\rho_d)\right]}{4\pi D(\rho-\rho_d)}, \tag{9}$$

where S_{source} describes the phase and strength of modulation of the source located at position ρ_s; c_n is the speed of light in the medium; and D is the optical diffusion coefficient that is governed by the absorption μ_a and the isotropic scattering μ'_s, coefficients of the continuous or homogeneous medium:

$$D = 1/3(\mu_a + \mu_s'). \tag{10}$$

In this study, we approximate a point-modulated source at the periphery of a large cylinder as a point-modulated source located at the interface of a semi-infinite medium. In this case the fluence is written in cylindrical coordinates and at the surface ($z = 0$) given by[17]

$$\Phi_{\text{inc}}(\rho_d) = S_{\text{source}}(\rho_s)\,\frac{1}{4\pi D}$$
$$\times\left(\frac{\exp\left\{-\left(\frac{\mu_a + i\omega/c_n}{D}\right)^{1/2}[(\rho_s-\rho_d)^2+(z-z_0)^2]^{1/2}\right\}}{[(\rho_s-\rho_d)^2+(z-z_0)^2]^{1/2}} - \frac{\exp\left[-\left(\frac{\mu_a + i\omega/c_n}{D}\right)^{1/2}[(\rho_s-\rho_d)^2+(z+z_0)^2]^{1/2}\right]}{[(\rho_s-\rho_d)^2+(z+z_0)^2]^{1/2}}\right), \tag{11}$$

where z_0 is one isotropic scattering length ($1/\mu'_s$).

The first-order ($n = 1$) scattered wave from the $k1$ infinitely long cylinder in an infinite medium is given by[15,18]

$$\Phi_{\text{scat},k1}{}^{n=1}(\rho_d) = -\Phi_{\text{inc}} \sum_{m=1}^{\infty} \int_0^{\infty} \cos(m\vartheta)\cos(pz)$$
$$\times K_m\left\{\left[p^2 + \left(\frac{-\mu_a + i\omega/c_n}{D}\right)\right]^{1/2} \rho_d\right\}$$
$$\times K_m\left\{\left[p^2 + \left(\frac{-\mu_a + i\omega/c_n}{D}\right)\right]^{1/2} \rho_s\right\}$$
$$\times \left[\frac{DxI_m'(x)I_m(y) - D_{k1}'yI_m(x)I_m'(y)}{DxK_m'(x)I_m(y) - D_{k1}'yK_m(x)I_m'(y)}\right]\mathrm{d}p, \tag{12}$$

where D_k' is the optical diffusion coefficient within the cylinder k; I_m and K_m are modified Bessel functions; and parameters x and y are given as

$$x = \left[p^2 + \left(\frac{-\mu_a + i\omega/c_n}{D}\right)\right]^{1/2} a_k,$$
$$y = \left[p^2 + \left(\frac{-\mu_a' + i\omega/c_n}{D_k'}\right)\right]^{1/2} a_k;$$

and a_k is the radius of cylinder $k1$. Radius ρ_d, angle ϑ, and length z denote the coordinates of the detector relative to the center of the infinite cylinder $k1$ (Fig. 2). The incident wave upon the infinite cylinder Φ_{inc} is computed from Eq. (11). A similar expression can be written for $\Phi_{\text{scat},k2}{}^{n=1}$.

We calculated second-order-scattering contributions by evaluating the scattered wave originating from the second object ($k2$) as the incident wave upon the first object ($k1$). In other words,

$$\Phi_{\text{scat},k1}{}^{n=2}(\rho_d) = -\Phi_{\text{scat},k2}{}^{n=1} \sum_{m=1}^{\infty} \int_0^{\infty} \cos(m\vartheta)\cos(pz)$$
$$\times K_m\left\{\left[p^2 + \left(\frac{-\mu_a + iw/c_n}{D}\right)\right]^{1/2} \rho_d\right\}$$
$$\times K_m\left\{\left[p^2 + \left(\frac{-\mu_a + i\omega/c_n}{D}\right)\right]^{1/2} \rho_s\right\}$$
$$\times \left[\frac{DxI_m'(x)I_m(y) - D_{k1}'yI_m(x)I_m'(y)}{DxK_m'(x)I_m(y) - D_{k1}'yK_m(x)I_m'(y)}\right]\mathrm{d}p, \tag{13}$$

where the incident wave upon cylinder $k1$ is now the first-order scattered wave $\Phi_{\text{scat},k2}{}^{n=1}$ that is computed from Eq. (12). A similar expression can be written for $\Phi_{\text{scat},k2}{}^{n=2}$. Because the optical properties and the diameter of the two cylinders were identical in this study, we consider the case in which $D_1' = D_2'$ and $a_1 = a_2$.

With the approach described above, the fluence detected at position ρ_d can be computed inclusive of first-order-scattering effects [i.e., $\Phi(\rho_d) = \Phi_{\text{inc}}(\rho_d) + \sum_{k=1}^{2} \Phi_{\text{scat},k}{}^{n=1}(\rho_d)$], as well as second-order scattering effects [i.e., $\Phi(\rho_d) = \Phi\text{inc}(\rho_d) + \sum_{n=1}^{2}\sum_{k=1}^{2} \Phi_{\text{scat},k}{}^{n}(\rho_d)$]. From final values of complex fluence, the phase shift and amplitude demodulation can be predicted from the simple relationships:

$$\theta(\rho_d) = \tan^{-1}\frac{\text{Im}[\Phi(\rho_d)]}{\text{Re}[\Phi(\rho_d)]} \tag{14}$$

$$M(\rho_d) = (\{\text{Im}[\Phi(\rho_d)]\}^2 + \{\text{Re}[\Phi(\rho_d)]\}^2)^{1/2}. \tag{15}$$

3. Materials and Methods

A. Experimental Measurements of Phase Shift Owing to Two Cylindrical Absorbers

To experimentally measure $M_{k1,k2}(\rho_d)$, $M_{k1}(\rho_d)$, $M_{k2}(\rho_d)$, $M_{\text{inc}}(\rho_d)$, $\theta_{k1,k2}(\rho_d)$, $\theta_{k1}(\rho_d)$, $\theta_{k2}(\rho_d)$, and $\theta_{\text{inc}}(\rho_d)$, frequency domain measurements were made with an apparatus that uses picosecond pulsed light at 780 nm with an average power of 1.3 W. Details of the apparatus are described elsewhere.[19] The phantom consisted of a plexiglass cylinder (with a 16.5-cm diameter and 20-cm height) filled with a 0.5% Intralipid solution (Kabi Pharmacia, Inc., Clayton, N.C.). As illustrated in Fig. 3, light was delivered to a peripheral point on the cylinder with a 1000-μm fiber (Model HCP-M1000T-08, Spectron Specialty Optics Co., Avon, Conn.) and collected through a second fiber located 4 circumferential cm from the incident source. Bakelite plastic rods (diameter, 3.175 mm) were painted black to provide perfectly light-absorbing inhomogeneities. Measurements of $\theta(\rho_d)$ and $M(\rho_d)$ at 80 MHz were conducted as the rods were moved in tandem along the plane perpendicular to a line connecting the source

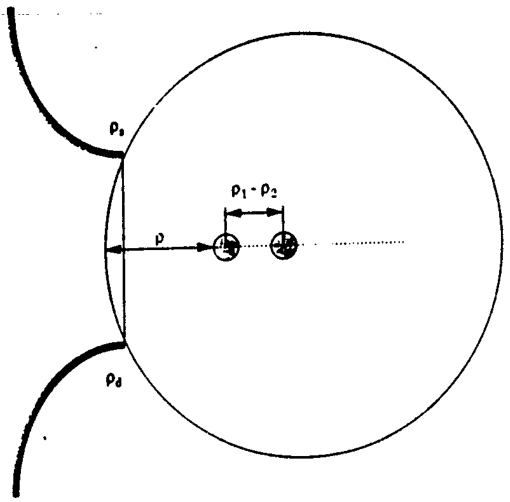

Fig. 3. Schematic illustrating the geometry of the experimental measurements.

and detector. Positioning was achieved with a motion controller (Model PMC200-P, Newport Corp., Irvine, Calif.) and a motorized actuator (Newport Model 850B). The actuator position was accurate to within 0.0050 mm. Phase and ac modulation were recorded as the distance between the center of the first absorbing cylinder, and the wall of the phantom was varied from 0 to 5 cm in 20 increments. When the two objects were moved in tandem, their separation distances ($\rho_1-\rho_2$) between the centers of the two perfect absorbers were 6, 10, and 20 mm. Three measurements were taken at each position. Measurements of phase shift and ac amplitude demodulation are reported relative to the absence case or θ_{inc} or M_{inc}.

B. Analytical Prediction of Phase Shift and Amplitude Modulation Owing to Two Absorbing Cylinders

In addition to the measurements of second-order interactions with the experimental approach described above, predictions of interactions between absorbers were computed analytically with Eqs. (11)–(15) with a modified version of an algorithm written by Boas that is available through the internet.[20] Complex fluence incorporating first- and second-order-scattering contributions was used to calculate phase shift owing to two infinite cylinders that effectively act as perfect absorbers ($\mu_a = 2\ \text{cm}^{-1}$, $\mu_s' = 10\ \text{cm}^{-1}$) in a turbid, semi-infinite medium mimicking our phantom ($\mu_a = 0.02\ \text{cm}^{-1}$, $\mu_s' = 10\ \text{cm}^{-1}$). Zero fluence boundary conditions were assumed and used in the algorithm.

C. Numerical Prediction of Phase Shift and Amplitude Demodulation Owing to Two Absorbing Heterogeneities

In addition to experimental measurements and analytical calculations, two-dimensional finite-element computations were conducted to predict the phase shift and amplitude demodulation resulting from first- and second-order interactions. The computations were performed on an Ultra 2 Sun Sparc workstation with a MATLAB partial differential equation toolbox. We solved the frequency domain diffusion equation for light propagation to determine the fluence from an 80-MHz sinusoidally modulated light source. The simulated phantom was an infinite cylinder 16.5 cm in diameter. The optical properties of the medium were set to mimic the experimental conditions of $0.02\ \text{cm}^{-1}$ for the absorption coefficient μ_a and $10\ \text{cm}^{-1}$ for the isotropic scattering coefficient μ_s'. We modeled the nearly perfect absorbers in these computations as infinite cylindrical rods and we approximated by increasing the absorption coefficient to 100 times that of the surrounding medium ($\mu_a = 2.0\ \text{cm}^{-1}$). The scattering coefficient for the object was set to that of the surroundings ($\mu_s' = 10\ \text{cm}^{-1}$) to mimic the analytical computations. The phantom was discretized into 66,048 triangular elements that contained 33,281 nodes. A partial current boundary condition was used to approximate light reflection and transmission across the boundary of the phantom as would be expected in the experimental measurements. Although our meshing did not permit representation of the perfect absorber as a volume excluded for light transport, we approximated the heterogeneity with a high absorption coefficient because others have shown that the propagation characteristics are comparable.[18] It is noteworthy that, although these computations do not exactly mimic the experimental measurements described below, they nonetheless adequately describe the contributions of second-order scattering effects. The forward solution was obtained for each absorbing cylinder alone and then in combination. The results were analyzed in a manner similar to the analysis of the experimental results with Eq. (7) and (8).

4. Results and Discussion

A. Experimental Results

Figures 4(a)–4(c) and 5(a)–5(c) illustrate the phase shift and the amplitude demodulation changes as a function of position of the pair of perfect absorbers whose centers are separated by 6, 10, and 20 mm. The symbols denote individual measurements of phase shift difference in the presence of the two hidden objects, and the symbols connected by the lines denote the phase shift and the amplitude demodulation calculated from Eq. (7) and (8) with measurements made in the absence and in the presence of a single individual absorber. The measured values of phase shift and amplitude demodulation denoted by the open symbols are therefore reflective of higher-order contributions, whereas the solid line reflects only first-order contributions. Paired Student's t-test shows that there is a significant difference ($p < 0.005$) between the set of phase shift and amplitude demodulation measurements and that predicted by Eqs. (7) and (8) for two perfect light-absorbing objects separated by 6, 10, and 20 mm and positioned at various distances from the source and the detector [Figs. 4(a)–5(c)]. Our results also show that the magnitude of second-order effects is greatest for two

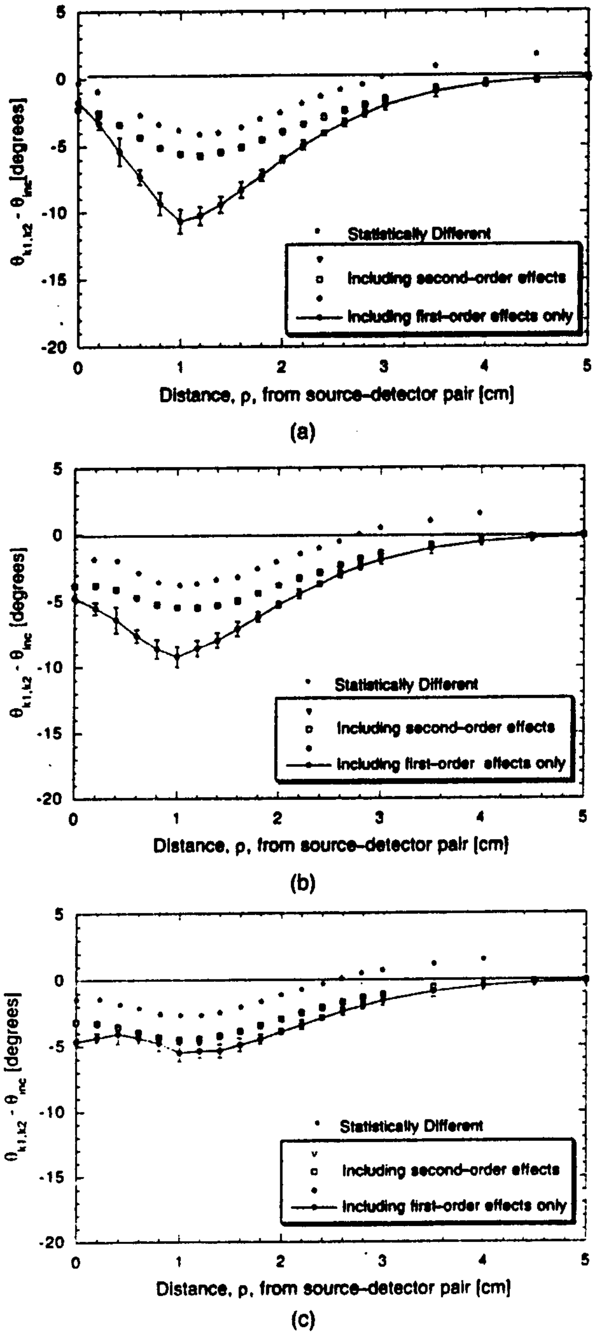

Fig. 4. Experimental values of $\theta_{k1,k2}-\theta_{inc}$ the phase difference (in degrees) relative to the absence condition as a function of distance from the source–detector pair. The symbols denote individual measurements in the presence of two cylinders separated by distances of (a) 6, (b) 10, and (c) 20 mm, whereas the line connects predictions from Eq. (7) and measurements of θ_{k1}, θ_{k2}, and θ_{inc}. The error bars denote the propagation of measurement errors (standard deviation) associated with θ_{k1}, θ_{k2}, and θ_{inc}. The x axis is reported as the distance between the wall and the first cylinder ($k1$). The asterisks denote significant difference ($p < 0.005$, paired Student's t-test) between the values experimentally measured and those obtained from Eq. (7).

absorbing heterogeneities spaced 6 mm apart and becomes smaller at 10 and 20 mm. The paired t-test indicates that there are significant differences at the 99.5% confidence levels (indicated by the asterisks in

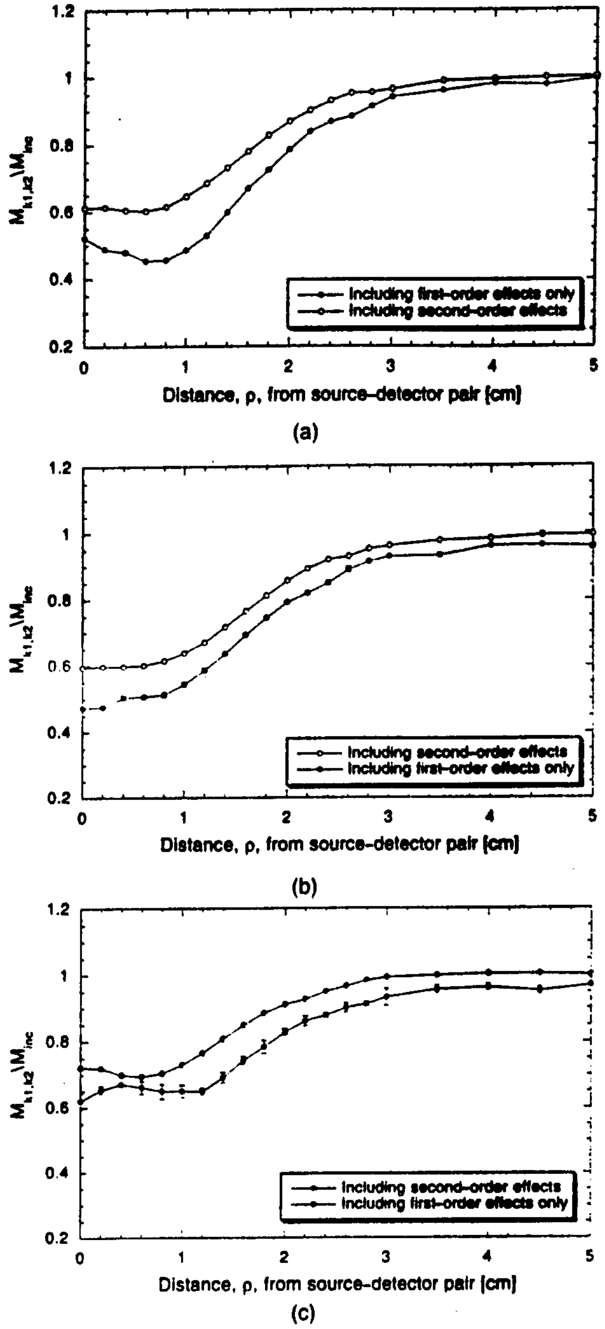

Fig. 5. Experimental values of $M_{k1,k2}/M_{inc}$ (in arbitrary units) relative to the absence condition as a function of distance from the source–detector pair. The symbols denote individual measurements in the presence of two cylinders separated by distances of (a) 6 (b) 10, and (c) 20 mm, whereas the line connects predictions from Eq. (8) and measurements of M_{k1}, M_{k2}, and M_{inc}. The error bars denote the propagation of measurement errors (standard deviation) associated with M_{k1}, M_{k2}, and M_{inc}. The x axis is reported as the distance between the wall and the first cylinder ($k1$).

Fig. 4) between individual experimental phase-shift values that reflect first- and higher-order scattering contributions to the detected signal and those computed values that are indicative of first-order effects only. From the data for 6-mm absorber separation illustrated in Fig. 4(a), it can be seen that the actual experimental measurements of phase shift change

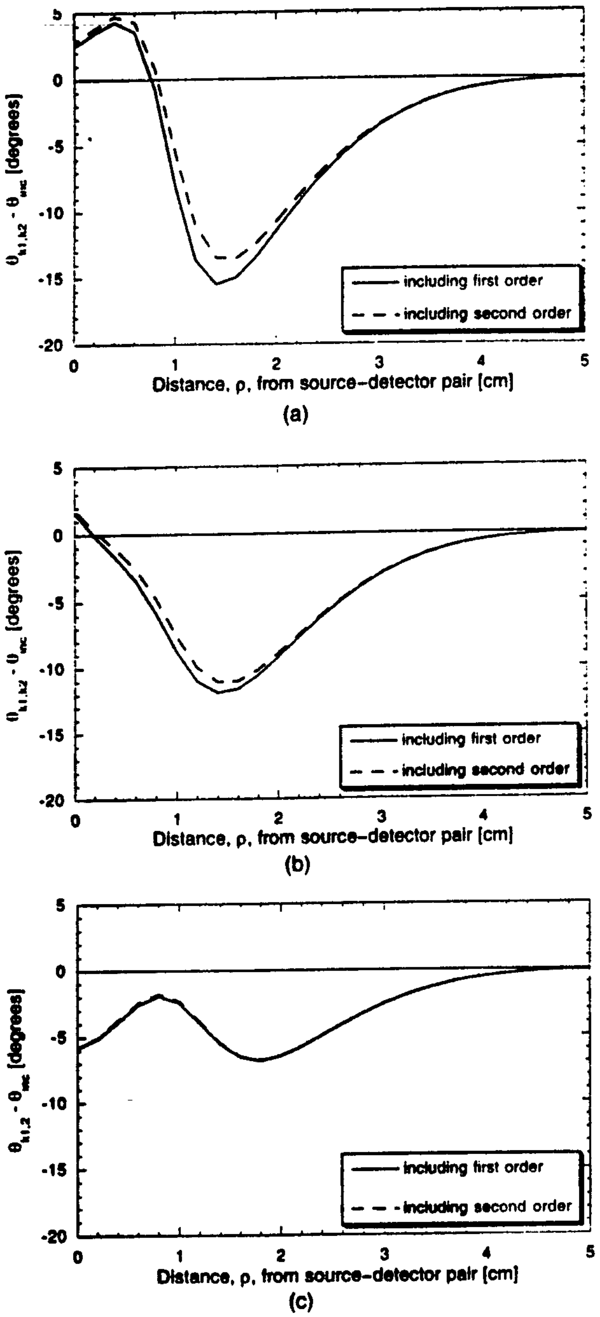

Fig. 6. Values of $\theta_{k1,k2}-\theta_{inc}$ (in degrees) calculated from the analytical prediction of first-order (solid line) and inclusive of second-order (dashed line)-scattering effects as a function of distance (cm) from the source–detector pair for two absorbing cylinders separated by (a) 6, (b) 10, and (c) 20 mm. The x axis is reported as the distance between the wall and the first cylinder ($k1$) and the phase shift reported relative to the absence case.

caused by two objects are smaller than those predicted by Eq. (7), in which second- and higher-order perturbations are not accounted for. At greater distances from the source and detector, agreement between experimental and predicted phase shift change suggests that second-order effects may indeed be negligible, even for the smallest separation, but only in a region where the objects' contributions to the detected signal is comparatively small. This is reasonable because second-order effects are expected to increase with proximity to the source and the detector. From our studies, it appears that separations greater than 20 mm are necessary for their accurate resolution through perturbative reconstruction approaches when perfect absorbers are involved.

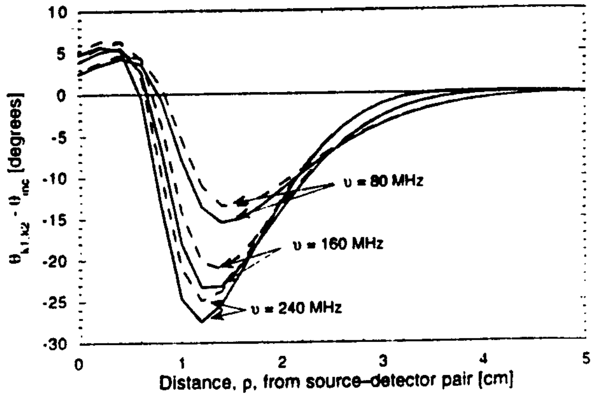

Fig. 7. Values of $\theta_{k1,k2}-\theta_{inc}$ (in degrees) calculated from analytical prediction of first order (solid curve) and inclusive of second order (dashed curve) for two absorbing cylinders separated by 6 mm and interrogated at 80, 160, and 240 MHz.

B. Analytical Computations

Our experimental results are also validated by the analytical predictions that account for first- and second-order scattering contributions. Figures 6(a)–6(c) depict the qualitative trends seen in the experimental data presented for phase difference in Figs. 4(a)–4(c). There appears to be good agreement between the trends observed experimentally with various separation distances and analytical predictions. Specifically, higher-order contributions significantly perturb the detected phase shift values when the separations between the center of two absorbing cylinders are 6 mm [Fig. 6(a)] and 10 mm [Fig. 6(b)]. The contribution of higher-order scattering from cylindrical absorbers is not significant when the separation distance is 20 mm [Fig. 6(c)]. However comparison with experimental results shows that there are differences in the absolute magnitude and shape of the phase shift change versus object distance. These distances are most likely caused by the differences in the boundary conditions, geometry, and absorber strength between the analytical and the experimental results. Nonetheless, the trends confirm experimental results that the presence of second-order perturbations reduces the phase shift change owing to two light-absorbing bodies. Neglecting second-order effects could cause an underestimation of absorption strength or size when reconstruction algorithms based on first-order perturbations are used.

In addition, we investigated the variation of second-order perturbations with modulation frequency as shown in Fig. 7. The simulated data of phase shift change versus position of the heterogeneities is depicted for two cylindrical absorbers (d =

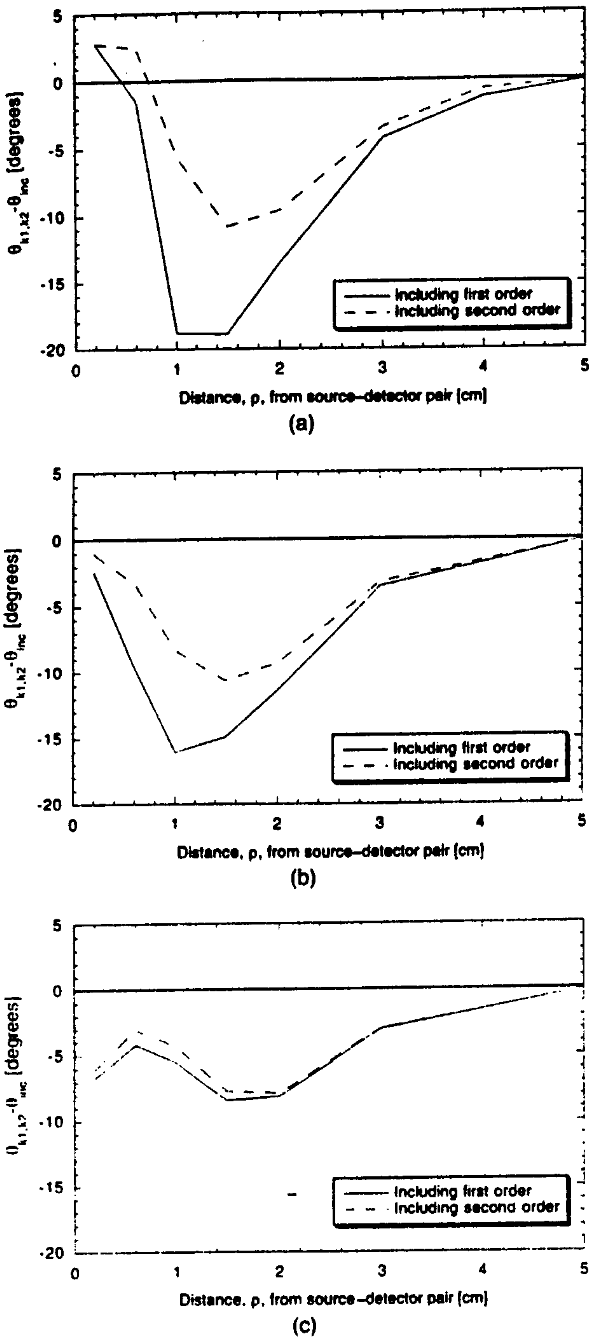

Fig. 8. Finite element computations of $\theta_{k1,k2}-\theta_{\rm inc}$ (in degrees) relative to an absence condition for considering only first-order (solid line) and including second-order (dashed line) perturbations as a function of distance (cm) from the source–detector pair for absorbing cylinders separated by (a) 6, (b) 10, and (c) 20 mm. The x axis is reported as the distance between the wall and the first cylinder ($k1$) and the phase shift reported relative to the absence case.

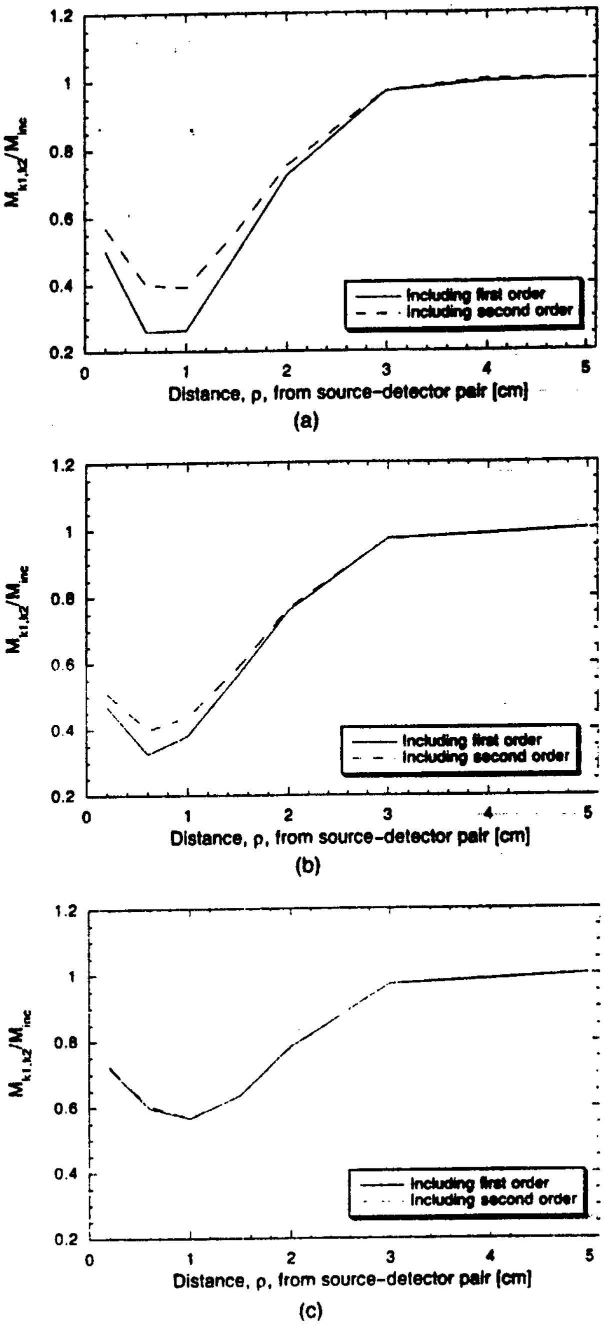

Fig. 9. Finite element computations of $M_{k1,k2}/M_{\rm inc}$ (in arbitrary units) referenced to an absence condition for both the first-order (solid line) and the second-order (dashed line) perturbations as a function of distance (cm) from the source–detector pair for absorbing cylinders separated by (a) 6, (b) 10, and (c) 20 mm. The x axis is reported as the distance between the wall and the first cylinder ($k1$) and the modulation ratio is reported relative to the absence case.

3.125 mm, $\mu_a = 2\ \mathrm{cm}^{-1}$) separated by 6 mm in a semi-infinite medium. Again, the phase shift is reported relative to the absence case, and the distance is reported from the wall to the center of the first cylinder. Three frequencies were evaluated: 80, 160, and 240 MHz. The absolute value of phase shift increases with frequency, but the contribution of second-order effect remains roughly the same absolute value. Consequently the error in assuming negligible second-order scattering effects becomes smaller at increasing frequencies. This is expected because increased damping of a rescattered photon density wave occurs at higher modulation frequencies. While these results intimately depend upon the choice of optical properties, they nonetheless point out that the error in neglecting second-order scattering contributions in analytically based reconstructions becomes smaller with increasing modulation frequencies. Of course the error reduction occurs at the expense of interrogating a smaller volume of tissue with a source modulated at an increased frequency.[21]

C. Finite Element Computations

Our experimental results were validated not only by analytical predictions but also with finite element computations. Figures 8(a)–9(c) show the numerical computations that correspond to the experimental phase shift data presented in Figs. 4(a)–5(c). Again there appears to be good agreement between the trends of the experimental and the analytical results and the numerical solutions. Also, higher-order contributions perturb the detected phase shift values when the separation distances between the two rods are 6 mm [Fig. 8(a)] and 10 mm [Fig. 8(b)]. The contribution of higher-order scattering from the cylindrical absorbers is not significant when the separation distance is 20 mm [Fig. 8(c)]. Figures 9(a)–9(c) show the amplitude demodulation relative to an absence condition. The modulation data also show results similar to those obtained experimentally. These computation results confirm that the presence of second-order perturbations is important for two light-absorbing objects that are less than 20 mm apart.

5. Conclusions

In summary, our experimental measurements show that the contributions of higher-order scattering of propagating photon density waves may not always be insignificant. While our analytical and numerical computations do not exactly reproduce experimental conditions (i.e., two-dimensional finite element, semi-infinite geometry, etc.), they nonetheless demonstrate that the experimental trends can be attributed to second-order effects. Under conditions of high contrast caused by absorption, analytical approaches to the inverse imaging algorithm may restrict the resolution and the sensitivity of biomedical optical imaging performed in the frequency domain. An analogy can also be drawn for time domain and cw reconstruction approaches that do not deploy full solutions to the diffusion equation to account for the interdependence of voxel optical properties on measured fluences. Certainly our results are based on the worst-case scenario of perfect absorbers and may have less impact on the image reconstructions involving imperfect absorbers. Under conditions in which multiple heterogeneities are contrasted with their surroundings on the basis of scattering or fluorescence, the first-order perturbation assumption may not be as restrictive. Indeed, if the nonlinearity associated with second-order scattering effects is small, noniterative Born and Rytov approximations are especially attractive because image reconstruction is not computation intensive. Nonetheless, our results suggest that inverse imaging algorithms that depend solely on first-order perturbations caused by local changes in tissue absorption properties may not provide a reconstruction as accurate as those algorithms that depend on the full numerical calculation of the diffusion equation with specified boundary conditions.

6. Appendix A

1. Nomenclature

a_k	Radius of cylinder k (cm)
c_n	Speed of light through the medium (cm/s)
D	Optical diffusion coefficient of homogeneous medium (cm)
$D_{k'}$	Diffusion coefficient inside the cylinder (cm)
I_n	Modified Bessel function
$I_{n'}$	Derivative of modified Bessel function I_n
K_n	Modified Bessel function
$K_{n'}$	Derivative of modified Bessel function K_n
M	ac demodulation of the incident light (mW/cm^2)
m	Number of objects
p	Integration variable in Helmholtz equation describing scatter from an infinite cylinder (cm^{-1})
S_{source}	Strength of modulated source at position ρ_s, represented as a complex number of amplitude and phase (mW)
x	Variable in Helmholtz equation describing scatter from an infinite cylinder (cm^{-1})
y	Variable in Helmholtz equation describing scatter from an infinite cylinder (cm^{-1})
z	Axial direction of the cylindrical heterogeneities or length (cm)

2. Greek

Φ	Photon fluence (mW/cm^2)
Φ_{inc}	Photon fluence of incident wave or in the absence of heterogeneities (mW/cm^2)
Φ_{scat}	Photon fluence arising from scattered wave (mW/cm^2)
ρ	Position vector (cm)
ρ_s	Position of the source (cm)
ρ_d	Position of detector (cm)
ρ_k	Center position of object k (cm)
θ	Phase shift of light wave (deg or rad)
ϑ	Angle between ρ_s and ρ_d
μ_a	Absorption coefficient of homogeneous surroundings (cm^{-1})
$\mu_{s'}$	Isotropic scattering of homogeneous surroundings (cm^{-1})
$\mu_{a'}$	Absorption coefficient of cylinder (cm^{-1})
$\mu_{s''}$	Isotropic scattering of cylinder (cm^{-1})

3. Subscripts and Superscripts

$_n$	Order of perturbation or nth-order scattering effect
$_k$	Index denoting cylindrical object one, $k1$; two, $k2$; or both objects, $k1$, $k2$
$_{\text{inc}}$	Index denoting absence measurement or condition

This research was supported in part by the National Institutes of Health (R01 CA61413, R01

CA67176, K04 CA68374) and the U.S. Army Medical Research Breast Cancer Program (DAMD17-96-1-6023).

References

1. L. M. Wang, P. P. Ho, and R. R. Alfano, "Double-stage picosecond Kerr gate for ballistic time-gated optical imaging in turbid media," Appl. Opt. **32**, 535–540 (1994).
2. B. B. Das, K. M. Yoo, and R. R. Alfano, "Ultrafast time-gated imaging in thick tissues: a step toward optical mammography," Opt. Lett. **18**, 1092–1094 (1993).
3. S. G. Demos, H. Savage, A. S. Heerdt, S. Schantz, and R. R. Alfano, "Time resolved degree of polarization for human breast tissue," Opt. Commun. **124**, 439–442 (1996).
4. J. R. Singer, F. A. Grunbaum, P. Kohn, and J. P. Zubelli, "Image reconstruction of the interior of bodies that diffuse radiation," Science **248**, 990–993 (1990).
5. J. C. Hebden, R. A. Kruger, and K. S. Wong, "Time-resolved imaging through a highly scattering medium," Appl. Opt. **30**, 788–794 (1991).
6. M. A. O'Leary, D. A. Boss, B. Chance, and A. G. Yodh, "Experimental images of heterogeneous turbid media by frequency domain diffusing photon tomography," Opt. Lett. **20**, 426–428 (1995).
7. H. Jiang, K. D. Paulsen, U. L. Osterberg, B. W. Pogue, and M. S. Patterson, "Simultaneous reconstruction of absorption and scattering maps in turbid media from near-infrared frequency domain data," Opt. Lett. **20**, 2128–2130 (1995).
8. H. Jiang, K. D. Paulsen, and U. L. Osterberg, "Optical image reconstruction using frequency domain data: simulations and experiments," J. Opt. Soc. Am. A **13**, 253–266 (1996).
9. M. A. Franceschini, K. T. Moesta, S. Fantini, G. Gaida, E. Gratton, H. Jess, W. W. Mantulin, M. Seeber, P. M. Schlag, and M. Kaschke, "Frequency-domain techniques enhance optical mammography: initial clinical results," Proc. Natl. Acad. Sci. USA **94**, 6468–6473 (1997).
10. E. M. Sevick, J. R. Lakowicz, H. Szmacinski, K. Nowaczyk, and M. L. Johnson, "Frequency domain imaging of absorbers obscured by scattering," J. Photochem. Photobiol. B **16**, 169–185 (1992).
11. E. Gratton, W. Mantulin, M. J. van de Ven, J. Fishkin, M. Maris, and B. Chance, "A novel approach to laser tomography," Bioimaging **1**, 40–46 (1993).
12. R. L. Barbour, H. L. Graber, Y. Wang, J. H. Chang, and R. Aronson, "A perturbation approach for optical diffusion tomography using continuous-wave and time resolved data," in *Fiber Optic Sensors: Engineering and Applications*, A. J. Bruinsma and B. Culshaw, eds., Proc. SPIE **1511**, 87–120 (1993).
13. S. R. Arridge, P. van der Zee, M. Cope, and D. T. Delpy, "Reconstruction methods for infra-red absorption imaging," in *Time-Resolved Spectroscopy and Imaging of Tissues*, B. Chance and A. Katzir, eds., Proc. SPIE **1431**, 204–215 (1991).
14. S. R. Arridge, M. Schweiger, M. Hiraoka, and D. T. Delpy, "Performance of an iterative reconstruction algorithm for near-infrared absorption and scatter imaging," in *Photon Migration and Imaging in Random Media and Tissues*, R. R. Alfano and B. Chance, eds., Proc. SPIE **1888**, 360–371 (1993).
15. D. A. Boas, B. O'Leary, B. Chance, and A. G. Yodh, "Scattering of diffuse photon density waves by spherical inhomogeneities within turbid media: analytical solution and applications," Proc. Natl. Acad. Sci. USA **91**, 4887–4891 (1994).
16. Y. Yao, Y. Wang, Y. Pei, W. Zhu, and R. L. Barbour, "Frequency-domain optical imaging of absorption and scattering distributions by a Born iterative method," J. Opt. Soc. Am. A **14**, 325–342 (1997).
17. S. R. Arridge, M. Cope, and D. T. Delpy, "The theoretical basis for the determination of optical path lengths in tissue: temporal and frequency-domain analysis," Phys. Med. Biol. **37**, 1531–1560 (1992).
18. H. C. van de Hulst, *Light Scattering by Small Particles* (Dover, New York, 1981).
19. C. L. Hutchinson, T. L. Troy, and E. M. Sevick-Muraca, "Fluorescence-lifetime determination in tissues or other scattering media from measurement of excitation and emission kinetics," Appl. Opt. **35**, 2325–2332 (1996).
20. D. A. Boas, http://dpdw.eotc.tufts.edu/boas/PMI/pmi.html.
21. E. M. Sevick, J. K. Frisoli, C. L. Burch, and J. R. Lakowicz, "Localization of absorbers in scattering media by use of frequency-domain measurements of time-dependent photon migration," Appl. Opt. **33**, 3562–3570 (1994).